2011

Fabrication of Organosilane Nanostructures as Selective Sites for Surface Chemical Reactions

Kathie Lee Lusker
Louisiana State University and Agricultural and Mechanical College

FABRICATION OF ORGANOSILANE NANOSTRUCTURES AS SELECTIVE SITES FOR SURFACE CHEMICAL REACTIONS

A Dissertation

Submitted to the Graduate Faculty of
Louisiana State University and
Agricultural and Mechanical College
in partial fulfillment of the
requirements for the degree of
Doctor of Philosophy

in

The Department of Chemistry

by
Kathie Lee Lusker
B.S., Louisiana State University, 2004

December 2011

ACKNOWLEDGEMENTS

I would like to express my gratitude to my advisor, Dr. Jayne Garno, for her guidance and support during my research studies at LSU. I have been fortunate to have an advisor that has given me numerous opportunities to travel and attend major conferences. I also want to thank my committee members Dr. Kermit Murray, Dr. Graca Vicente, Dr. Megan Macnaughtan, Dr. Jin-Woo Choi, and Dr. Francisco Hung for reviewing my dissertation and providing valuable feedback.

I also thank both past and present members of the Garno research group, especially Dr. Jie-Ren Li, for all of the discussions and good times we had in the past. They have all made my time at LSU more enjoyable and have given me memories that I will cherish forever. Lastly, and most importantly, I want to express my deepest appreciation to my parents (Lee and Sha Lusker), three sisters (Jennifer, Zabrina, and Aine), grandparents (Fe Apostol and Tom and Amy Pester), and boyfriend of 12 years (Gregory Ardoin) for all of their moral support, advice, love and encouragement. Without them, I would not be where I am today.

TABLE OF CONTENTS

LIST OF TABLES

LIST OF FIGURES

LIST OF ABBREVIATIONS

Abbreviation	Name
6-AAPTMS	N-(6-Aminohexyl)-3-aminopropyltrimethoxysilane
AFM	Atomic Force Microscopy
BSA	Bovine Serum Albumin
CS-AFM	Current Sensing Atomic Force Microscopy
ECT	Eicosanethiol
ESL	Edge Spreading Lithography
FM-AFM	Force Modulation Atomic Force Microscopy
FFT	Fast Fourier Transform
FWHM	Full Width at Half Maximum
HCP	Hexagonally Close-packed
HDDT	12-Hydroxydodecanethiol
HOPG	Highly Ordered Pyrolytic Graphite
IMM	Indirect Magnetic Modulation
ITO	Indium Tin Oxide
MAC	Magnetic AC
MPTMS	3-Mercaptopropyltrimethoxysilane
OPV	Organic Photovoltaic
OTS	Octadecyltrichlorosilane
PDMS	Polydimethylsiloxane
PEG-silane	2-[Methoxy-(polyethyleneoxy)propyl]trichlorosilane
PS	Polystyrene

RIE	Reactive Ion Etching
SAM	Self-assembled Monolayer
SDV	Standard Deviation
SERS	Surface Enhanced Raman Spectroscopy
SHA	Sulfanylhexadecanoic acid
SPL	Scanning Probe Lithography
SPM	Scanning Probe Microscopy
STM	Scanning Tunneling Microscopy
UTS	10-Undecenyltrichlorosilane

ABSTRACT

Naturally self-assembled mesospheres provide a practical route for controlling the arrangement of materials on surfaces at the nanoscale. Periodic arrays of well-defined nanostructures can be produced with different nanomaterials and interpattern spacings. Results presented in this dissertation demonstrate particle lithography methods developed for fabricating arrays of organosilane nanostructures. Surfaces were designed for the selective deposition of polymers and nanoparticles to produce multicomponent nanopatterns. The approaches for surface patterning provide new directions for studying surface chemistry at the molecular-level, and have practical application for emerging photovoltaic thin film technologies.

Atomic force microscopy (AFM) provides unique capabilities for molecular visualization and ultrasensitive measurements of surface properties with nanoscale resolution. Organosilane nanopatterns bearing different functionalities and chain lengths were characterized using AFM to gain insight on molecular organization and surface-assembly processes. Indirect magnetic modulation (IMM) is a new instrument configuration for force modulation AFM that was developed for investigating mechanical properties of materials. The principle of IMM is based on indirect oscillation of soft nonmagnetic cantilevers through the tip holder assembly, which contains magnetic materials. Imaging can be performed in either ambient or liquid environments. The driving frequency for tip vibration can be selected to enhance contrast in amplitude and phase images, which provides information on the elastic response of thin-film materials. Images acquired with IMM furnish nanoscale resolution views of the morphology and elastic response of organosilane nanostructures. The dampening effect of liquid imaging media on cantilever oscillation during IMM was investigated using a liquid sample cell.

Organic photovoltaic (OPV) devices are promising alternatives to traditional silicon based solar cells. A major challenge for OPVs is the requirement for higher efficiencies, or better device performance. The nanoscale morphology and molecular organization of the donor/acceptor materials in the organic layer affects the conductivity of OPV devices. To improve efficiency, new fabrication methods must be developed that are capable of controlling the molecular structure of the donor/acceptor materials. Using particle lithography combined with contact printing, billions of periodic and uniform pillar nanostructures of polythiophene can be fabricated on the surface. The dimensions and spacing can be selectively tuned by using different size latex masks.

CHAPTER 1. INTRODUCTION

Nanostructures have many uses for applications in sensors,[1-2] catalysis,[3] molecular separation,[4] and electronic devices.[5] The ability to control surface chemistry at the nanoscale poses a challenge for the development of emerging technologies such as protein chips or molecular junctions. The investigations in this dissertation describe nanofabrication methods based on particle lithography developed for generating well-defined nanostructures of organosilanes, which can be used as a structural platform for building more complex architectures. Molecular-level investigations of the morphology, self-assembly processes, and properties of designed nanostructures were accomplished using atomic force microscopy (AFM).

1.1 Nanoscale Characterizations Using Atomic Force Microscopy

The capability of AFM for achieving nanoscale resolution enables characterization of material properties, as well as fundamental investigations of chemical or biochemical reactions. Fundamental studies of surface reactions and material properties at the molecular-level can provide essential information for the development of new and advanced technologies in fields such as materials engineering,[6-7] molecular electronics,[8-9] and medical diagnostics.[10-11] Chapter 2 of this dissertation summarizes the background and history of AFM. The basic operating principle of the AFM imaging modes used for this research are described, including contact mode, lateral force imaging, tapping-mode, and phase imaging. Force-distance spectroscopy and force modulation modes of AFM are also reviewed.

1.2 Controlling the Arrangement of Materials on Surfaces at the Nanoscale with Particle Lithography

Development of nanotechnology depends not only on capabilities for synthesis of functional nanomaterials and molecules, but also requires the ability to spatially arrange and organize materials on surfaces at the nanoscale. Developing new high throughput fabrication

techniques with control of the chemical functionality, geometry and spatial organization of nanostructures on surfaces can aid in the development of functional materials for electronic, sensing, and optical device applications. Particle lithography, also referred to as nanosphere lithography, is a versatile, high throughput approach for fabrication that has been used to generate 2D and 3D periodic arrays of materials on surfaces.[12-15] Close packed layers of monodisperse mesospheres (latex or colloidal silica) provide a lithographic mask or structural template, which can then be used to guide the deposition of materials onto the surface. The spherical geometry of the mesoparticles restricts deposition processes. Areas of the surface where the mesospheres make contact with the substrate remain protected during steps of material or thin film deposition. The surface nanopatterns produced by particle lithography correspond to the arrangement and periodicity of the mesospheres used for the mask. Chapter 3, entitled "Defining the Chemistry of Surfaces at the Nanoscale using Particle Lithography", provides a comprehensive literature review of contemporary approaches with particle lithography applied for patterning self-assembled monolayers (SAMs), proteins, and nanoparticles.

1.3 Particle Lithography as a Toolkit for Spatially Confining Surface Reactions of Organosilanes

Combining particle lithography with molecular self-assembly is a practical approach for producing organosilane nanostructures with controlled geometries and designated surface coverage. In this nanofabrication approach, the locations of water residues are confined around the bases of latex mesospheres and define the sites for vapor deposition of trifunctional organosilanes. Particle lithography combined with vapor deposition generates billions of periodically arranged nanopatterns with control of the geometry, density, and surface chemistry. Chapter 4 ("Particle Lithography Combined with Vapor Deposition: A Toolkit for Studying Confined Surface Reactions in Nanoscale Liquid Volumes") demonstrates examples of

organosilane nanopatterns presenting different terminal groups and chain lengths prepared with particle lithography.[16] The self-polymerization reactions of ω-functionalized silanes were investigated using high-resolution AFM studies combined with nanolithography. Tapping-mode AFM was used to study the effect of the terminal moieties of organosilanes by evaluating parameters of the number density, surface coverage and thickness of layers formed.

1.4 Defining the Site-selectivity of Surfaces Using Organosilane Nanopatterns for the Adsorption of Functionalized Nanoparticles

Periodic arrays of organosilane nanostructures prepared with particle lithography provide a foundation to spatially define sites for adsorption of nanoparticles. Surfaces can be designed with methyl-terminated organosilane nanopatterns to furnish a resist for further chemical steps. Uniform patterns of nanosized holes of uncovered silicon substrate were prepared within a nanostructured film of octadecylsiloxane using particle lithography combined with vapor deposition. Exposed areas of the substrate furnish sites for selectively binding silanol-functionalized gold nanoparticles, whereas areas with methyl-terminated silane provide an effective resist to prevent nonspecific adsorption. By immersing patterned substrates into a solution of surface-active gold nanoparticles coated with 3-mercaptopropyltrimethoxysilane (MPTMS), architectures of functionalized nanoparticles with uniform geometry and periodic spacing were generated on surfaces of glass and silicon wafers. Surface changes throughout the steps of particle lithography were investigated using contact mode and tapping-mode AFM. To investigate the optical properties of nanopatterned nanoparticles, samples were characterized with UV-Vis spectrophotometry. Measurements reveal that a red-shift occurred as a result of changes in interparticle distance as the nanoparticles assemble onto spatially confined areas of the surface patterns. Studies of nanostructures of silane-functionalized nanoparticles prepared within resists of organosilane nanopatterns produced with particle lithography will be described

in Chapter 5. This chapter is entitled "Nanostructures of Functionalized Gold Nanoparticles Prepared by Particle Lithography with Organosilanes", and has been submitted for publication in *Langmuir*.

1.5 A Hybrid Approach Using Particle Lithography for the Fabrication of Periodic Nanostructures on Surfaces

A hybrid patterning approach was developed which combines particle lithography with contact printing of organosilanes. Arrays of nanopores within an octadecyltrichlorosilane (OTS) film are generated by direct transfer of organosilane ink to the substrate using physical deposition. In this hybrid approach for nanopatterning, a block of polydimethylsiloxane (PDMS) is used to transfer inks of organosilanes to the substrate through a mesoparticle mask of either latex or colloidal silica spheres. Removal of the mask of mesospheres reveals regularly-spaced pores or holes within an organosilane film. The interpattern spacing between nanopores is determined by the diameters of the mesospheres selected for the mask. The nanopores are areas of uncovered substrate (i.e. Si/SiO_2, glass, indium tin oxide) and provide selectivity for bottom-up nanofabrication, forming billions of periodic sites for attaching other nanomaterials or molecules. Chemical modification of the pores can be accomplished by immersing the nanopatterned samples in a solution containing new molecules. Nanopatterns prepared with particle lithography combined with contact printing were characterized with contact mode and tapping-mode AFM and will be described in Chapter 6 ("Hybrid Approach for Nanofabrication: Particle Lithography Combined with Contact Printing of Organosilanes"; manuscript in preparation).

1.6 Preparation of Nanostructured Conducting Polymer Thin Films

Organic photovoltaic (OPV) devices are promising alternatives to solar cell technologies. Compared to traditional silicon solar cells, OPV devices are more cost-effective to fabricate,

have a lower production time, can be applied to flexible and plastic substrates, and the fabrication process is more environmentally friendly.[17] Despite these advantages, a major challenge exists for improving the power conversion efficiency of OPVs, which is the ratio of electrical energy output to energy input. An efficiency of at least ten percent is needed for OPV devices to be considered for commercial production. The nanoscale morphology and molecular organization within the organic layers and at the donor-acceptor interface can affect the overall efficiency and performance of OPV devices.[18-19] To reach higher efficiencies, new methods must be developed that are capable of precisely controlling the nanoscale organization and molecular structure of the polymers during device fabrication. Chapter 7 demonstrates a "bottom-up" nanopatterning approach for designing a bulk heterojunction OPV device. Particle lithography provides a practical route for building complex molecular structures using successive steps of surface chemical reactions. Particle lithography combined with contact printing was applied for creating nanostructured arrays of organosilane, which furnishes a scaffold for controlling the hierarchical and lateral organization of conducting polymers (e.g. polythiophene) during surface-initiated *in situ* living polymerization. Well-defined arrays of polythiophene pillars with tailorable sizes, geometries and spacing are produced on surfaces of Si(111), ITO, and quartz.

1.7 Measuring the Elasticity of Organosilane Nanostructures with Indirect Magnetic Modulation AFM in Air and Liquid Media

Ring-shaped nanopatterns of organosilanes fabricated via particle lithography combined with vapor deposition furnish ideal test platforms for investigating local mechanical properties (i.e. elasticity and stiffness) at the nanoscale using force modulation with indirect magnetic modulation (IMM) AFM.[20] For IMM imaging, an AC electromagnetic field is generated by a solenoid located beneath the sample plate. The flux of the external AC field causes indirect oscillation of a soft, non-magnetic cantilever (spring constants <1 N/m) within the tip holder

assembly, which contains ferromagnetic components. Different driving frequencies can be chosen to drive the cantilever to oscillate. Phase and amplitude images are acquired simultaneously with topography frames using IMM and provide a detailed map of the elastic response of samples. Resonance driving frequencies were selected from frequency-response spectra to drive tip oscillation. Chapter 8 presents results for studies of the elastic response of organosilane nanostructures using IMM in air and liquid environments. An advantage of IMM compared to other FM-AFM instrument configurations is that indirect actuation of the tip results in very low forces (<1 nN) applied to the sample. Therefore, it is a non-destructive approach to imaging that is suitable for analyzing the mechanical properties of delicate samples, such as polymers and biological species.

1.8 Dissertation Synopsis

Particle lithography is a versatile toolkit for generating surface nanostructures with designed functionalities and tunable geometries. Mesoparticle masks and templates can be prepared over large areas and provide a practical route for patterning nanoparticles, organic thin films, and polymers on surfaces with nanoscale precision. Chapter 9 presents future work for fabricating a complete OPV device with enhanced efficiency. The spaces between polythiophene nanopillars can be filled with a suitable acceptor (n-type) material, and a top aluminum electrode can be deposited by metal evaporation. Control of the molecular organization of both donor and acceptor materials can facilitate carrier transport towards the top and bottom electrodes. Future investigations will involve studying the effect of nanoscale morphology on photoelectric properties of the polythiophene nanopillars using current sensing AFM (CS-AFM). Local measurements of the conductive properties with CS-AFM of polythiophene nanostructures can provide insight on the correlation between molecular structure/organization and sample conductivity with nanoscale resolution.

CHAPTER 2. INSTRUMENTAL METHODS USING ATOMIC FORCE MICROSCOPY

2.1 Background and Imaging Principle of Atomic Force Microscopy

Atomic force microscopy (AFM) was invented by Binnig, Quate, and Gerber in 1986 and has become a powerful surface analysis tool capable of achieving unprecedented resolution at the atomic and molecular level.[21] Over the last two and a half decades, AFM has provided a fundamental understanding of the role of structure and material properties. An advantage of AFM is that experiments can be accomplished in nearly any environment, such as in liquid, vacuum, or in ambient air, with capabilities for dynamic studies to monitor changes in surface morphology that evolve over time using time-lapse AFM. Both conducting and insulating materials can be characterized with AFM without the need for sample pretreatment. The ultrasensitive measurement capabilities of AFM have been demonstrated to achieve lateral resolution less than 1 nm and vertical resolution of 0.1 nm.[22] Studies with AFM have been applied for characterizing metal nanoparticles,[23-25] proteins[26-28] and polymers.[29-30]

For AFM, also referred to as scanning force microscopy, a sharp probe (tip) affixed to the end of a cantilever is scanned across the surface to collect information about sample morphology. Depending on the instrument configuration and AFM imaging mode, information about tip-surface adhesion, magnetic forces, frictional forces, elastic compliance and sample conductance can be obtained.

The movement of the tip over the sample surface is controlled by a piezoceramic scanner. By applying voltages to the piezoscanner, movements of the cantilever over the sample surface can be precisely controlled at the nanoscale in the x, y, and z directions. The most commonly used AFM tips are ultrasharp silicon (Si) or silicon nitride (Si_3N_4) probes, which are attached to either a V-shaped or rectangular (diving board) cantilever. The cantilevers typically have lengths ranging from 10-200 μm and widths of 20-40 μm. The geometries of the apex of the tips are

usually square-based pyramids or cylindrical cones. The backside of the cantilever is coated with a reflective coating. A photodiode laser is used to focus a laser beam on the back of the cantilever while the tip raster-scans the sample surface in a line-by-line fashion. Changes in the vertical bending (deflection) or oscillation amplitude of the tip are monitored and detected using a position sensitive photodetector. Changes in deflection or oscillation amplitude are maintained to an assigned setpoint value through the use of an electronic feedback loop. Images of the sample are digitally constructed by recording the changes in tip-surface interaction as a function of tip position. A three dimensional profile of the surface can be acquired with AFM. Information about the material properties can be acquired and mapped simultaneously with surface topography.

Imaging modes of AFM are categorized according to how the AFM tip is operated in proximity with the sample surface: contact, non-contact and intermittent-contact. In contact mode AFM, the AFM tip remains in direct contact with the sample continuously during imaging, whereas in non-contact mode, the tip is maintained at a discrete distance from the sample. For intermittent-contact modes, the tip is driven to oscillate at or near its resonance frequency and 'taps' the sample during scanning; intermittent-contact mode is frequently referred to as tapping-mode AFM. The most common AFM imaging modes are contact and tapping-mode AFM. The following sections will provide an overview of specific AFM imaging modes used for the research presented in this dissertation. The fundamental principles and basic operation for contact mode, frictional force, tapping-mode and phase imaging will be described.

2.2 Contact Mode and Lateral Force Imaging

For contact mode imaging, the AFM tip remains in direct physical contact with the surface during imaging. Contact mode and lateral force imaging are accomplished simultaneously. For contact mode AFM, a sharp probe at the end of a cantilever is raster-scanned

across a surface using a piezoelectric tube scanner. Applying a voltage to the piezoelectric material causes it to expand or contract for precise positioning of the tip during scanning. A photodiode laser is used to focus light on the backside of the reflective cantilever and deflected to a quadrant photodetector (Figure 2.1). While the tip is scanned in contact with the sample, the bending of the cantilever will produce a change in the position, or deflection, of the laser spot focused on the photodetector. For contact mode AFM, the deflection is related to the force applied to the sample, and is maintained at a constant value (i.e. a setpoint value). To maintain the initial deflection setpoint value for the force applied between the tip and sample, the feedback loop of the computer controller incrementally adjusts the voltage applied to the piezoscanner. Variations in the surface topography will induce cantilever bending and, therefore, result in vertical displacement of the laser position in the top and bottom quadrants of the photodetector.

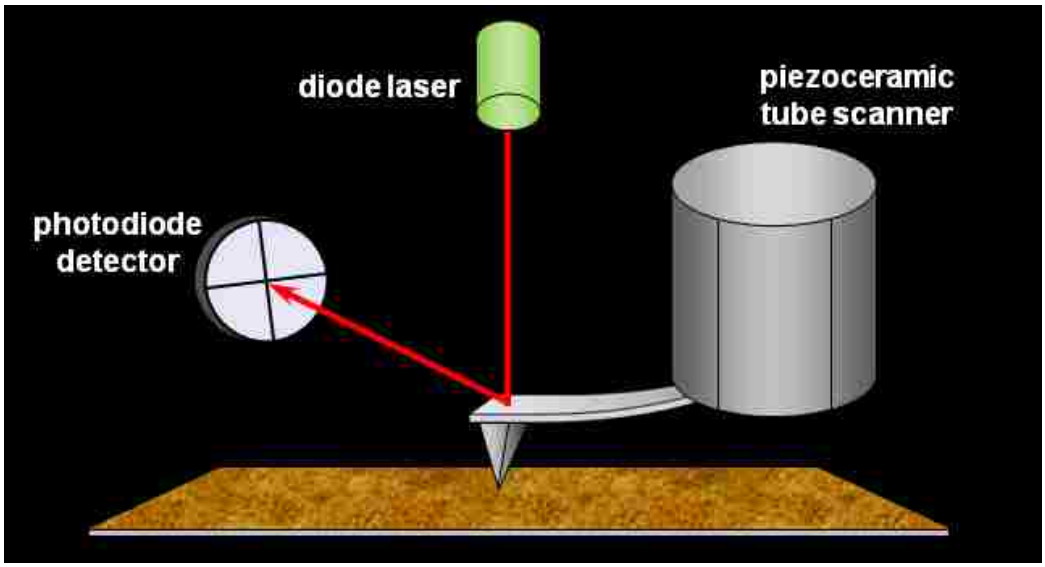

Figure 2.1 Operating principle of contact mode AFM.

Torsional twisting of the cantilever causes lateral displacement of the position of the laser spot. The lateral force mode of imaging is sensitive to differences in chemical composition and mechanical (friction) properties of the sample.[31-32] As the tip is dragged across the surface, torsional twisting is caused by frictional forces between the tip and the sample. Torsional

twisting of the tip induces changes in the position of laser spot in the left and right quadrants of the detector, which are then used to construct digital lateral force images.[33] Lateral force images map the changes in frictional force between the tip and the sample as it is scanned in contact with the surface. Frictional force images are acquired by subtracting the trace and retrace lateral force images. Lateral force images often show edge features of the surface because tip-surface adhesive interactions are quite different at the sides of nanostructures. For contact mode AFM, topography and lateral force images are acquired simultaneously.

A drawback of contact mode AFM is that the shear forces caused by the scanning tip can damage delicate and soft samples. To overcome this problem, soft cantilevers with small spring constants can be used for contact mode imaging to reduce the amount of force exerted on the sample. Alternatively, one can perform contact mode in liquid media. Typical force settings used for operating in air can range from 1 to 10 nN, whereas force settings less than 1 nN can be applied for imaging in liquid environments.

Height measurements (z-dimension) reaching sub-Angstrom resolution can be routinely achieved with contact mode AFM. However, measurements of the lateral dimensions obtained with AFM often are not representative of the true sample topography. The lateral features are often broadened and exaggerated as a result of the size and shape of the AFM tip. The effect is known as tip-sample convolution, which occurs when the radius of curvature of the tip is greater than the size of the feature being imaged on the surface. Blunt tips do not accurately trace the shapes of sample features. As the tip is scanned over the sample, the sides of the tip make contact before the apex of the tip. Therefore, the final lateral dimensions viewed in the AFM image is actually an image of the shape and dimensions of the tip, as depicted in Figure 2.2. The use of a sharp probe with a high aspect ratio can alleviate the issue with tip-sample convolution since a sharp probe can follow the surface contours more accurately (right of Figure 2.2). Alternatively,

the use of tip and sample deconvolution programs can digitally reconstruct the surface profiles to provide a better approximation of the true surface features.[34-37]

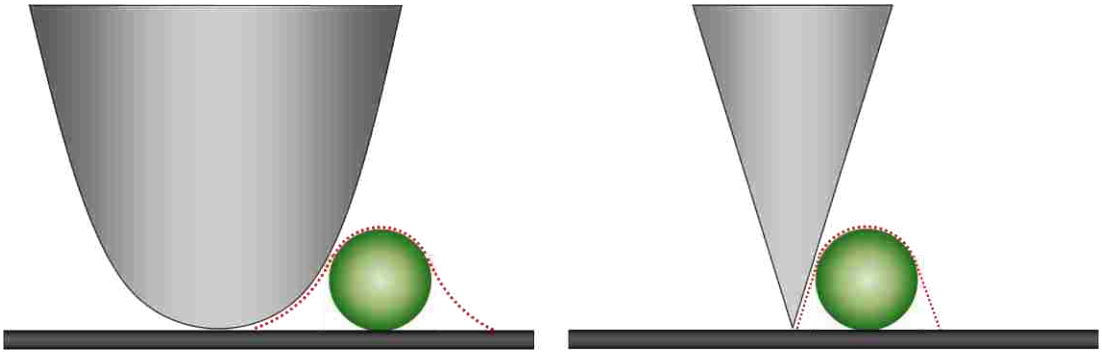

Figure 2.2 Effect of tip size and shape on mapping lateral dimensions of surface features.

Atomic force microscopes must be calibrated in the X-Y axis to obtain accurate information. The bending and hysteresis of piezotube scanners are not completely linear for X-Y-Z displacement motions. A method for correcting the non-linearity of X-Y displacement is to add calibration sensors to the X-Y piezoelectric scanner to measure the actual piezo displacement; this is known as "closed-loop" feedback operation. The Z axis of the piezoelectric scanner must also be linear and calibrated to obtain accurate height measurements. Commercially available calibration standards are used for micron-level calibration of AFM's. Microfabricated calibration grids or gratings consist of arrays of uniform structures (e.g., silicon, highly ordered pyrolytic graphite or HOPG, aluminum) with accurate step heights, pitch (i.e. distances between structures), and lateral dimensions. Open-loop AFM scanners used for this research were calibrated at the nanoscale using the step height of flat Au(111) films (2.25 Å) and the periodic lattices of mica(0001), HOPG, and Au(111), which have lattice constants of 5.18, 2.46, and 2.88 Å, respectively.

2.2.1 AFM Force Spectroscopy

Forces between the tip and sample form the basis for all measurements with AFM. Forces can be measured down to the pN level with AFM force spectroscopy, where the deflection of the

cantilever is measured during a sample approach and retract cycle. A force-distance curve is a plot of the cantilever deflection as a function of the tip position in the z-direction. Forces between the probe and sample are calculated by applying Hooke's Law, **F = -kz**. For this relation, **F** is the force, **k** is the cantilever spring constant, and **z** is the distance between the tip and sample.

An example of a force-distance curve acquired in air for nanostructures prepared with octadecyltrichlorosilane (OTS) on Si(111) substrates is displayed in Figure 2.3. A force-distance curve is acquired during a single approach and retract cycle. Initially, the tip is far away from the sample. There are no interactions present between the tip and sample, thus no cantilever deflection (region I). As the tip approaches the sample, the tip senses attractive forces with the sample. This causes the tip to "snap into contact" with the surface, thus indicating a negative (attractive) force (region II). This region of the force-distance curve can be used for measuring surface forces such as van der Waals and electrostatic combined forces of attraction. As the tip continues approaching the sample, long and short-range repulsive forces cause the cantilever to bend, as shown in region III. Once the deflection reaches a maximum, the tip begins to retract away from the surface (region IV). Adhesive forces maintain contact between between the tip and sample during retraction. When the distance between the tip and sample is large enough to overcome long-range attractive interactions, the cantilever "snaps out of contact" (region V) and returns to a zero deflection (region VI). This region can be used for approximating surface energy or binding forces of materials.

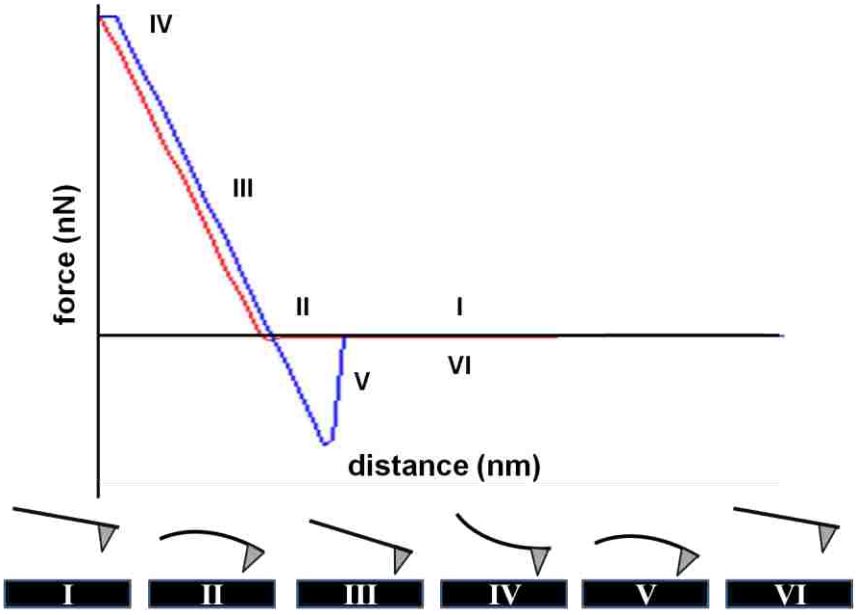

Figure 2.3 Force-distance curve acquired in air with a Si_3N_4 tip for OTS surface nanopatterns fabricated on Si(111) substrates.

2.3 Tapping-Mode and Phase Imaging

Tapping-mode AFM is an intermittent imaging mode and was developed to address the challenges faced with contact mode AFM for characterizing loosely bound or easily damaged materials, such as proteins,[38-39] polymers[40-41] and nanoparticles.[42-44] With tapping-mode imaging, damage to the tip or sample is minimized since lateral and shear forces exerted on the sample are greatly reduced. The general principle of tapping-mode AFM is based on driving the motion of a cantilever to oscillate near its natural resonance frequency (Figure 2.4). Typical resonance frequencies for tapping-mode tips range from 150 to 300 kHz. Tapping-mode tips are much stiffer compared to contact mode tips, with spring constants around 20-50 N/m. Transient interfacial bonds between the tip and sample are not formed in tapping-mode because of the rapid tip motion. The amplitude of the cantilever oscillation is typically 50 to 100 nm, which is sufficient to provide the cantilever with enough energy to overcome adhesion forces.[45-46] The tip is mounted directly on a piezoactuator. To induce tip oscillation, an AC voltage is applied to the

piezoactuator within the AFM nosecone. When the tip is scanned across the surface, the oscillating cantilever intermittently touches, or 'taps', the sample. The amplitude of the oscillating cantilever is monitored by the photodetector. In tapping-mode, a feedback loop is used to maintain a constant amplitude. The measured amplitude (i.e. output signal) is compared to the amplitude setpoint value (i.e. driving AC input signal). The difference between the output and driving signals is known as the error signal. The feedback loop uses the error signal to determine the voltage needed to maintain a constant amplitude.[47] The incremental changes in voltage required to maintain a constant amplitude signal are then translated into digital images of the surface topography with nanoscale resolution.

Phase images are acquired simultaneously with surface topography with tapping-mode operation. Information of surface composition, adhesion, stiffness, and viscoelasticity can be obtained with phase imaging.[48-50] A lock-in amplifier is used to measure the phase lag of tip oscillation relative to the driving AC input signal as a basis for generating phase images. The phase lag is very sensitive to differences in material properties.

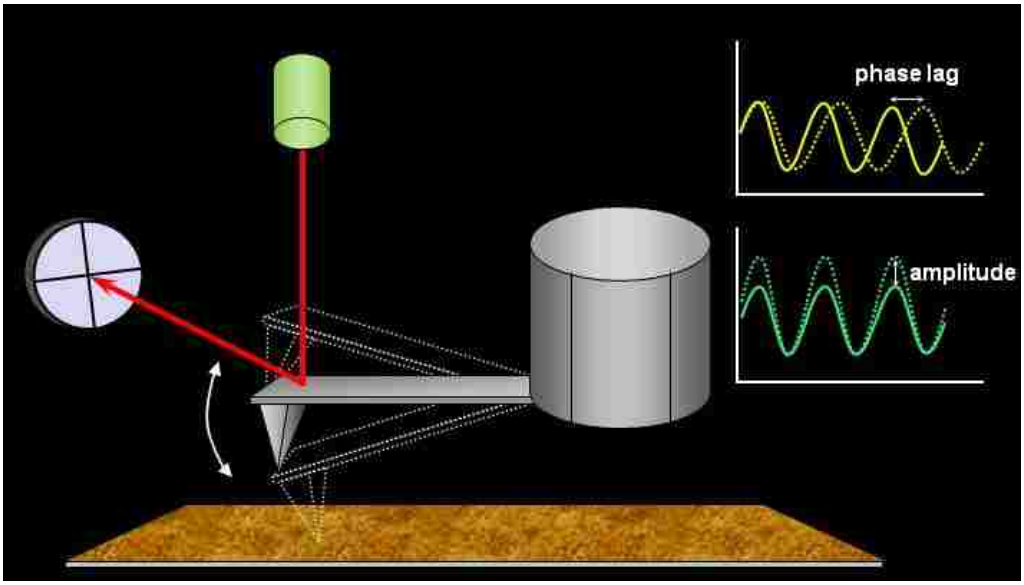

Figure 2.4 Basic operating principle for tapping-mode AFM.

2.4 Force Modulation AFM

Force modulation is an AFM imaging mode used for probing local mechanical properties (e.g., elastic and viscoelastic properties) of surfaces.[51-53] With force modulation AFM, the relative elasticity and stiffness of materials can be characterized and mapped with phase and amplitude images.[54-58] During force modulation, an AFM tip is scanned in direct contact (i.e. in contact mode) with the surface and at the same time, a periodic oscillation is applied and introduced into the z-direction. The periodic oscillation leads to a modulation of the force between the tip and the sample. The magnitude of the tip deflection is detected by the photodiode detector and is influenced by the relative elasticity of the sample (i.e., the cantilever deflection is inversely proportional to the magnitude of deformation of the sample). Under the same applied force, a soft area deforms more than a hard area during scanning, resulting in a reduction in the oscillating amplitude of the tip.[51-52] During imaging, the amplitude and phase response of the cantilever are detected by a lock-in-amplifier and recorded as a function of the tip position for surface mapping. Differences between the amplitude and phase versus the periodic function of the driving AC signal are used to generate digital images of changes in surface elastic properties.

Force modulation experiments can be accomplished using one of several instrument setups, which differ in the way the tip is driven to oscillate. One strategy for inducing tip vibration is to apply a periodic AC signal directly to the segment of the piezotube scanner which drives the tip to oscillate in the z-direction. Another instrument configuration applies a periodic AC signal to a small piezoceramic chip to directly drive the tip to vibrate. In addition, probes which contain a thin magnetic coating on the topside can be driven to vibrate with an externally applied AC electromagnetic field. This approach is known as magnetic force modulation (MFM). Thin magnetic films can be deposited on AFM tips either by heated metal evaporation or by gluing microscopically small magnets onto the cantilever.[59] When an external AC

electromagnetic field is applied, the magnetically coated probe is driven to oscillate. A disadvantage of MFM is that metal coatings tend to wear off over time when scanning in contact mode. Also, the magnetic strength of the coating decreases with time and therefore requires re-magnetization of the cantilever. A further instrument configuration for force modulation AFM was developed for this dissertation research (Chapter 8), which uses indirect magnetic modulation (IMM) of non-magnetic probes.

2.5 AFM Imaging Modes Used for Dissertation Research

For this dissertation research, imaging and measurement modes of AFM were chosen according to the nature of the sample and environmental requirements. Details of the samples, sample preparation procedures, and specific operating parameters are presented within each chapter. A summary and overview of the imaging modes used for this dissertation is presented in Table 2.1.

Table 2.1 AFM imaging modes used for dissertation research experiments.

	Sample description	**Contact mode**	**Lateral force mode**	**Tapping-mode**	**Phase imaging**	**IMM**
Chapter 4	Organosilane nanopatterns on Si(111) prepared by PL			X	X	
Chapter 5	Organosilane and functionalized Au nanoparticles patterned on Si(111) prepared by PL			X	X	
Chapter 6	Organosilane nanopatterns on Si(111) prepared by PL	X	X	X	X	
Chapter 7	OTS and polythiophene nanostructures prepared on Si(111) and quartz by PL and surface initiated living polymerization	X	X			
Chapter 8	Organosilane nanopatterns on Si(111) prepared by PL			X		X

**PL = particle lithography

CHAPTER 3. DEFINING THE CHEMISTRY OF SURFACES AT THE NANOSCALE USING PARTICLE LITHOGRAPHY

3.1 Introduction

As technology continues to progress, there is a growing demand for more practical and effective lithographic methods capable of producing structures at the nanoscale with designed functionalities and desirable properties. Considerable research efforts have been invested over the years to develop new or improved techniques for fabricating organized arrays of materials both at the nanoscale and with high throughput. Particle lithography is a high throughput surface patterning approach that allows nanoscale control of the organization of materials and provides a generic approach for nanopatterning organic thin films, proteins, and other nanomaterials. Materials that have been patterned include polymers,[60-61] metals,[62-67] organic thin films,[16, 68-73] nanoparticles,[14, 74-75] and proteins.[15, 76-77] Particle lithography has been used for patterning on surfaces of glass, silicon wafers, mica, ITO, and Au(111). The outcome is a nanofabrication approach for defining the arrangement and surface coverage of designed materials using self-assembly chemistry. This chapter provides an overview of the less conventional approaches for patterning nanomaterials that combine chemical approaches with particle lithography to create nanostructured surfaces with well-defined selectivity, morphology and reactivity.

3.2 History and Development of Particle Lithography

Particle lithography is a materials general method for nanopatterning originally developed by Deckman and Dunsmuir in 1982.[78] In their original work, arrays of silicon posts were fabricated by reactive ion milling of 400 nm latex spheres, followed by removing the spheres with an oxygen ion beam. Patterns of triangular silver posts on silicon substrates were also prepared by evaporating silver over an array of 400 nm latex spheres. Particle lithography has also been referred to as colloidal lithography,[79] nanosphere lithography,[80-81] evaporative

lithography,[14] or natural lithography.[78] The natural assembly of spherical particles, such as latex or colloidal silica, is used to prepare a surface mask or template. Solutions of size-sorted monodisperse spheres naturally self-assemble into periodic lattices on flat surfaces. Nanostructures are prepared by depositing materials through the surface masks of mesospheres.

3.3 Strategies for Nanolithography with Particle Masks

Several approaches have been reported for preparing arrays of colloidal spheres, such as spin-coating,[80, 82-83] solvent evaporation,[14, 75] and colloidal self-assembly occuring at an air-liquid interface[84] or in an electric field.[85-86] The spheres spontaneously self-assemble on the surface to form periodic structures with regular geometries and interparticle spacings. In almost all cases, self-assembled 2D colloidal mesospheres are hexagonally close-packed (hcp), since hcp is more thermodynamically stable.[87] In addition to hcp, 2D non-close-packed colloidal crystals are also possible and can be obtained by etching of ordered 2D colloidal spheres using techniques such as isotropic plasma etching,[88] anisotropic reactive ion etching (RIE),[89] and electron beam irradiation.[90] However, this chapter will focus primarily on nanopatterns prepared using 2D close-packed colloidal spheres.

An example mask of close-packed mesospheres with hexagonal symmetry is shown with an atomic force microscopy (AFM) image in Figure 3.1. The surface topography of 300 nm polystyrene latex discloses the arrangement of mesospheres prepared by drying an aqueous drop of monodisperse latex on Si(111) in ambient conditions. The crystalline layer of mesospheres furnishes a mask for guiding the deposition of evaporated metals, organic vapors or other nanomaterials. Areas where the spherical particles are in contact with the substrate remain protected during deposition processes. The mask of mesospheres can be removed by rinsing steps, sonication, dissolution, calcination, isotropic plasma etching,[88] anisotropic reactive ion etching,[89] and electron beam irradiation.[90] Adhesive tape can also be used to physically strip

away the mask.[14] The surface nanopatterns generated with particle lithography correspond to the arrangement, diameter and periodicity of the mesospheres used for the mask. Therefore, the interpattern spacings and size can be selected by choosing different diameters of mesospheres.

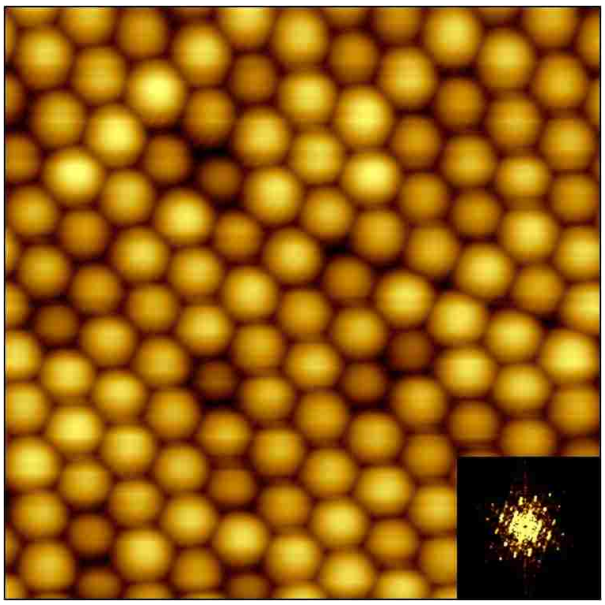

Figure 3.1 Close-packed layer of PS mesospheres (diameter 200 nm) on a Si(111) substrate. View of a 2 x 2 μm^2 AFM topograph; inset shown is an FFT analysis of the topography image.

Various shapes, sizes, geometries, and interpattern spacings can be obtained with particle lithography depending on the nanofabrication technique, mesosphere deposition method and size of mesospheres used for sample preparation. Chemistry approaches for nanofabrication with particle lithography include evaporation,[67, 78] direct deposition,[91] and etching.[66] Examples for different nanomaterials patterned are summarized in Table 3.1, which have a common strategy of using mesoparticles for lithography. Particle lithography was used to generate arrays of rings, dots or pillar nanostructures that are comprised of inorganic materials, organic thin films, quantum dots, and biomolecules.

Table 3.1 Chemical approaches for particle lithography with inorganics, SAMs, nanoparticles, and proteins.

	Substrate	**Material and Pattern Geometry**	**Mask/ Template**	**Sphere Diameter**	**Patterning Method/Approach**	**Mask/ Template Removal**	**Ref.**
Inorganics	silicon	TiO_2 nanorods	polystyrene	350 nm-1 μm	pulsed laser deposition	not removed	[92]
	sapphire (Al_2O_3)	TiO_2 nanobowls	latex	505 nm	atomic layer deposition, ion beam milling	toluene etching	[93]
	Si(100)	silicon nanopillars	latex	280-440 nm	deposition of Cr nanoparticles via sputtering followed by reactive ion etching	sonication in CH_2Cl_2	[94]
	Si(111)	Ni, Co nanoparticle arrays	latex	100 nm-1 μm	electron beam evaporation	dissolution and sonication in THF	[74]
	Pt-coated silicon	lead zirconium titanate nanorings	latex	3 μm and 160 nm	room temperature pulsed laser deposition of lead zirconium titanate films, followed by high angle argon ion etching and annealing	thermal annealing in air	[95]
Alkanethiols	gold	concentric rings of ECT, SHA, and HDDT	colloidal silica	1.6 μm	printing with a planar PDMS stamp	sonication in water	[91]
	gold	rings and porous membrane of HDT	colloidal silica	800 nm	vapor phase deposition	sonication in water	[96]
Organosilanes	Si(111), mica(0001), glass, Au(111)	rings or pores of OTS, PEG-silane, 6-AAPTMS	latex	100-500 nm	chemical vapor deposition	rinsing and sonicating in ethanol	[16, 71-73]
	Si(100)	porous OTS film	colloidal silica	200-500 nm	solution immersion	sonication in aqueous medium	[69]
Quantum Dots (QD's)	mica(0001)	rings or pores of cysteine coated CdS QD's	latex or colloidal silica	200- 800 nm	drop deposition of a PS/QD solution with varying ratios, followed by drying	rinsing with ethanol or water	[75]
	glass	rings of CdSe QD's	latex	200 nm-2 μm	evaporation induced assembly	adhesive tape	[14]

	Substrate	Material and Pattern Geometry	Mask/ Template	Sphere Diameter	Patterning Method/Approach	Mask/ Template Removal	Ref.
Proteins	glass and silicon	dots of fibrinogen, P-selectin, and BSA	latex	2-10 μm	liquid phase grafting of PEG-silane to masked substrate, followed by removal of mask and incubation in protein solution	rinsing with water	[97]
	HOPG and glass	honeycomb rings of BSA, fibrinogen, and antimouse IgG	latex	0.56-5.43 μm	incubation in protein solution	ultrasound in HBSS-Ca^{2+} buffer solution	[98]
	gold	dot arrays of streptavidin and biotinylated antibody	latex	400 nm	preparation of well-controlled mixed SAMs of thiol-derivatives on gold dot arrays, followed by immersion in protein solution	sonication in THF	[99]
	mica(0001) and Au(111)	arrays of BSA and rabbit IgG	latex	200- 800 nm	solvent evaporation of mixed solutions of latex and protein	rinsing with water	[15]
	mica(0001) and Au(111)	ring and pore arrays of BSA and staphylococcal protein A	latex	200-500nm	solvent evaporation of mixed solutions of latex and protein	rinsing with water	[76]

*THF, tetrahydrofuran; SAMs, self-assembled monolayers; PDMS, polydimethylsiloxane; ECT, eicosanethiol; SHA, sulfanylhexadecanoic acid; HDDT, 12 hydroxydodecanethiol; HDT, hexadecanethiol; OTS, octadecyltrichlorosilane; PEG-silane, 2-[methoxy-(polyethyleneoxy)propyl]trichlorosilane; 6-AAPTMS, N-(6-aminohexyl)-3-aminopropyltrimethoxysilane; HOPG, highly ordered pyrolytic graphite; BSA, bovine serum albumin; IgG, immunoglobin

3.4 Applications of Particle Lithography for Patterning Self-Assembled Monolayers

Nanoscale patterning has been accomplished with self-assembled monolayers (SAMs) of organothiols and organosilanes using particle lithography. Combining particle lithography with molecular self-assembly is a practical strategy to generate nanostructures with controlled surface chemistry and defined geometries. Nanopatterns of SAMs can be used as a surface template for

integrating other molecules or materials and have potential applications for sensor surfaces and electronic devices.[100] Due to their stability and well-ordered surface structures, SAMs are an ideal platform for studying molecular, protein and cellular binding events and have been used extensively for biological research.

Several methods based on particle lithography have been reported for patterning organothiols.[70, 96] Patterns of thiol SAMs form spontaneously by S-Au chemisorption on surfaces of coinage metals. Organothiol nanopatterns with sub-100 nm dimensions were fabricated by a particle lithography approach developed by McLellan et al. known as edge-spreading lithography (ESL).[70, 91, 101] With ESL, alkanethiol molecules were transferred from a planar polydimethysiloxane (PDMS) stamp onto a gold substrate through a particle mask. A 2D array of monodispered silica beads are used as a guide during the deposition of alkanethiols. The molecules form a SAM around the circular footprint of each silica bead. With longer contact times between the PDMS stamp and masked substrate, the area of the SAM expands laterally by reactive spreading.[70, 101] Arrays of concentric rings of thiolate monolayers with carboxy- (bright), hydroxyl- (gray), and methyl-terminal groups patterned on gold substrates are shown in the lateral force microscopy (LFM) images in Figure 3.2. The concentric rings in Figure 3.2 were obtained by printing sulfanylhexadecanoic acid (SHA), 12-hydroxydodecanethiol (HDDT), and eicosanethiol (ECT). The widths of the monolayer rings are dependent on the printing time and concentration of the organothiol ink. Additionally, the position of each monolayer within the concentric ring pattern can be controlled by changing the printing order.

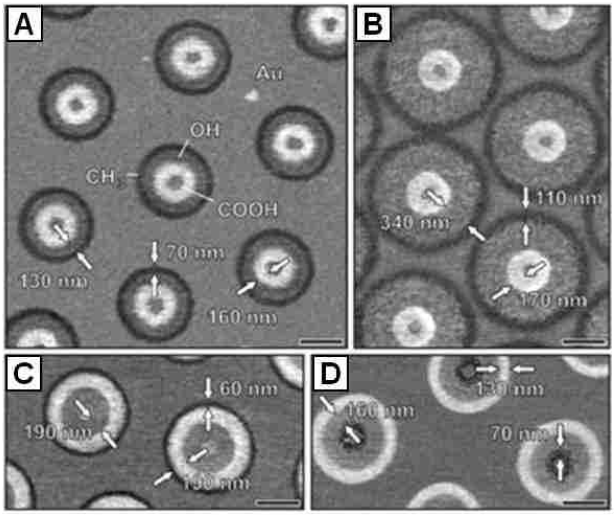

Figure 3.2 Concentric ring nanopatterns of alkanethiolate SAMs on gold prepared by ESL using 1.6 µm silica particles displayed with LFM images: (A) rings prepared by successive printing of SHA, HDDT, and ECT; (B) increase in ring width for HDDT and ECT monolayers is accomplished with longer printing times; (C) patterns prepared by successive printing of HDDT, SHA and ECT; (D) concentric rings produced by first printing ECT, followed by HDDT and SHA. All scale bars are 500 nm. Reproduced with permission from ref[91], M. Geissler et al., *Angew. Chem. Int. Ed.*, 44 (**2005**). Copyright@ John Wiley & Sons, Inc.

Approaches for particle lithography using organosilane SAMs have been developed and applied to various substrates (e.g., silicon oxide, aluminum oxide, germanium oxide, quartz, glass, gold, mica[102]). Organosilane SAMs are chemically robust due to the covalent nature of the siloxane network formed on surfaces. Post-chemical modification of silane SAMs can be accomplished for further binding steps or modifying the surface properties or reactivity without destroying the original thin film.

Vapor deposition steps can be combined with particle lithography to fabricate organosilane nanostructures.[16, 71-72] To form nanopatterns of organosilane SAMs, trace amounts of water are necessary to initiate surface hydrolysis of organotrichlorosilanes. The masks of latex mesospheres can be used to direct the placement of water residues on surfaces, and organosilanes bind selectively at sites of water.[71] Depending on the drying conditions used to prepare latex masks, either ring patterns or films with nanopores can be produced as shown in Figure 3.3.

When latex masks are dried briefly, water is distributed homogenously throughout areas of the surface (Figure 3.3A). When the partially dried latex mask is exposed to organosilane vapors, molecules do not deposit on the areas protected by latex spheres. After removal of the latex mask by a rinsing step, an organosilane thin film with uncovered periodic holes is formed on the surface, as shown in Figure 3.3B and 3.3C. When latex masks are dried for longer intervals, water residues persist only near the base areas of spheres to produce a circular water meniscus (Figure 3.3E). After vapor deposition, ring-shaped nanostructures are produced that conform to the sites of water residues, as shown in Figures 3.3F and 3.3G.

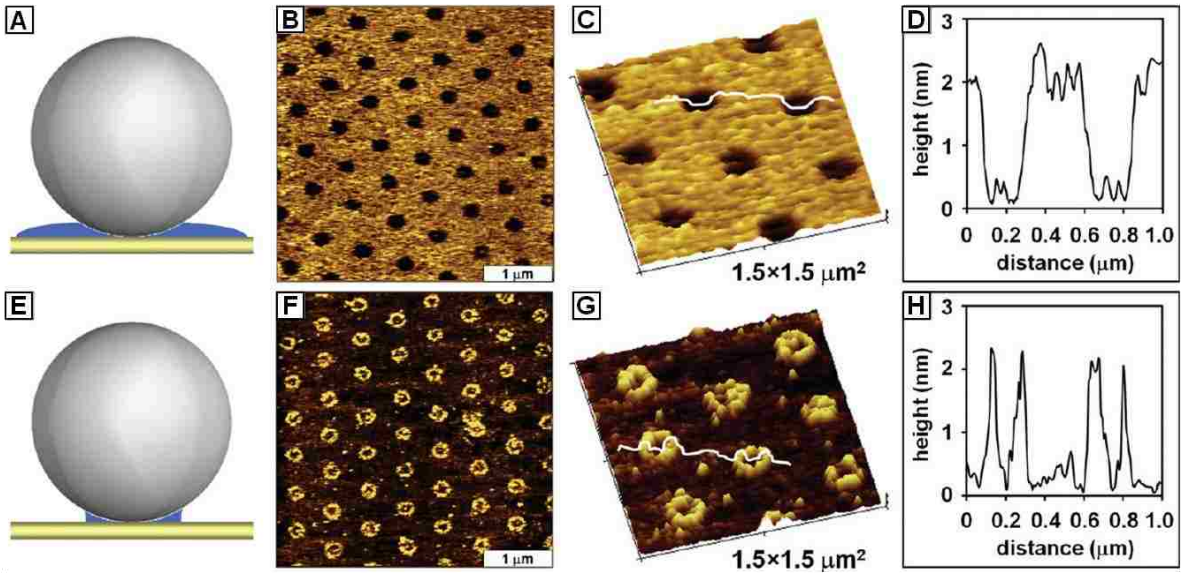

Figure 3.3 Nanopatterns of OTS on mica(0001) prepared by particle lithography combined with vapor deposition using 500 nm latex masks. (A) Thin film of water is produced on surface for briefly dried masks; (B) OTS film with periodic pores of uncovered substrate shown with an AFM topograph; (C) zoom-in of B; (D) height profile for the line in C; (E) longer drying of mask produces a water meniscus around the bases of spheres; (F) AFM topograph of OTS ring patterns; (G) close-up of F; (H) cursor profile for the line in G. Reproduced with permission from ref[72], J.-R. Li et al., *ACS Nano*, 3 (**2009**). Copyright@ American Chemical Society.

For the examples of nanopatterns prepared with vapor deposition of octadecyltrichlorosilane (OTS) shown in Figure 3.3, the film thickness corresponds to a single molecular layer, and the center-to-center distance between nanostructures matches the latex

diameter (Figures 3.3D and 3.3H). Particle lithography combined with vapor deposition has also been applied for fabricating nanostructures of OTS on Au(111), Si(111), and glass substrates.[71, 73] Nanopatterns of organosilanes with different functional groups (e.g. polyethylene glycol, amine, vinyl) have also been produced with particle lithography combined with vapor deposition.[16, 72]

3.5 Patterns of Nanoparticles Produced with Particle Lithography

Particle lithography is a practical route to fabricate nanopatterns of metal nanoparticles over large areas, providing exquisite control of the surface arrangement at the nanoscale. Lithography methods for metal evaporation through shadow masks of mesospheres typically form geometries that are pyrimadal or triangular. The triangular shapes are formed within triple hollow sites of hexagonally-packed spheres. Metal evaporation is accomplished using techniques such as a magnetron sputtering, electron beam evaporation, or thermal evaporation.[87] Among the reports for lithography accomplished with particle masks, approximately 85% of the articles describe studies with nanostructures produced by deposition of heated metal vapors through a shadow mask, and is most commonly referred to as natural lithography[78] or nanosphere lithography (NSL).[80] This practical, high-throughput approach was first developed by Deckman and Dunsmuir and has become the convention for studies of photonic phenomena. Exquisitely regular, periodic nanostructures are essential for studies of size-dependent photonic properties and for measurements with surface enhanced Raman spectroscopy (SERS). Readers are directed to contemporary reviews of approaches for NSL to form metal deposits.[87, 103-105]

Evaporation or sputtering of a metal through a monolayer of colloidal spheres will create structures whose shape is determined by shape of the aperture, or interstices, between the spheres. The size of the apertures is determined by the size of the spheres in a colloidal monolayer. Strategies have been developed to bypass these limitations in an effort to create

either smaller features or different shaped nanostructures. Heating has been shown to cause deformable latex particles to shrink in size, or to flatten against the substrate to create smaller interstitial sites for depositing metals. An approach was developed by Kosiorek et al. to create periodic arrays of metal nanoparticles with pattern sizes as small as 30 nm.[67] For latex masks, the size of the apertures between nanospheres can be reduced by heating. Depositing a metal vapor through an annealed mask was shown to produce smaller nanostructures on the surface compared to nanostructures prepared with masks that were not annealed. An array of cobalt magnetic nanoparticles was fabricated on a silicon substrate using latex masks that were annealed by microwave heating, shown in Figure 3.4. The diameter of a single cobalt nanostructure measured approximately 28 nm, which closely matches the size of the apertures within the latex mask. The Co nanoparticle arrays maintain the interparticle spacing and order of the latex mask.

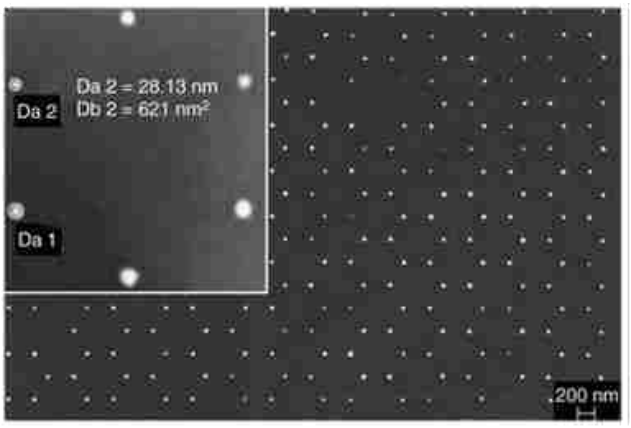

Figure 3.4 Arrays of Co nanoparticles on silicon substrate prepared by annealing 540 nm latex masks, followed by metal evaporation of Co. Reproduced with permission from ref[67], A. Kosiorek et al., *Small*, 1, (**2005**). Copyright@ John Wiley & Sons, Inc.

Ring-shaped arrangements of metal nanoparticles were produced by particle lithography using solution deposition of metal salts. Metal nanorings composed of copper, gold, and platinum nanoparticles were prepared on Si(100) and HOPG substrates using a particle lithography strategy developed by Bayati et al.[13] A surface template of 505 nm latex spheres were immersed in a 10 mM solution of metal salts for 2 hr, followed by reduction with $NaBH_4$.

The latex template was rinsed away with chloroform to disclose arrays of metal nanorings with periodicities corresponding to the diameter of the latex nanospheres. Examples are shown by the AFM views in Figures 3.5A, 3.5B and 3.5C for Cu, gold, and Pt nanorings prepared on Si(100) substrates, respectively. The average height and diameter of the metal nanorings measured 5.7 $\pm$ 0.8 nm and 167.3 $\pm$ 8.9 nm, respectively. Ring-shaped nanostructures of gold have been shown to exhibit tunable surface plasmon resonances in the near infrared region.[106]

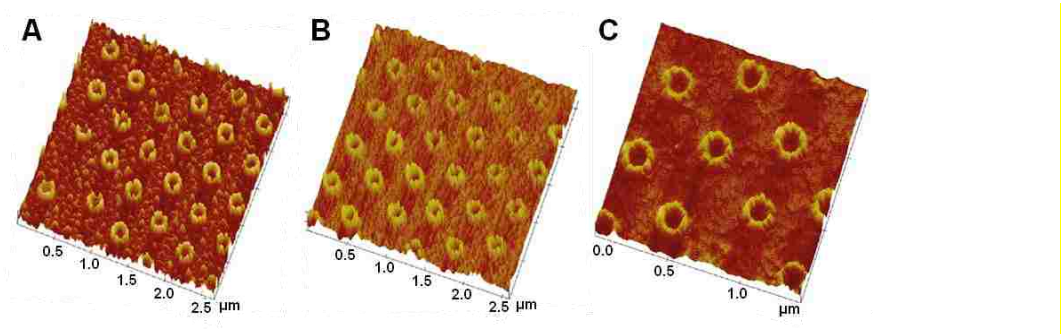

Figure 3.5 Metal ring nanoarrays produced by reducing metal precursor through the interstices between PS nanospheres. Topography AFM views of (A) Cu, (B) Au, and (C) Pt nanorings formed on Si(100) substrates. Reproduced with permission from ref[13], M. Bayati et al., *Langmuir*, 26, (**2010**). Copyright@ American Chemical Society.

A solution-based particle lithography approach known as "two-particle" lithography was developed by Lewandowski et al. for controlling the arrangement of cysteine-coated CdS quantum dots on surfaces.[75] Monodisperse latex mesoparticles (or colloidal silica) were mixed with cysteine-coated CdS quantum dots in an aqueous solution. Drying the aqueous mixture of mesoparticles and nanoparticles spontaneously produces ring arrangements of nanoparticles on mica substrates, as shown in Figure 3.6. As water evaporates during the drying step, the liquid carries the nanoparticles to form circular arrangements of nanoparticles surrounding the bottom area of the mesospheres. The latex template is removed by a rinsing step, and the smaller nanoparticles persist and remain attached to the surface. The cysteine-coated CdS rings measure 140 $\pm$ 12 nm in diameter, with approximately 10% surface coverage. There are 12 nanostructures within the 2 x 2 μm^2 frame in Figure 3.6B, which scales up to 300 million nanostructures per 1 x

1 cm^2. A cursor profile reveals that the height of the nanostructures is 1.9 $\pm$ 0.6 nm (Figure 3.6C), which corresponds to the thickness of a single layer of the nanoparticles.

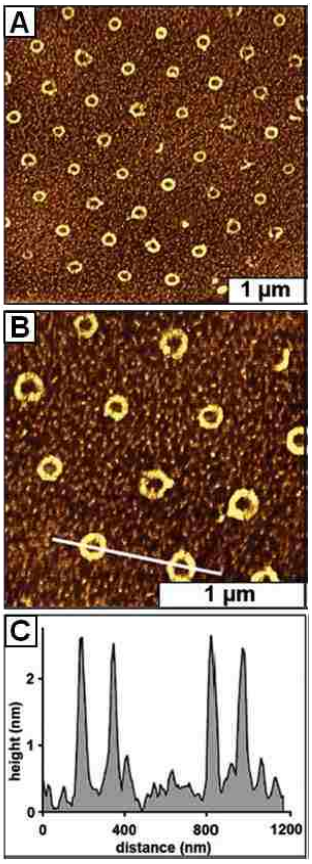

Figure 3.6 Ring-shaped nanostructures of cysteine-coated CdS nanoparticles prepared by two-particle lithography using 500 nm silica spheres: (A) AFM topography image; (B) close-up view of A; (C) cursor profile for the line in B. Reproduced with permission from ref[75], B. R. Lewandowski et al., *J. Phys. Chem. C*, 113, (**2009**). Copyright@ American Chemical Society.

Two-component patterns of organosilanes prepared by particle lithography furnish a spatially-selective platform for binding metal nanoparticles, as demonstrated by Li et al.[72] Gold nanoparticles were selectively attached onto thiol-functionalized organosilane nanopatterns, which were prepared by particle lithography combined with vapor deposition.[72] Nanostructures of OTS were first prepared by vapor deposition through 300 nm latex masks. Removal of the surface mask generates a thin film of OTS with periodically arranged pores of uncovered Si(111) substrate. The uncovered areas were backfilled by immersion in a solution of 3-

mercaptopropyltrimethoxysilane (MPTMS). Thiol-terminated MPTMS patterns define the sites for selectively binding gold nanoparticles via S-Au chemisorption by immersion in a solution of gold nanoparticles (Figure 3.7A). Gold nanoparticles bind selectively on areas patterned with MPTMS, as shown in Figure 3.7B. The clusters contain around 2-5 gold nanoparticles, as shown by the 1 x 1 μm^2 view in Figure 3.7C. The average height and periodicity of the patterned gold clusters measured 13 $\pm$ 3 nm and 310 $\pm$ 14 nm, respectively (Figure 3.7D).

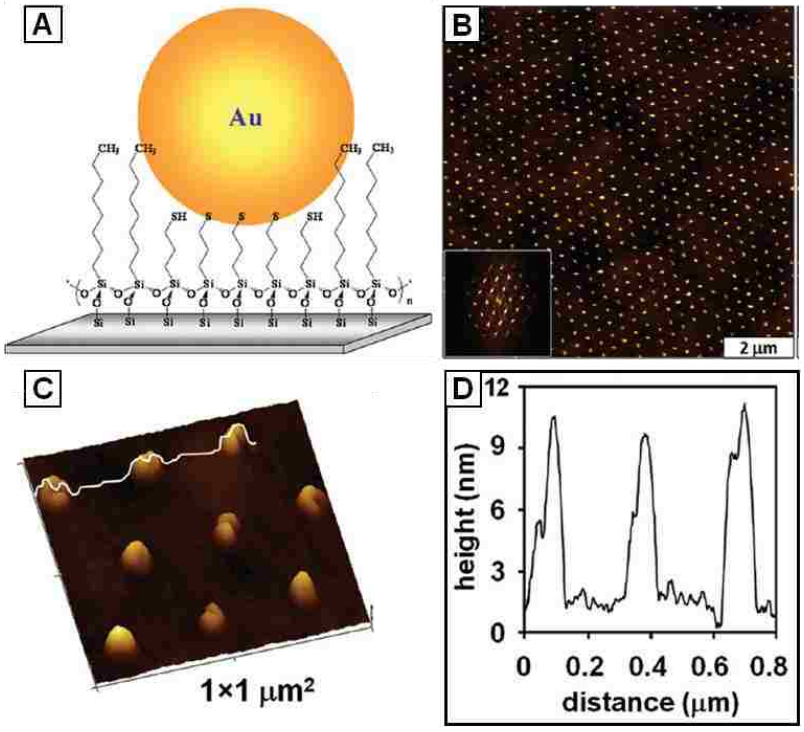

Figure 3.7 Defining spatial selectivity using organosilane nanopatterns for selective immobilizaton of gold nanoparticles. (A) Gold nanoparticles selectively attach onto areas with MPTMS; (B) 10 x 10 μm^2 topography view of periodic arrays of gold nanoparticle clusters on Si(111) (inset shown is the corresponding FFT image); (C) zoom-in view of B; (D) height profile for the line in C. Reproduced with permission from ref[72], J.-R. Li et al., *ACS Nano*, 3, (**2009**). Copyright@ American Chemical Society.

3.6 Nanopatterns of Proteins Fabricated by Particle Lithography

High throughput fabrication methods for nanopatterning proteins are important for the development of protein-based biosensors and biochips.[107-109] Particle lithography has been used for generating protein patterns at the nanoscale by evaporative drying of an aqueous mixture of

protein and latex. Ordered arrays of bovine serum albumin (BSA), Immunogobulin G (IgG) and staphylococcal protein A (SpA) were fabricated using particle lithography, by Garno et al.[15, 76, 110] An example of arrays of BSA nanopatterns produced using 500 nm polystyrene latex as a structural template is shown in Figure 3.8, in which proteins are attached directly to mica substrates by physical adsorption.[76] To create the BSA nanopatterns, the protein and latex mesospheres were mixed in aqueous solution, deposited on mica, and then dried under ambient conditions. As the water evaporates during drying, the mesospheres self-assemble on the surface to produce crystalline assemblies. Proteins surround the latex template to form ring or hole patterns depending on BSA : latex ratios, as shown in Figure 3.8. The latex mesospheres were rinsed from the surface with deionized water. However, the BSA remains attached to the substrate to form a single layer of protein nanostructures. Ring nanostructures of ferritin were prepared using evaporative particle lithography by Daniels et al., for studies of magnetic response of individual ferroproteins at the molecular level.[111]

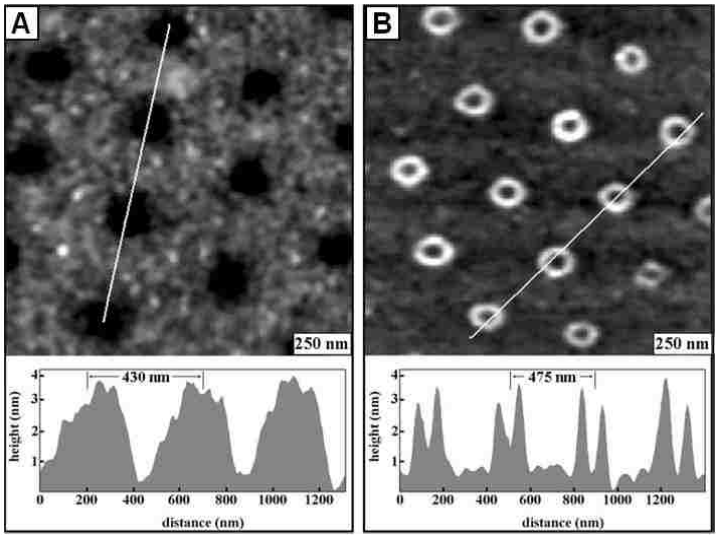

Figure 3.8 Periodic arrays of BSA nanostructures on mica(0001) prepared with 500 nm latex spheres. (A) AFM topography image and corresponding cursor profile of well-defined pores of uncovered substrate within a BSA film prepared with a protein : latex ratio of 61,000 : 1; (B) topograph and height profile of ring-shaped BSA nanostructures formed using a ratio of 30,500 : 1. Reproduced with permission from ref[76], J.-R. Li, *Analyst*, 131, (**2006**). Copyright@ the Royal Society of Chemistry.

A strategy for preparing lysozyme nanostructures on patterns of organosilanes was developed by Cai et al. using particle lithography.[77] A monolayer film of undecenyltrichlorosilane was prepared on a silicon substrate, and then oxidized using a solution of $KMnO_4/NaIO_4$ to form carboxylic acid headgroups. Polystyrene nanospheres were then deposited onto the hydrophilic surface to form a mask for further patterning steps. Vapor phase deposition of methyl-terminated OTS was applied to the surface mask. After removal of the spheres, periodic nanopatterns of UTS_{ox} and OTS were generated to define sites for protein adsorption. Lysozyme was selectively deposited onto surface areas with carboxylic acid. Reactions with an antibody demonstrated that the bioactivity was preserved for the lysozyme patterns, as shown in Figure 3.9.

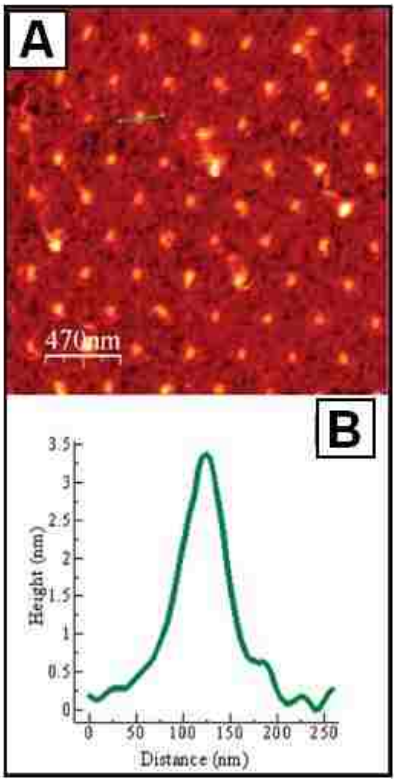

Figure 3.9 Adsorption of antibody on lysozyme nanopatterns prepared on silicon wafers using particle lithography combined with surface silane chemistry. (A) Topography image of the lysozyme nanoarrays after antibody adsorption; (B) cursor profile corresponding to the green line in **A**. Reproduced with permission from ref[77], Y. Cai et al., *Langmuir,* 21, (**2005**). Copyright@ American Chemical Society.

3.7 Future Prospectus of Particle Lithography

Particle lithography provides a practical, inexpensive, and materials-general route for rapidly producing arrays of nanostructures on surfaces. There is a continuing challenge to press the limits for patterning individual proteins and isolated nanoparticles, to enable studies of size-dependent properties and molecular-level phenomena. The most promising directions for lithography with mesoparticles are to develop strategies with nanoscale spatial patterning to incorporate innovative schemes of chemical reactions, to enable directed assembly of desired functionalities with multiple components and molecular designs. Future directions for patterning strategies will likely incorporate more sophisticated reactions for constructing hierarchical macromolecular structures, with multifunctionalities.

CHAPTER 4. PARTICLE LITHOGRAPHY COMBINED WITH VAPOR DEPOSITION: A TOOLKIT FOR STUDYING CONFINED SURFACE REACTIONS IN NANOSCALE LIQUID VOLUMES*

4.1 Introduction

For emerging applications in nanotechnology, high throughput methods are needed for fabricating nanostructures with tunable properties and sizes for sensors,[1-2] catalysis,[3] molecular separations[4] and electronics.[5] Patterns of organosilane self-assembled monolayers (SAMs) are of interest for molecular studies because various head group functionalities and chain lengths can be used to tailor the surface properties.[112-113] Organosilane SAMs are used for sensors,[114-115] molecular electronic devices,[116] lubricants[117] and semiconductor coatings.[118] A benefit of organosilane SAMs is the suitability for using a range of different substrates, such as silicon oxide, metal oxides, quartz, glass, gold and mica.[102] Organosilane SAMs are chemically robust due to covalent bonds to the surface and between the bridges of the siloxane network. As a result, functionalized organosilanes have been used as molecular platforms for further chemical modification or binding steps.[119-120]

Monolayers of organosilanes have been prepared on surfaces using either techniques of solution immersion[121-122] or vapor deposition.[123-124] Studies have shown that the overall quality of the SAM that is formed depends intrinsically on the experimental conditions used during film preparation, such as the type of solvent used,[120, 125] nature of the substrate,[121, 126] reaction temperature,[120, 127-128] precursor concentration[129] and the size and chemical structure of the organosilane.[126, 130] In particular, the amount of water that is present on the surface has been shown to greatly influence the quality of the film.[112, 122, 131] Surface bound water initiates hydrolysis of organotrichlorosilanes to form silanols, which then form siloxane linkages to surface silanol (Si–OH) groups or undergo condensation for polymerization of organosilanols.

*Reproduced with permission from Elsevier.

Patterns of organosilanes can be used for integrating various molecules into well-defined surfaces. Strategies of lithography for micropatterning organosilanes on surfaces include microcontact printing,[132-133] photolithography[134] and electron beam lithography[135-136]. Nanopatterning of organosilanes has been accomplished using different approaches for scanning probe lithography such as dip-pen nanolithography,[137] bias-induced lithography[138] and nanoshaving.[139]

Particle lithography provides capabilities for rapidly producing periodic nanopatterns over large areas and has been applied for patterning polymers,[60-61] metals,[62-67] SAMs[68-70] and proteins.[15, 76-77] Particle lithography offers a versatile alternative for nanofabrication with the benefit of high throughput and has also been referred to as colloidal lithography,[79] natural lithography,[78] nanosphere lithography,[80-81] or evaporative lithography.[14] Monodisperse mesospheres of latex or colloidal silica spontaneously assemble on flat surfaces to form close packed structures with regular geometries and interparticle spacing.[87] The 2D arrays of mesoparticles furnish an evaporative mask or a structural template for guiding the deposition of various materials. The area of contact between the spherical particles and the substrate remains protected from chemical modification during the patterning process.

We have developed a direct method of accomplishing particle lithography using chemical vapor deposition to nanopattern organosilanes on different substrates (e.g., silicon wafers, glass, mica and gold surfaces).[71-72] In this report, we demonstrate the applicability of particle lithography with vapor deposition for preparing multilayered nanostructures of organosilanes with different terminal groups: amine-, PEG- and vinyl-terminated organosilanes. The self-polymerization reactions of ω-functionalized silanes were investigated using atomic force microscopy (AFM) to obtain molecular-level views of ring-shaped nanostructures prepared using particle lithography. The influence of the following parameters has been studied as a function of

terminal group chemistry and molecular length: the surface density, the thickness of the SAMs, the widths of the patterns, periodicity, and overall surface coverage.

4.2 Experimental Details

4.2.1 Materials and Reagents

Boron-doped polished Si(111) wafers were obtained from Virginia Semiconductor Inc. (Fredericksburg, VA) and cut into 1×1 cm^2 squares. Concentrated sulfuric acid (98.0%) and hydrogen peroxide (30%) were used as received from Sigma-Aldrich. Size-sorted monodisperse polystyrene latex mesospheres (1 wt.% solution) with sulfate surface groups with particle diameters of 100, 150, 200, 300 and 500 nm were obtained from Thermo Scientific (Waltham, MA) and used as surface masks during vapor deposition of organosilanes. Octadecyltrichlorosilane (OTS), N-(6-aminohexyl)-3-aminopropyltrimethoxysilane (6-AAPTMS), 2-[methoxy-(polyethyleneoxy)propyl]trichlorosilane (PEG-silane) and 10-undecenyltrichlorosilane (UTS) were purchased from Gelest (Morrisville, PA) and used without further purification. Anhydrous ethanol was purchased from Pharmco (Aaper, TX).

4.2.2 Substrate Preparation

Silicon substrates were cleaned by soaking in piranha solution (3:1 v/v ratio of concentrated sulfuric acid and 30% hydrogen peroxide) for 1 h. Piranha solution is corrosive and should be handled with caution. After cleaning, surfaces were rinsed with copious amounts of deionized water purified by a Millipore Milli-Q purification system (18 MΩ cm, Boston, MA) and dried in air.

4.2.3 Basic Steps for Nanofabrication of Organosilane Ring Patterns

Nanopatterns of organosilanes with different terminal groups were prepared following a procedure that was previously described for octadecyltrichlorosilane (OTS).[71] An overview of the procedure for particle lithography with vapor deposition is shown in Figure 4.1. First, latex

mesospheres were washed to remove surfactants by three cycles of centrifuging (15 min cycle^{-1}) at 14,000 rpm. The supernatant was discarded and the latex mesospheres were resuspended in deionized water with vortex mixing. A drop (20 μL) of the latex suspension was deposited on a clean Si(111) substrate and dried for 12 h in ambient conditions (25 C, relative humidity ~55%).

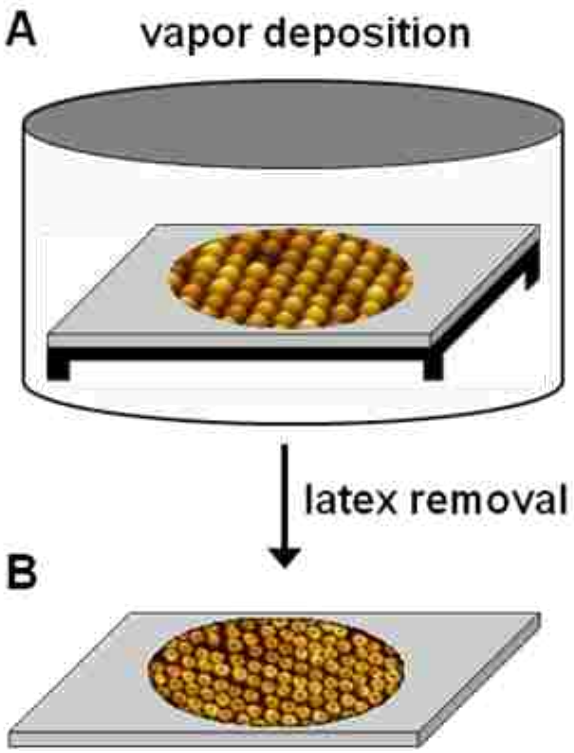

Figure 4.1 Fabrication of organosilane nanostructures using particle lithography combined with chemical vapor deposition. (A) A crystalline layer of latex mesospheres provides an evaporative mask for nanopatterning. The masked substrate is placed in a sealed vessel containing a small volume of neat organosilane and then is heated at 70 °C to generate vapors. (B) After the latex mask is rinsed away an array of organosilane ring nanopatterns is formed.

As water evaporates during the ambient drying step, the latex spheres are pulled together by capillary forces to form close-packed layers on the surface. The dried film of latex provides a mask for nanolithography; however nanoscopic amounts of water persist under the spheres at the surface to uniformly produce a water meniscus around the base of each sphere. The water residues define the locations for organosilanes to bind. The substrates with masks of latex films were placed on a platform within a glass container, then a small volume (300 μL) of neat

organosilane was added to the bottom of the vessel. The container was sealed and placed into a heated oven for 8 h (Figure 4.1A). We have established empirically that it is not necessary to heat the samples to the boiling point of the organosilane, sufficient vapor is generated at 70 °C to produce nanopatterns. During the heated vapor step, organosilanes bind covalently only on area of the surface where a water meniscus is present. Areas of the surface where the latex particles make contact with the substrate remain protected from vapor deposition. In the final step, the film of latex mesospheres was removed by rinsing and sonicating in deionized water and ethanol several times (Figure 4.1B). After removal of the latex mask, covalently bound organosilanes persist on the surface to reveal periodic arrays of ring-shaped nanostructures with dimensions corresponding to the diameter of the latex masks.

4.2.4 Atomic Force Microscopy

Samples were characterized using either a model 5500 or 5600 LS scanning probe microscope (Agilent Technologies, Chandler, AZ) with acoustic AC-mode (tapping) AFM. Silicon probes with an average resonance frequency of 190 kHz and spring constants ranging from 20 to 95 Nm^{-1} (Nanoscience Instruments, Inc., Phoenix, AZ) were used for imaging. Digital images were processed with Gwyddion (version 2.9) open source software which is supported by the Czech Metrology Institute.[140]

4.2.5 Quantitative Measurements

Measurements of surface coverage (θ) were obtained with Image-Tool (UTHSCSA, San Antonio, TX).[141] The percent surface coverage was estimated from AFM images by averaging measurements from representative images from different areas of multiple samples. To measure the periodicity between nanopatterns, the center-to-center distances between adjacent pores were measured for at least 100 nanostructures using cursor line profiles from several AFM topographs acquired for different areas of the surface. The average thickness of organosilane nanopatterns

was measured with height profiles of AFM topographs acquired for at least 100 rings from different areas of the sample, referencing the uncovered areas of the substrate as a baseline.

4.3 Results and Discussion

4.3.1 Control of Size and Surface Density of Nanopatterns Prepared from OTS

Images of methyl-terminated nanopatterns prepared with OTS from different sizes of latex masks are shown with successive zoom-in AFM views (Figure 4.2). For ring-shaped nanostructures prepared by particle lithography, AFM topographic views show that arrays of OTS rings are generated with highly regular geometries. With changes in the diameter of the spheres, the density of ring nanopatterns correspondingly changes according to the periodicity of the latex mask. Line profiles traced across the nanopatterns reveal that the baselines within the pores of the rings are at the same level as the surrounding uncovered areas of the substrate, which indicates that OTS did not adsorb within the center of the rings. The absence of adsorbates within the pore areas enclosed by the rings demonstrates that latex spheres were effective surface masks for chemical vapor deposition. Relatively few defects are observed in the wide area views displayed in the first column (Figure 4.2, left images). Successive zoom-in views are shown in the second and third columns of Figure 4.2, which show fine details of the size and uniformity of the nanostructure geometries. From the cursor line profiles shown in the fourth column of Figure 4.2, the average periodicity for samples prepared with 495, 200 and 100 nm latex diameters measured 502 ± 5, 218 ± 8 and 112 ± 6 nm, respectively.

Changing the latex diameter provides a toolkit for tuning the surface density and sizes of organosilane nanopatterns. The periodicity of the latex mask dictates the center-to-center distance between rings; however the organosilane patterns are much smaller than the latex particles. Evaporative masks of mesoparticles provide an excellent framework for controlling the overall periodicity and long-range order. When combining particle lithography with vapor

deposition, ring structures form around the base of each sphere where a water meniscus is located. Nanoscopic residues of water are confined around the base of each latex particle, which provides reaction sites for the hydrolysis and condensation of organosilanes. Essentially, particles are used to pattern water residues on the surface because latex films were dried in a humid, ambient environment. The volumes of these meniscus sites are exquisitely regular in dimension at the nanoscale to define a 3D nanosized container for silanation to occur. Vapor deposition of organosilanes takes place selectively at the locations of water residues, mediated by a two-step reaction mechanism of hydrolysis and condensation.[71] Since organosilanes bind covalently to silicon substrates, the organosilane nanostructures produced by particle lithography are highly robust to effects of oxidation and heat.

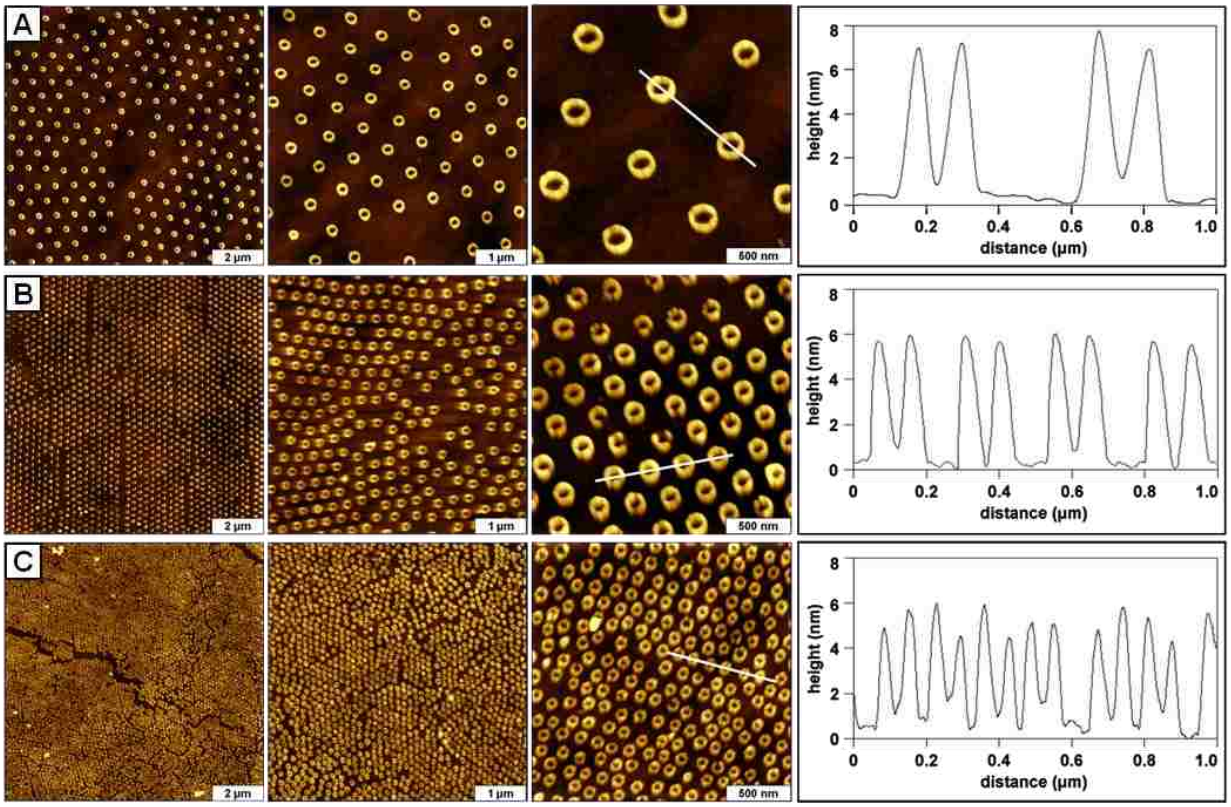

Figure 4.2 Ring-shaped nanopatterns of OTS prepared on Si(111). Topography images of nanopatterns prepared with latex diameters of (A) 495 nm, (B) 200 nm and (C) 100 nm, acquired with tapping mode AFM.

One would expect that the size of the water meniscus would scale proportionately with the diameter of the mesoparticles. A larger latex mesoparticle would have a water meniscus that is wider and taller in dimension. Cursor measurements of the ring nanopatterns in Figure 4.2 provide a means to test this prediction. The widths of the rings changed from 230 ± 6 nm to 170 ± 5 nm to 97 ± 7 nm for latex sizes of 495, 200 and 100 nm, respectively. Interestingly, the changes in the heights of the rings also scale with the sizes of the mesoparticles: from 7.2 ± 0.6 nm to 5.8 ± 0.4 nm to 5.2 ± 0.6 nm correspondingly for latex diameters of 495, 200 and 100 nm. The thickness of a monolayer of OTS has been reported to measure within the range of 2.26 and 2.76 nm.[130, 142-144] Thus, the thicknesses of the patterned OTS nanostructures correspond roughly to a double layer for 100 nm latex, a triple layer for 200 nm latex and four layers with 495 nm spheres. Multilayer structures of organosilanes are produced by self-polymerization reactions, therefore, a key to producing monolayer films is to carefully control the amount of water present during the reaction.[112, 122, 131] The thickness of OTS patterns is neatly controlled by the height of the water meniscus, such that a wider and taller water meniscus is produced for larger spheres of latex.

By changing the size of the latex mesospheres used as masks, the spatial distribution and surface density of organosilane nanopatterns can be fine-tuned. The number of nanostructures scales predictably from 12 rings (Figure 4.2A) to 64 (Figure 4.2B) and 224 (Figure 4.2C) rings within the 2×2 μm^2 frames shown in the third column of Figure 4.2. This scales up to a surface density of 3×10^8, 2×10^9 and 6×10^9 rings per 1×1 cm^2 for OTS nanopatterns prepared with latex diameters of 495, 200 and 100 nm, respectively. Thus, the particle lithography toolkit provides an approach for selecting the periodicity of ring nanopatterns, enabling nanoscale control of the number density of nanopatterns.

4.3.2 Effects of Headgroup Chemistry for the Surface Coverage of Organosilane Nanopatterns

Beyond our initial studies of methyl-terminated nanopatterns of OTS, organosilanes with different functional groups (e.g., vinyl-, PEG and amine-terminated silanes) were prepared using particle lithography combined with vapor deposition. Arrays of ring nanostructures of UTS, PEG-silane and 6-AAPTMS prepared with 300 nm latex are demonstrated with tapping mode AFM images shown in Figure 4.3A–C, respectively. Discrete changes are observed for ring shapes according to the chemical composition of the nanopatterns, even within the larger 8×8 μm^2 topographic views (Figure 4.3, left column). Magnified views of the surface areas reveal that the hexagonal packing arrangement of the latex mask is preserved for all three cases. Geometry changes of the ring widths and heights are apparent for the different organosilane moieties. For the examples shown in Figure 4.3, simultaneous samples were prepared with masks of 300 nm latex for different terminal moieties. The widths of the rings (FWHM±SDV) measured 55 ± 3 nm, 72 ± 4 nm and 61 ± 6 nm for UTS, PEG-silane and 6-AAPTMS, respectively. Comparing the means using a paired t-test, these values are significantly different at the 99% confidence level (n=50). Thus, changes in the molecular lengths and terminal groups of organosilanes produce differences in lateral spreading of the patterns across the surface within the confined volume of a water meniscus.

Multilayered structures were observed for patterns of all three organosilanes of Figure 4.3, with the tallest heights observed for vinyl terminated UTS. Organosilanes with reactive head groups can form multilayers either through head-to-head interactions, head-to-tail assembly, or self-polymerization reactions. The shortest nanostructures were obtained with 6-AAPTMS, which has a triethoxy end group rather than trichlorosilane. Referencing the uncovered areas of silicon substrate as a baseline, a thickness of 9.2 ± 0.4 nm was measured for UTS nanopatterns

(Figure 4.3A), which has a theoretical length of 1.6 nm for a single layer.[145] This would correspond to approximately six molecular layers of UTS for fully extended, upright molecules. Nanostructures prepared with PEG-silane (Figure 4.3B) measured 7.9 ± 0.6 nm in height which corresponds to a thickness of 4–5 molecular layers when compared to the expected thickness of a monomolecular PEG layer of 1.0 to 1.7 nm.[146] The length of a fully extended silane molecule with seven PEG units is 3.1 nm.[146] An average thickness of 4.3 ± 0.4 nm was measured for ring nanostructures of 6-AAPTMS (Figure 4.3C), which corresponds to approximately three layers, the known thickness of a monolayer of 6-AAPTMS is 1.3 nm.[123]

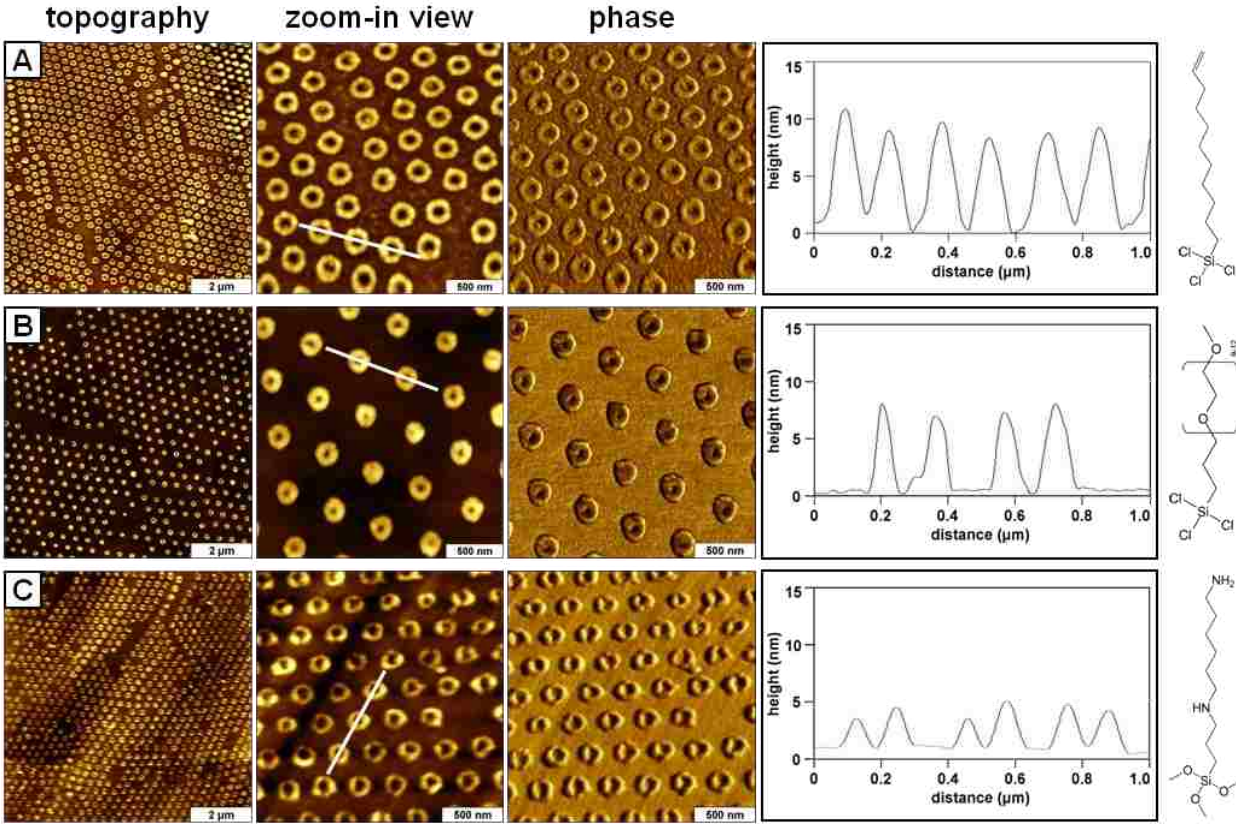

Figure 4.3 Periodic arrays of organosilane nanopatterns with different functional groups fabricated on Si(111) using 300 nm latex masks. Tapping mode images and height profiles of (A) vinyl-terminated UTS nanostructures, (B) PEG-silane rings and (C) amine-terminated 6 AAPTMS nanopatterns.

Trifunctional organosilanes are highly reactive in the presence of water and can both oligomerize and polymerize at a surface or in solution, depending on experimental conditions.[147-148] For 6-AAPTMS, the amino headgroup can form a hydrogen or ionic bond with the methoxysilane group of another AAPTMS molecule or its hydrolyzed form.[123] Also, the amino group can self-catalyze the hydrolysis step to produce multilayers.[149] Triethoxysilanes were reported to be less reactive to water than trichlorosilanes and therefore would be likely to produce fewer layers within the ring nanostructures. Since all three systems were prepared simultaneously with 300 nm latex, the size and volume of the water meniscus should be comparable for the experiments of Figure 4.3. This indicates that the reactivity of the terminal group affects the surface assembly into multilayers, with the order of reactivity vinyl>>PEG>amine functional groups for the propensity to form multiple layers.

Well-defined pores are observed at the center of the ring nanopatterns in the 2×2 μm^2 zoom-in topographic views and simultaneously acquired phase images, pinpointing the locations where the latex spheres were removed. Phase images provide a sensitive map of the surface morphology, as well as indicating changes in surface chemistry. The phase images in the third column of Figure 4.3 clearly reveal differences in surface chemistry between the organosilane rings and surrounding areas of the silicon substrates. Segmented domains of UTS are apparent in the phase image shown in Figure 4.3A, which can be an indication of disordered multilayers. Small clusters are also present on areas of the surface between UTS ring patterns. The phase images acquired for PEG-silane and 6-AAPTMS, however, reveal nanostructures with a continuous, smooth morphology without disconnections. The average lateral periodicity for UTS, PEG-silane and 6-AAPTMS nanopatterns measured 296 ± 8, 311 ± 6 and 298 ± 5 nm, respectively. These values closely match the expected 300 nm diameter of latex mesospheres used as masks for particle lithography, within 3% variation.

A number of experimental parameters can influence the self-assembly of organosilanes, such as the type of solvent used,[120, 125] the nature of the substrate,[121, 126] reaction temperature[120, 127-128] and water content.[131, 150-151] The molecular structure and reactivity also influence how the molecules self-organize on surfaces in both vertical and lateral directions. An important contribution of using particle lithography for studies of organosilane chemistry is that the reaction volumes can be spatially confined to take place within a nanoscopic meniscus area. This ability to spatially control surface reactions can furnish insight for the chemical mechanisms of surface assembly and interchain self-polymerization of organosilanes within confined volumes.

Quantitative comparisons of the changes in the number density of rings of UTS, PEG-silane and 6-AAPTMS nanostructures can be made as a function of latex diameter (Figure 4.4). The diameter of latex spheres directly defines how many nanostructures will be generated. The surface densities were found to be quite consistent for UTS, PEG-silane and 6-AAPTMS ring nanopatterns (Figure 4.4). The number of nanostructures ranges from 1 to 12 billion nanostructures cm^{-2} depending on the diameter of latex. These results demonstrate the powerful advantages of using particle lithography for creating nanostructures; basic steps of chemistry can be used to rapidly and predictably generate billions of nanopatterns with exquisitely regular geometries and periodicity.

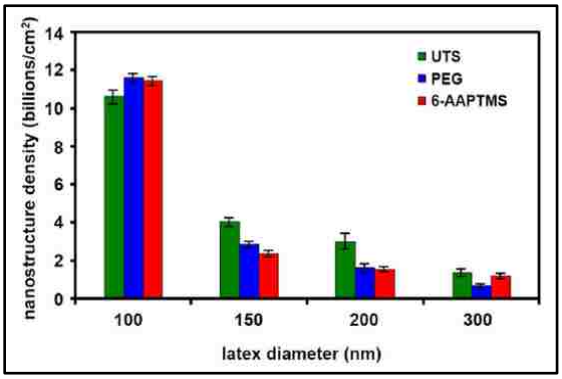

Figure 4.4 Changes in the surface density for organosilane nanostructures of UTS (green), PEG silane (blue) and 6-AAPTMS (red) prepared on Si(111) using different diameters of latex spheres.

The surface coverage (θ) was evaluated for UTS, PEG-silane and 6-AAPTMS nanopatterns using estimates from counting pixels in AFM images (Table 4.1). Overall, the percent surface coverage of nanostructures for UTS, PEG-silane and 6-AAPTMS were fairly reproducible for specific latex diameters, ranging from 13 to 24% for 300 nm latex and from 34 to 40% for 150 nm latex diameter. As a generic trend, the results in Table 4.1 indicate that for each molecule the overall surface coverage increases with decreasing latex diameters. However, for samples prepared with 100 nm latex, the UTS surfaces had a significantly higher coverage of 75%, which was found to be a reproducible effect for samples prepared on different days. This is considerably greater than the values observed for nanopatterns of OTS, PEG-silane and 6-AAPTMS and is an interesting anomaly which merits further study.

Table 4.1 Surface coverage estimates for organosilane nanostructures with different terminal groups.

Latex diameter [nm]	θ_{OTS}[%]	θ_{UTS}[%]	θ_{PEG}[%]	$\theta_{6\text{-}AAPTMS}$[%]
100	44 ± 2.3	75 ± 1.3	45 ± 1.5	50 ± 3.6
150	32 ± 1.6	38 ± 2.4	34 ± 2.9	40 ± 2.5
200	27 ± 1.9	33 ± 1.8	24 ± 0.8	34 ± 1.0
300	20 ± 1.2	24 ± 0.9	13 ± 0.7	22 ± 1.6

4.3.3 Long-Range Order and Periodicity of PEG-Silane Nanopatterns

The capabilities of particle lithography for patterning of broad areas of the surface are demonstrated in Figure 4.5. Nanopatterns of PEG-silanes prepared with 150 nm latex are viewed within a 30×30 μm^2 topography frame. Within this relatively large area of the sample the exquisitely regular geometries and arrangement of nanopatterns are apparent. The arrays of PEG-silane rings span the entire surface and maintain the long-range order of the latex mask, with periodicities extending over micron regions. Very few defects (e.g., point defects and misaligned

domains) are observed. Missing patterns and line defects in mesosphere masks can be attributed to sphere polydispersity, nanoscale defects of the underlying substrate and packing defects from shrinkage during the drying step.[152] A number of approaches have been reported for minimizing the density of defects for scale-up to wafer dimensions.[82, 87, 153-155] The reciprocal space of the topography frame is displayed in the inset of Figure 4.5 with 2D fast Fourier transform (FFT) analysis, as further confirmation of the well-defined periodicity of the nanopattern array. The FFT analysis provides a quantitative picture of the long-range order of the array of PEG-silane nanostructures.

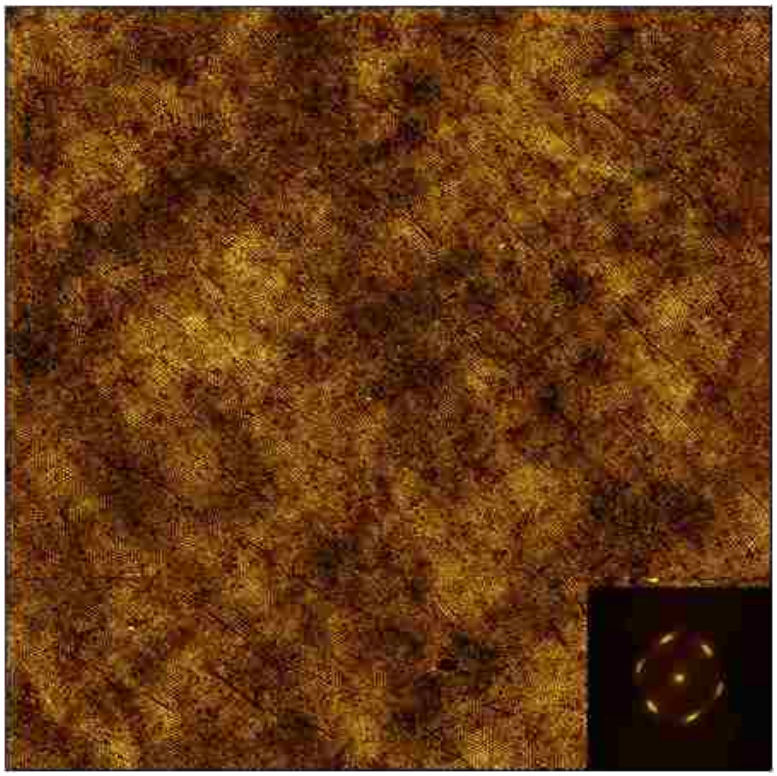

Figure 4.5 The high throughput capabilities of particle lithography are demonstrated with a wide view AFM image of PEG-silane ring nanostructures prepared with 150 nm latex. The inset shows an FFT spectrum generated from the 30×30 μm^2 topograph.

Particle lithography provides a versatile toolkit for high throughput nanopatterning of covalently attached organosilanes, with the practicality of designing surface reactivity by using designated functional groups. These compelling new results with nanoscale particle lithography

provide insight about the propensity of reactive moieties to form multilayers and offer new possibilities for accomplishing surface reactions within the confined volume of 3D liquid meniscus area as determined by the diameter of latex masks. Our results with ω-functionalized organosilanes indicate that the most critical factors for surface assembly with particle lithography combined with vapor deposition are the nature of the head group, the endgroup of the parent molecule, as well as the chain length and the size of the water meniscus. Control of the humidity may lead to different thicknesses of the multilayers and studies are in progress to evaluate the specific changes in the heights and lateral dimensions of the rings as a function of humidity. Overall, the ring geometries, number density and surface coverage are exquisitely reproducible at the nanoscale and are primarily determined according to the diameters of the latex masks. Different chemical functionalities presented at the interface enable molecular level control of surface reactivity for the nanopattern designs.

4.4 Conclusions

The procedure for preparing nanostructures using particle lithography and vapor deposition of organosilanes requires only a few chemical steps and does not require sophisticated equipment or expensive reagents. Billions of high quality nanostructures are rapidly generated with basic steps of wet chemistry, with the versatility of using a range of different substrates such as silicon, glass, gold or mica. Particle lithography combined with vapor deposition of organosilanes offers synthetic flexibility, extending to trialkoxy or trichlorosilane end groups, provides advantages of covalent surface linkages and produces exquisitely regular nanostructures with tunable surface coverage and density of nanostructures. From a scientific perspective, particle lithography enables spatial confinement of silanation reactions within nanoscopic volumes of a water meniscus. This provides a way to obtain molecular-level views of the products of reactions after surface assembly using AFM analysis. A convenient and practical

toolkit is furnished by particle lithography to spatially direct and control surface reactions of organosilanes, which will lead to future studies of more complex multi-molecular architectures and designs using immersion strategies to backfill nanopatterns.

CHAPTER 5. NANOSTRUCTURES OF FUNCTIONALIZED GOLD NANOPARTICLES PREPARED BY PARTICLE LITHOGRAPHY WITH ORGANOSILANES*

5.1 Introduction

Considerable advances have been achieved in developing approaches to synthesize functional nanoparticles with designed properties (optical, electronic, catalytic, magnetic, etc.) by tailoring the size, composition and shell chemistry of metal nanoparticles. However, the development of convenient, high throughput methods for fabricating surface structures of nanoparticles presents a further challenge for materials research. Relatively few methods have capabilities for placing nanoparticles on surfaces with alignment at scales below 500 nm. High throughput patterning of nanoparticles is a requirement for potential nanotechnology applications in miniaturized devices and sensor platforms.

Addition of designed organic ligands to the surface of metal nanoparticles changes the nature of the material and imparts new properties for multiple functions, such as fluorescence, reactivity or chemical specificity.[156-157] There is considerable precedent for the synthesis of monolayer-protected nanoparticles with different shell chemistries.[158-159] However, there are few reports that present approaches for preparing surface patterns of these nanomaterials at length scales below tens of microns. Particle lithography is a versatile, high-throughput approach for controlling the organization of nanomaterials on surfaces and has also been referred to as colloidal lithography,[79] natural lithography,[78] nanosphere lithography[80] or evaporative lithography.[14] Millions of nanostructures can be generated on surfaces with relatively few defects to reproducibly prepare well-defined arrangements. Most articles that have been published (630 of 846) use the term nanosphere lithography or NSL to refer to evaporation of heated metal films through a shadow mask of latex spheres to create single element nanostructures. Metal

*Reproduced with permission from the American Chemical Society.

nanostructures formed with NSL have size-tunable properties for applications as SERS substrates or as photonic crystals. Other deposition approaches that have been reported with NSL include argon ion milling, reactive ion etching and electrodeposition of metals. Particle lithography is a generic approach for creating patterns for a diverse range of materials, such as polymers,[60-61] metals,[62-67, 160] organic thin films[68-70, 161] and proteins.[15, 76-77] With particle lithography, films of latex or colloidal silica furnish 2D arrays of mesospheres as a lithographic mask or template for guiding the deposition of different materials and organic thin films. Monodisperse mesospheres spontaneously self-assemble on flat surfaces when dried, to form hexagonal arrays for high-throughput patterning.[87] The lithographic mask of spherical particles protects the surface during chemical treatments, and can be conveniently removed by subsequent steps of solvent rinsing, dissolution or sonication.

A practical strategy for patterning metal nanoparticles is to prepare nanopatterns of self-assembled monolayers (SAMs), and use the spatial selectivity of functional headgroups of the molecules to subsequently define the surface attachment of nanoparticles. Organosilane SAMs presenting various terminal chemistries can be prepared with a range of different substrates, such as silicon wafers, metal oxides, quartz, glass and mica.[102] Organosilane SAMs form robust, covalent bonds to surfaces, and are widely used as resist films for photolithography. Organosilane SAMs provide molecular platforms for further chemical modification steps to integrate designed moieties into well-defined surface patterns.[119-120] Combining particle lithography with molecular self-assembly is a practical approach for producing 2D arrays of organosilane nanostructures with ring-shaped geometries or nanosized holes within a surface film.[71-73] The organosilane nanostructures are an excellent foundation for building more complex nanostructures from the bottom-up, by successive *ex situ* steps of surface chemical reactions. Millions of nanopatterned sites can be produced with vapor deposition of organosilanes and

particle lithography to provide exquisite spatial selectivity, such as for deposition of uncoated gold nanoparticles.[72]

Methods for patterning core-shell nanoparticles will facilitate studies of size-dependent properties, by providing test platforms with discrete dimensions and surface arrangements of nanomaterials. Surface nanopatterns of nanoparticles offer advantages for high resolution studies with scanning probe microscopy (SPM),[162] and are an essential step for incorporating nanomaterials in sensors and miniaturized devices.[163] Strategies for patterning nanoparticles have been reported for preparing 1D wires[164] and 2D arrays[165] of coated nanoparticles using steps of solvent partitioning, self-assembly or evaporation. Ring structures of nanoparticles have been produced using evaporative particle lithography.[14, 75] To further control the dimensions and shapes of surface patterns of encapsulated nanoparticles, methods have been reported for attaching nanoparticles to patterns of thiol SAMs prepared on gold substrates using electron beam lithography[166] and microcontact printing.[163, 167] Methods based on microcontact printing produced multilayer patterns at size scales of 5-50 microns. Manipulation of single nanoparticles has been accomplished using atomic force microscopy (AFM)[163] and scanning tunneling microscopy.[163, 168] Exquisite precision has been achieved for patterning nanoparticles with SPM-based nanolithography,[169-171] however SPM-based methods generate nanopatterns individually by a slow serial procedure that is not easily scaled up for high throughput production of billions of nanostructures. A challenge is presented for developing high-throughput approaches for controlling the arrangement of nanoparticles at ever smaller dimensions. For studies of magnetic, optical or electronic properties of coated nanoparticles, additional steps which add chemical contaminants should be minimized or eliminated.

In this report, we introduce a protocol for patterning surface-active nanoparticles within uncovered areas of a silane-masked substrate. Modified gold nanoparticles were linked to

surfaces of silicon and glass by designing a linking group within the organic shell. Functionalized core-shell nanoparticles such as gold monolayer protected clusters consist of a gold core that is coated with a thiol organic monolayer, for applications such as biosensing and quantum devices.[159, 172-173] Using particle lithography, substrates with well-defined arrays of uncovered nanoholes were formed within a film of methyl-terminated silane SAM, and the patterned surfaces were then used as a resist to direct the attachment of coated gold nanoparticles within confined areas. Although we have previously patterned bare gold nanoparticles onto pre-formed backfilled nanopatterns of mercaptosilanes, the nature of surface attachment and chemical interactions become more complicated for coated nanoparticles. The chemical scheme of thiol-gold chemisorption (using bare nanoparticles) versus robust covalent linkages with silanation provides entirely different routes to mediate surface attachment than our previous publication.[72] Approaches with covalent linkages for directing nanoparticles to attach selectively to defined regions of the surface by steps of surface self-assembly and designed chemistry opens possibilities for chemical patterning of coated nanoparticles to generate functional nanostructures.

5.2 Experimental

5.2.1 Materials and Reagents

Boron-doped, double side polished Si(111) wafers (Virginia Semiconductor Inc., Fredericksburg, VA) and glass cover slides (Fisher Scientific, Pittsburgh, PA) were used as substrates. Concentrated sulfuric acid (98.0%), hydrogen peroxide (30%), $NaBH_4$ (99%), tetraoctylammonium bromide (98%), tetrachloroauric(III) acid and anhydrous toluene (99.8%) were purchased from Sigma Aldrich (St. Louis, MO). Monodisperse latex mesospheres (1 wt% solution) with a particle diameter of 200 nm were obtained from Duke Scientific (Palo Alto, CA). Octadecyltrichlorosilane (OTS) and 3-mercaptopropyltrimethoxysilane (MPTMS) were

purchased from Gelest (Morrisville, PA) and used without further purification. Anhydrous ethanol was obtained from Pharmco (Aaper, TX).

5.2.2 Substrate Preparation

Silicon substrates were cut into 1 × 1 cm^2 squares and cleaned by soaking in piranha solution (3:1 v/v ratio of concentrated sulfuric acid and 30% hydrogen peroxide) for 1 h. Piranha solution is corrosive and should be handled with caution. After cleaning, surfaces were rinsed with copious amounts of deionized water and dried in air (18 MΩ·cm, Millipore Milli-Q purification system, Boston, MA).

5.2.3 Synthesis of Organosilane Coated Nanoparticles

Gold nanoparticles with a diameter of 3-5 nm were chemically modified with MPTMS to produce nanoparticles with silanol terminal groups. The synthesis of coated nanoparticles followed a previously reported protocol.[43, 174-175] A solution of tetraoctylammonium bromide (35 mM in toluene, 10 mL) was added to 15 mM tetrachloroauric(III) acid in water (10 mL) as shown in Figure 5.1A. After mixing, $AuCl_4^-$ ions transferred to the top organic layer, as shown in Figure 5.1B when the toluene phase became orange-brown. Neat MPTMS (65 mg) was added to the toluene phase, and the resulting solution was stirred for 10 min at room temperature. With stirring, the orange-brown solution became colorless within 5 min, shown in Figure 5.1C. The colorless organic phase was isolated and transferred to a clean vial, and 10 mL of 150 mM $NaBH_4$ solution was slowly added to the organic phase to yield nanoparticles. The dark organic phase was further stirred at room temperature for 45 min to produce a dark color for the top layer containing MPTMS-coated gold nanoparticles, shown in Figure 5.1D.

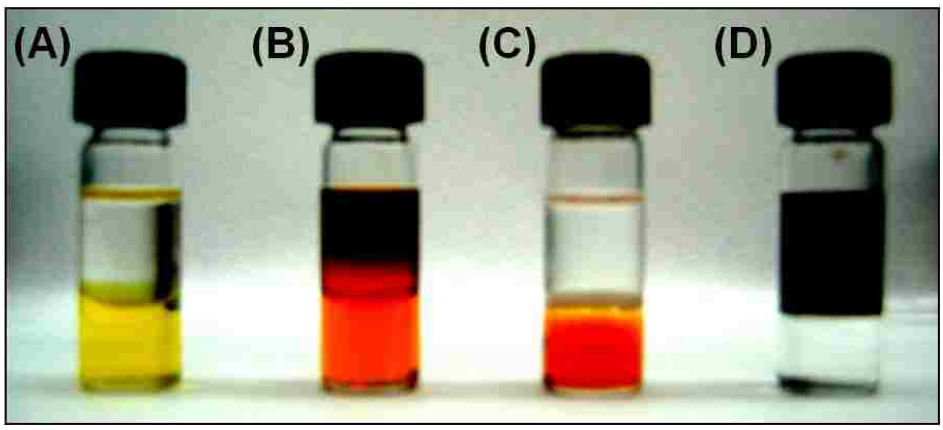

Figure 5.1 Color changes that evolve during synthesis of organosilane coated gold nanoparticles. (A) A solution of $HAuCl_4$ was added to toluene; (B) tetraoctylammonium bromide was added to the toluene solution and gold (III) cations were transferred to the organic phase; (C) after MPTMS was added to the solution the organic phase became colorless; (D) the organic phase was transferred to another vial, and a solution of sodium borohydride was added.

5.2.4 Selective Deposition of Nanoparticles on Organosilane Nanopatterns

Steps for the overall procedure for preparing nanopatterns of silane coated nanoparticles are shown in Figure 5.2. A surface masked with OTS nanopatterns was prepared using vapor deposition through mesoparticles, which left exposed sites for deposition of nanoparticles coated with MPTMS. Nanopatterns of OTS were prepared as previously described.[71] First, latex mesospheres were washed with deionized water to remove contaminants by three cycles of centrifuging (15 min $cycle^{-1}$) at 14000 rpm. The supernatant was discarded and the latex mesospheres were resuspended in deionized water with vortex mixing. A small drop (20 µL) of the latex suspension was deposited on a clean Si(111) substrate and dried for 20 min in ambient conditions (25°C, relative humidity ~50%). As water evaporates during the drying step, capillary forces induce the close-packing of spheres to spontaneously form a crystalline layer on the surface. A thin film of water persists throughout areas of the surface; however, residues of water become trapped near the base of the spheres to form a liquid meniscus ring. The sites where water residues are present define the locations for OTS to bind to the surface.

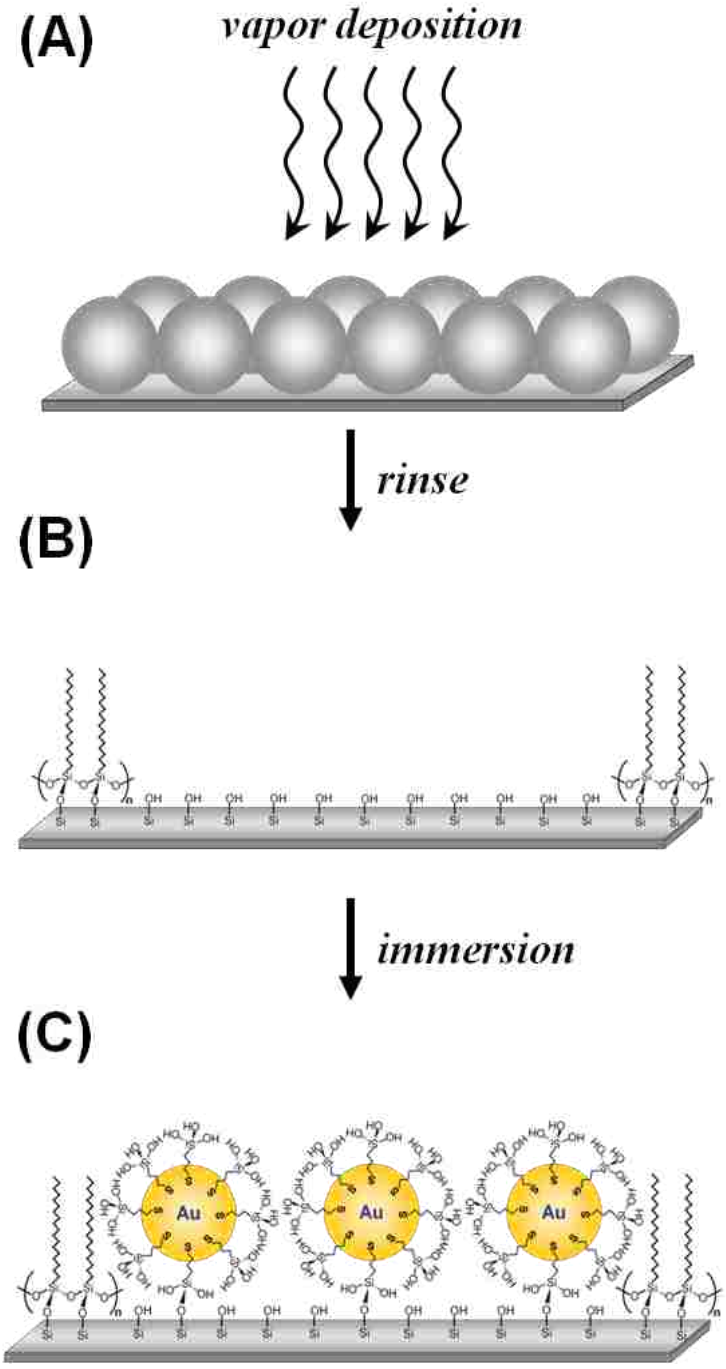

Figure 5.2 Procedure for nanopatterning silanol-coated gold nanoparticles. (A) Latex mesospheres provide an evaporative mask during vapor deposition of OTS; (B) latex masks are rinsed away to generate an array of OTS nanostructures; (C) nanoparticles deposit on areas of uncovered substrate after immersion in a solution of surface-active gold nanoparticles.

The dried film of latex furnishes an evaporative mask for patterning, and is placed in a sealed chamber containing a small volume of neat OTS (Figure 5.2A). The sample is heated in

an oven at 70°C for 8 h to generate vapors of OTS. During this step, organosilanes bind covalently at areas of the surface where water is present, forming a network of bridging Si-O linkages between adjacent molecules or the substrate. Areas of the surface where the latex particles make contact with the substrate remain protected from vapor deposition. The film of latex mesospheres is then removed by rinsing and sonicating the sample with deionized water and ethanol several times. After removal of the latex mask, nanopatterns of OTS molecules persist on the surface to reveal arrays of ring shaped nanostructures (Figure 5.2B). In the final step, surfaces patterned with OTS nanostructures are immersed for 12 h in a freshly-prepared solution of surface-active nanoparticles (Figure 5.2C). To remove loosely-bound nanoparticles, samples were then sonicated in ethanol three times for 15 min and dried in air.

5.2.5 Characterization of Nanopatterns

Scanning probe characterizations of samples were obtained in ambient conditions with a model 5500 scanning probe microscope (Agilent Technologies, Chandler, AZ). Pyramidal silicon probes with an average resonance frequency of 190 kHz and spring constants ranging from 20-95 N m^{-1} (Nanoscience Instruments, Inc., Phoenix, AZ) were used for imaging with tapping mode AFM. Oxide-sharpened silicon nitride cantilevers with force constants ranging from 0.1 to 0.5 N/m were used when imaging in contact mode (Veeco Probes, Santa Barbara, CA). Digital images were processed with Gwyddion open source software (version 2.9), which is supported by the Czech Metrology Institute.[140] Measurements of surface coverage were obtained with ImageTool (UTHSCSA, San Antonio, TX).[141] The percent surface coverage was estimated using 2D AFM images and averaging the surface coverage of representative images from different areas of multiple samples. Ultraviolet-visible (UV-Vis) spectra of the MPTMS-coated nanoparticles and nanopatterns were recorded with a Varian Cary 50 UV-Vis spectrophotometer (Palo Alto, CA).

5.3 Results and Discussion

Surface masks of organosilane nanopatterns produced using particle lithography provide exquisite spatial selectivity to define the adsorption of nanomaterials. For these studies, methyl-terminated nanopatterns were prepared by vapor deposition of OTS as a surface mask, to designate locations for subsequent adsorption of MPTMS-coated nanoparticles. Surface changes throughout the steps of particle lithography can be investigated with AFM. A representative example is shown in Figure 5.3 for arrays of OTS nanostructures formed on Si(111) substrates that were prepared with 200 nm diameter latex masks. The topmost frames are views of the OTS patterns after the latex mask was removed, and the lower panels show the changes after adsorption of nanoparticles. The ring geometries of the nanopatterns are exquisitely uniform at the nanoscale, shown by AFM topography and phase images in Figures 5.3A and 5.3B, respectively. The hexagonal packing of the latex mask is transferred to the surface arrangement of OTS ring structures, shown in the topography frame in Figure 5.3A. Phase images provide a sensitive map of the surface morphology, as well as reflecting differences in adhesion and softness of materials. The phase image (Figure 5.3B) and line height profile (Figure 5.3C) reveal an interesting irregularity of the surface coating of OTS. A dark black spot at the center of each ring in the phase image indicates that the tip-surface interaction is different than the areas between the rings. The dark contrast indicates a hard surface, and softer areas have brighter contrast. Analysis of the film thickness shows the deeper valleys occur at the centers of the circle patterns, pinpointing where latex spheres were displaced. These valleys furnish a baseline of the exposed bare substrate for thickness measurements. The film thickness of areas between the rings measures 1.3 ± 0.2 nm, which is shorter than the height of a densely-packed OTS monolayer. The thickness of a monolayer of OTS has been reported to measure within the range

of 2.26 and 2.76 nm, depending on sample preparation conditions.[130, 142-144] The thickness at the immediate areas of the rings measures 4.4 ± 0.4 nm, corresponding to a double layer.

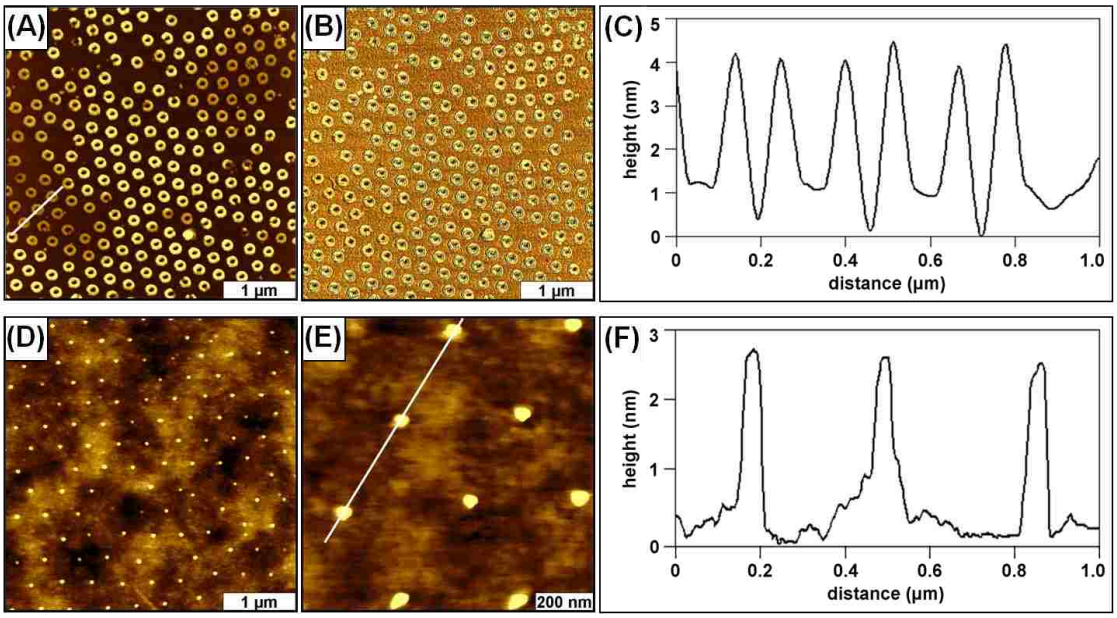

Figure 5.3 Nanopatterned surfaces before and after depositing nanoparticles. (A) Topography and (B) corresponding phase image of OTS nanostructures fabricated using particle lithography with 200 nm latex particles; (C) height profile for the line in **A**; (D) topography image of periodic arrays of nanoparticles produced by selective adsorption onto OTS nanopatterned surfaces; (E) zoom-in view of the nanostructures; (F) cursor profile for the line in **E**.

Height measurements of the OTS films suggest that more water was located near the base of latex spheres to produce dense packing and self-polymerization within the water meniscus sites. The coating of water residues is not entirely uniform throughout the surface, there are localized areas where water beads to form thicker residues. Water becomes trapped or pinned at meniscus sites near the latex spheres. A hydrolysis step is required for surface binding of OTS; therefore, the thickness of the OTS films provides a map of the locations of nanoscopic water residues. The areas between the taller OTS rings are less densely packed areas of OTS; however, the phase image shows fairly consistent surface coverage of the shorter phase. The deeper pores in the centers of the rings are areas of uncovered substrate, which provide sites for attachment of MPTMS-coated nanoparticles.

After the OTS nanopatterns were immersed in a solution of MPTMS-coated nanoparticles, the rings are no longer visible in the bottom panels of Figure 5.3. Instead, a periodic array of nanoparticle clusters is disclosed in the topography images (Figures 5.3D and 5.3E), and approximately 2.5% of the surface is covered with nanoparticles. There are 123 clusters of nanoparticles within the $4 \times 4\ \mu m^2$ frame (Figure 5.3D), which scales to a density of 8×10^8 nanostructures per cm^2. The round shape of the nanostructures conforms to the circular geometry of the pores confined within the OTS rings. The average height of the nanoparticle clusters measures 2.5 ± 0.4 nm above the surrounding OTS film, and the width of the nanostructures measures 54 ± 5 nm (FWHM ± standard deviation). A representative height profile is shown for three nanostructures in Figure 5.3F. Referencing the 1.3 nm thickness of the OTS film surrounding the OTS rings, the estimated height of the nanostructures is approximately 3.8 ± 0.4 nm, which matches the dimensions of the synthesized MPTMS-coated nanoparticles. The regular spacing between nanopatterns measures 333 ± 12 nm, according to the periodicity of the OTS ring nanopatterns. Multiple areas of the sample were analyzed, and these images are representative of views throughout the sample.

Films of OTS provide an effective resist layer for further steps of surface treatment because OTS presents a methyl group at the surface. For OTS to bind to surfaces, a trace amount of water is necessary to initiate surface hydrolysis. The amount of water that is present on the surface has been shown to greatly influence the quality of organosilane films.[112, 122, 131] Surface bound water initiates hydrolysis of organotrichlorosilanes to form organosilanols, which then either form siloxane linkages to the surface, form free silanol (Si-OH) groups, or undergo self-polymerization. Trichlorosilanes are highly reactive in the presence of water and can form multilayers through self-polymerization either on the surface or in solution, depending on experimental conditions.[147-148] The locations of water residues define the sites for OTS to bind to

the surface during vapor deposition, mediated by hydrolysis and condensation reactions. Meniscus areas contain trapped residues of water to form dense multilayer ring structures of OTS. Changes in ambient humidity and drying intervals for the latex particle masks correspondingly produce variations in the size of the nanoscale water meniscus. Recently, we reported that the size of the water meniscus can be correspondingly tuned by changing the diameter of the latex beads, such that particles with larger diameters produced taller nanostructures than those with smaller diameters with self-polymerization of organosilanes.[16] Essentially, the water meniscus trapped between latex particles and the substrate furnishes an exquisitely regular, nanoscopic reaction volume as a containment area for hydrosilation to occur. The small pores at the center of the OTS rings provide well-defined areas of bare substrate for further reaction steps. Samples prepared with 200 nm latex spheres generate nanoholes with diameters measuring 55 ± 2 nm, and the uncovered hole areas span about 6% of the surface. The diameters of the nanoholes produced with particle lithography combined with vapor deposition are smaller than the actual size of the latex spheres, since the area of surface contact between latex mesospheres and underlying substrate define the dimensions of the nanoholes. Adsorbates were not observed within the pores, indicating that latex spheres were effective surface masks for vapor deposition. With an immersion step, silane-functionalized nanoparticles attached selectively and uniformly within the pore areas surrounded by OTS (Figures 5.3D and 5.3E). These results showcase the exquisite spatial selectivity of chemical patterning with particle lithography.

The high throughput capabilities of particle lithography are demonstrated for a larger area, for a 10 x 10 μm^2 topography image (Figure 5.4). Arrays of nanoparticle structures span the entire surface and exhibit the long-range order of the latex mask, with periodicities extending over micron regions. A few defects (e.g., point defects and misaligned domains) are apparent,

which are inherited from mesospheres that did not fully close-pack. Missing patterns and line defects in mesosphere masks can be attributed to the polydispersity of the mesospheres as well as imperfections of the underlying substrate, which affect the packing arrangement of the latex particles during self-assembly.[152] A 2D fast Fourier transform (FFT) analysis, the reciprocal space of the topography frame, is displayed in the inset of Figure 5.4 as confirmation of the hexagonal arrangement and well-defined periodicity of the nanopatterns. The FFT analysis provides a quantitative picture of the long-range order and periodicity of the array of nanostructures.

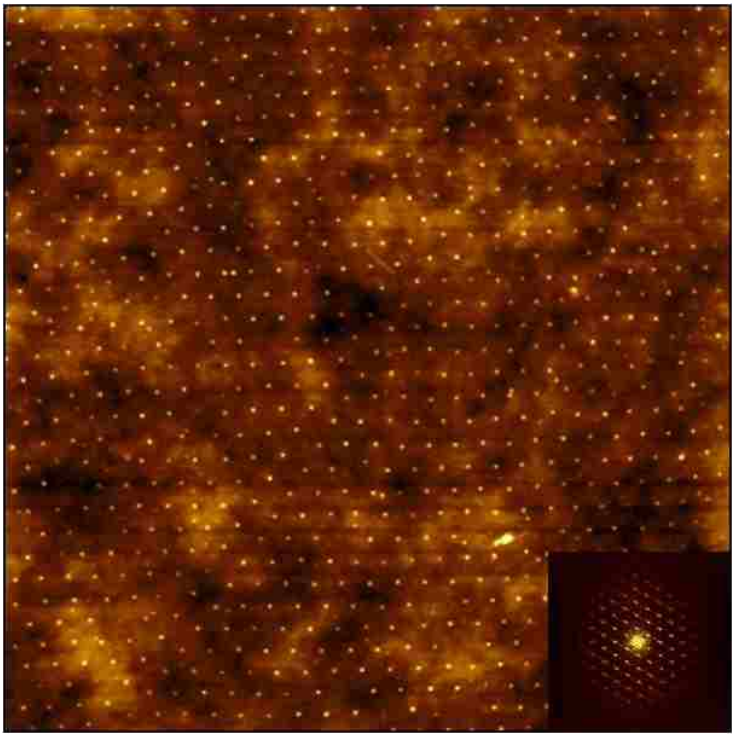

Figure 5.4 View of a broad area (10 x 10 μm^2) of nanostructures fabricated with 200 nm latex masks; the inset shows an FFT spectrum generated from the topograph.

To investigate the optical properties of nanopatterned nanoparticles, samples were prepared on glass substrates and characterized with UV-Vis spectrophotometry (Figure 5.5). The conditions for preparing OTS patterns on Si(111) also works well for glass or mica(0001) substrates.[71-72] As a comparison, UV-Vis spectra were acquired for nanoparticles in solution, as

well as for OTS nanopatterns on glass substrates. For nanoparticles in solution, a prominent absorption peak is observed around 335 nm (green line). However, no peaks were observed in the 300-600 nm UV-Vis region for OTS nanopatterns on glass substrates (blue line), which was prepared as a control sample. When nanoparticles were selectively deposited on OTS nanopatterns formed on glass substrates, two peaks appear at 415 and 465 nm in the UV-Vis spectra (red line). The red-shift observed for gold nanostructures results from changes in interparticle distance as the gold nanoparticles assemble onto spatially confined areas of the surface patterns.

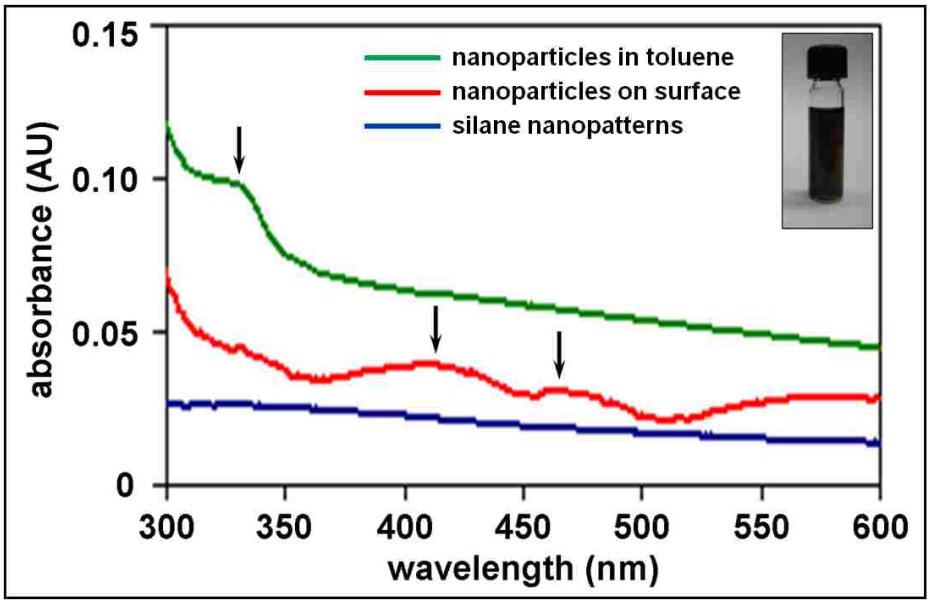

Figure 5.5 Comparison of UV-Vis spectra for synthesized silanol-coated gold nanoparticles and nanopatterned surfaces; the inset is a photograph of functionalized gold nanoparticles (dark brown) in solution.

UV-visible spectroscopy has been widely used for the characterization of metal nanoparticles to investigate the size-dependent changes for electronic structures and relative optical properties. Larger gold colloids with diameters more than 2 nm display the well-known surface plasmon band in the visible region at ca. 520 nm.[176-177] The intensity of this absorption band decreases with a smaller gold cluster size in accordance with theory.[176] For gold

nanoparticles with diameters less than 2 nm, the surface plasmon resonance disappears completely, leaving a smooth spectrum with absorbance increasing exponentially from the visible to the ultraviolet region.[175, 178-179] With a further decrease in size, the emergence of discrete peaks in the UV-Vis spectra are observed.[175, 178]

The long term stability of the nanopatterns was evaluated by examining a sample after several years of storage in ambient conditions. Although it is generally known that covalent linkages with organosilanes are robust, we examined one of our earlier samples after 39 months of storage in a closed plastic container. A sample prepared with 200 nm latex masks was characterized with tapping mode AFM (Figure 5.6) for comparison with a freshly-prepared sample. A representative view of an "aged" sample is shown in Figure 5.6A and 5.6B, demonstrating that the nanostructures have persisted and are clearly apparent in the topography and phase images, respectively. The phase image discloses the location of very small nanostructures that are hidden in the topography frame. After careful AFM studies, we were unable to resolve discrete shapes of individual nanoparticles for the aged sample, whereas the zoom views for the sample of Figure 5.3 show morphologies of clusters of nanoparticles. This may be caused by close adhesion between adjacent nanoparticles over time. Individual cursor measurements of each of the nanostructures in Figure 5.6A show the overall heights of the nanostructures range from 2.5 to 7.0 nm, with a mean value of 4.3 nm. The histogram and scatter plot of Figures 5.6C and 5.6D were measured directly from the single frame shown in Figure 5.6A, with 200 data points. The plot in Figure 5.6D shows the correlation between the surface area and measured height of individual nanostructures. From height measurements of nanostructures, a general trend is evident that nanostructures with larger lateral dimensions have taller heights. At the nanoscale, the sizes of the uncovered pores within the OTS film are not

perfectly uniform in dimension. Surface sites with smaller areas have fewer nanoparticles attached within the nanostructures.

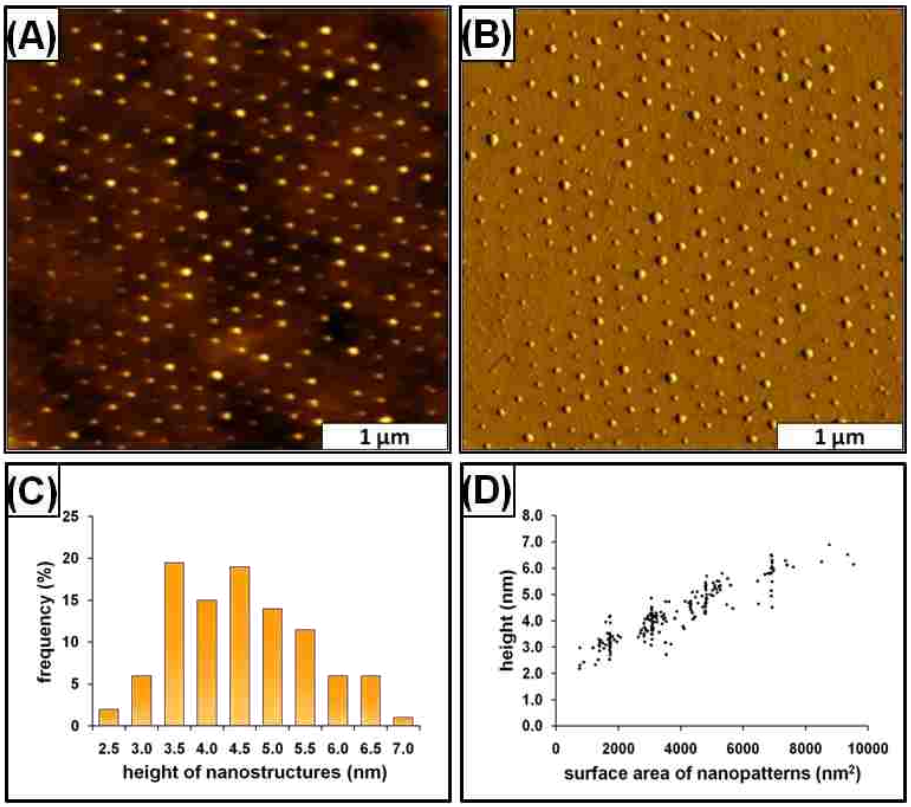

Figure 5.6 Nanopatterns of silanol-terminated gold nanoparticles persist on a Si(111) substrate after long term storage in ambient conditions. The sample was prepared using 200 nm latex mesospheres. (A) Topography and (B) corresponding phase image (3.5 x 3.5 μm^2); (C) height histogram for nanostructures; (D) correlation of height with measured surface area.

5.4 Conclusions

Designed surface structures of OTS prepared with particle lithography can be used for the precise positioning of surface-active nanoparticles to produce billions of uniformly shaped nanopatterns with designed surface coverage and interpattern spacing. Overall, the geometry, number density and surface coverage of the nanostructures are exquisitely reproducible at the nanoscale and are mainly determined according to the diameters of the latex masks. Organosilane nanostructures prepared by particle lithography furnish well-defined sites for spatially directing surface reactions, such as for deposition of nanomaterials with well-defined

arrangements. Particle lithography with organosilanes requires only a few basic chemistry steps, yet provides generic capabilities for high throughput lithography of exquisitely small and regular nanostructures. Our approach for nanopatterning has achieved exquisite control of the placement of single layers of coated nanoparticles in well-defined nanoscale arrangements with simple chemical steps. The simplicity of particle lithography is a major advantage for producing surface test platforms for scanning probe studies, without the need for expensive instrumentation or additional surface contaminants. This approach can be applied for preparing well-defined surface arrangements of other core-shell nanomaterials with more complex shell chemistries.

CHAPTER 6. HYBRID APPROACH FOR NANOFABRICATION: PARTICLE LITHOGRAPHY COMBINED WITH CONTACT PRINTING OF ORGANOSILANES

6.1 Introduction

Microcontact printing of organic thin films was introduced by George Whitesides in 1994, and has since become an essential commercial tool for patterning microcircuitry, sensor platforms, and surface-based microdevices.[180-182] Although the feasibility of extending microprinting capabilities to the nanoscale has been demonstrated with microcontact printing, nanoscale dimensions (<100 nm) are difficult to achieve because of the limitation of manufacturing masks or molds with very small dimensions. Masters for preparing polydimethylsiloxane (PDMS) stamps are manufactured with photolithography. Monodisperse, size-sorted latex beads can provide exquisitely regular dimensions for surface masks, to enable nanolithography with molecular-level dimensions. Particle lithography provides an alternative approach for producing regular arrays of molecular nanostructures with high throughput. Particle lithography is an economical approach for generating nanostructures with a few basic steps of self-assembly using bench chemistry (i.e. centrifugation, sonication, mixing, drying). In this report, we describe a hybrid approach for achieving nanoscale patterning of organosilanes by combining contact printing with latex particle lithography. This 'hybrid' strategy provides a tool for chemical patterning of two components for designing nanostructures of organosilane self-assembled monolayers (SAMs).

Particle lithography, also referred to as colloidal lithography,[79] natural lithography,[78] evaporative lithography,[14] or nanosphere lithography,[80] is a general approach for high-throughput nanopatterning and is based on using a mask or template of close-packed spheres. Monodisperse latex or colloidal silica beads spontaneously assemble into close-packed crystals when solutions of spheres are dried on a flat substrate. Methods of particle lithography have been reported for

preparing nanopatterns of polymers,[61] metals,[62-63] SAMs,[68-70] nanoparticles,[14, 75] and proteins.[15, 76-77] Approaches for particle lithography most often are based on thermal or e-beam evaporation of heated metals through shadow-masks of spheres.[78, 103] A strategy with vapor deposition of alkanethiols was reported by McLellan et al.[96] and for certain organosilanes by Li et al.[16, 71-72] The vapor deposition of organosilanes is limited to certain small molecules which can be heated to produce a vapor, and is not a general approach for all molecular systems. . A potential problem with particle lithography can occur for patterning SAMs using immersion steps because the mesospheres rapidly detach from the substrate when the masks are submerged in solutions of liquids. Also, polystyrene latex dissolves in certain solvents (e.g. chloroform, acetone, toluene). On the other hand, this disadvantage provides a convenient route for clean removal of the mesoparticle masks.

The problem of applying a thin film of organic molecules to a substrate through a mask of mesospheres can be solved with a hybrid strategy: using contact printing with PDMS stamps. A method for printing *n*-alkanethiols on gold substrates, referred to as edge-spreading lithography was previously reported by McLellan et al.[70] The transfer of thiol inks relies on an adsorption mechanism of sulfur-gold affinity and surface chemisorption taking place in ambient air. However, the applicability of PDMS stamping for patterning organosilane SAMs with particle masks has not yet been advanced. A considerable advantage of using organosilane rather than thiol SAMs is the capability for covalent binding of silane films to different types of substrate materials, such as silicon oxide, aluminum oxide, germanium oxide, quartz, glass, gold and mica.[102] The nature of surface attachment for organosilanes requires a hydrolysis step; trace amounts of water are necessary for silanation reactions. In this study, we test the applicability of patterning organosilanes using a hybrid lithography approach, combining contact printing of organosilane SAMs with PDMS stamps through surface masks prepared by particle lithography.

Molecular level investigations reveal the feasibility of a hybrid lithography strategy, and demonstrate that the geometries and quality of organosilane nanostructures inherently depend on processes of surface wetting.

6.2 Approach for Hybrid Nanolithography

The fabrication steps are outlined in Figure 6.1. First, boron-doped, double-side polished Si(111) substrates (Virginia Semiconductor Inc., Fredericksburg, VA) were cleaned by soaking in piranha solution for 1 h (piranha solution is a mixture of concentrated sulfuric acid and 30% hydrogen peroxide, 3:1 v/v ratio, which is highly corrosive and should be handled with caution). Next, silicon substrates were rinsed with copious amounts of deionized water (18 MΩ·cm, Millipore Milli-Q plus system, Boston, MA) and dried in ambient conditions (25 ºC, relative humidity ~ 55%). Monodisperse latex mesospheres (Thermo Scientific, Waltham, MA) were washed with deionized water rinses by centrifuging at 14000 rpm for 15 min to form a pellet and resuspending the latex pellet in deionized water (three cycles). A 20 µL drop of the latex particles suspension was deposited on the freshly cleaned substrate and dried in air for 2 h. During the drying step, capillary forces of evaporating water cause the monodisperse mesospheres of latex to form close-packed layers on the substrate (Figure 6.1A), which provides a mask for patterning. A 2 x 2 cm^2 block of PDMS (Sylgard 184, Dow Corning) was used for transferring octadecyltrichlorosilane (OTS) (Gelest, Morrisville, PA) molecules to the surface of the latex film. A 30 µL volume of a 30% v/v solution of OTS in bicyclohexyl was deposited and spread evenly over the PDMS block, then quickly dried in a stream of ultrahigh purity argon. The PDMS block coated with OTS was placed on top of the latex masked substrate (Figure 6.1B). As the OTS solution was transferred from the PDMS block through the latex mask by permeation, the surface areas directly underneath the particles are protected from silane adsorption. After 1 h of physical contact, the PDMS block was lifted off and the sample was

rinsed with copious amounts of deionized water. In the final step, the mask of latex particles was cleanly removed by sonicating and rinsing with ethanol (Pharmco, Aaper, Tx) and deionized water. After removal of the mask, periodic arrays of Si/SiO_2 nanopores within a nanostructured film of OTS were generated on the surface (Figure 6.1C).

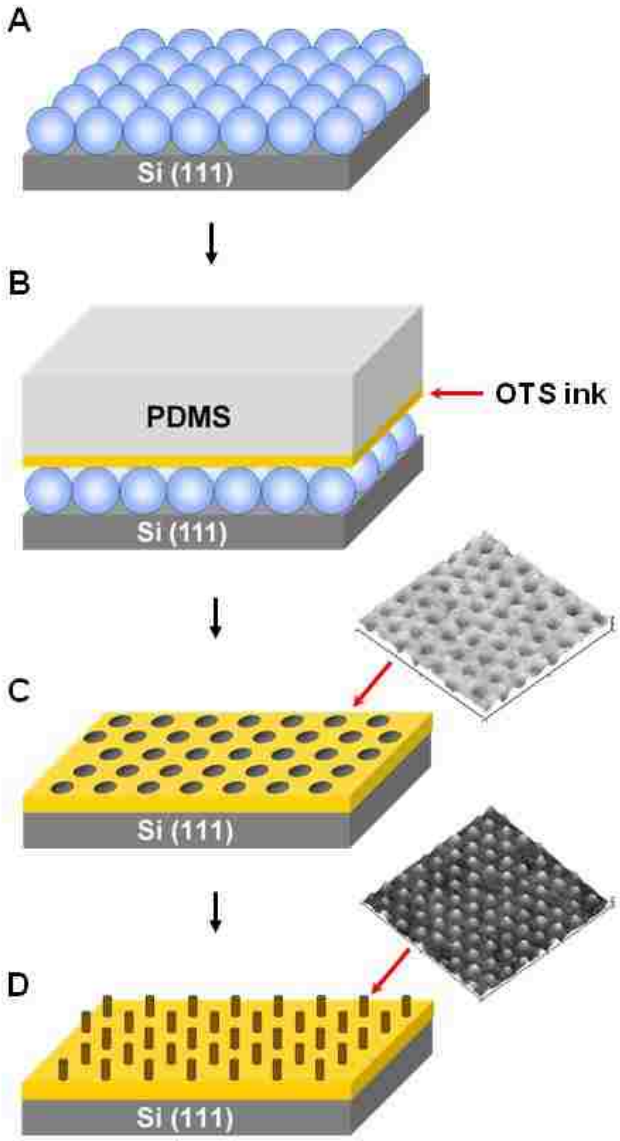

Figure 6.1 Fabrication steps for particle lithography combined with contact printing of organosilanes. (A) A dried film of latex mesospheres on a Si(111) substrate provides a mask for patterning. (B) A PDMS block coated with OTS was placed in contact with the masked surface. (C) The PDMS block was removed after 1 h, and the latex mask was rinsed away. A thin nanostructured film of OTS with circular areas of bare substrate is printed on the substrate. (D) Pillars of 6-AAPTMS were produced by immersing the sample into a solution containing a second organosilane.

The uncovered areas of the substrate were backfilled with a second organosilane by immersing the sample for 6 h in a 1.6 % (v/v) solution of N-(6-aminohexyl)-3-aminopropyl-trimethoxysilane (6-AAPTMS) (Gelest, Morrisville, PA) in anhydrous toluene (Sigma Aldrich, St. Louis, MO). Samples were then rinsed and sonicated with ethanol and water to produce two-component nanopatterns with discrete columns of 6-AAPTMS multilayers surrounded by a film of OTS (Figure 6.1D).

Samples were characterized using either contact or tapping-mode atomic force microscopy (AFM) throughout different steps of lithography (Agilent model 5420 and 5500 scanning probe microscopes, Agilent Technologies, Chandler, AZ). Oxide-sharpened silicon nitride cantilevers with force constants ranging from 0.1 to 0.5 N/m were used for contact mode imaging (Veeco Probes, Santa Barbara, CA). Silicon probes with a spring constant of 48 N/m and a resonant frequency of 190 kHz were used for tapping-mode AFM studies (Vistaprobes, Phoenix, AZ). Digital images were processed with Gwyddion open source software (version 2.9), which is supported by the Czech Metrology Institute.[140] Analysis of surface coverage was accomplished by manual thresholding of black and white pixel scales, using ImageTool software (UTHSCSA, San Antonio, TX).[141]

6.3 Results and Discussion

Films of nanostructured OTS produced by particle lithography with contact printing are shown in Figure 6.2A and 6.2B. Periodic surface patterns of bare substrate areas with circular geometries that were produced within an OTS film using latex diameters of 200 and 300 nm are shown in the AFM images of Figures 6.2A and 6.2B, respectively. The nanopatterns exhibit exquisitely uniform and regular morphologies and geometries. The topographs in Figures 6.2A and 6.2B do not show any OTS adsorbed at the center areas of the nanoholes where the latex spheres were previously in contact with the surface. The nanoholes correspond to the

arrangement and periodicity of the mask. Lateral force images show changes in frictional forces for tip-surface adhesive interactions. Differences in surface chemistry between OTS nanostructures and uncovered silicon substrates are apparent in the lateral force images shown in Figures 6.2A and 6.2B and furnish a chemical map of the regions of substrate and OTS. The uniformity in color contrast of the OTS film surrounding the nanoholes indicates a homogenous surface composition. The 2 x 2 μm^2 zoom-in topography views and simultaneously acquired lateral force images of the patterned surfaces in Figure 6.2A and 6.2B reveal that the hexagonal pattern of the latex mask is preserved after fabrication. The diameters of the holes measured 108 ± 10 nm for samples prepared with 200 nm latex and 168 ± 10 nm for samples prepared from 300 nm latex. The sizes of the bare areas results from conformal contact of the deformable latex spheres with the substrate. Within the 2 × 2 μm^2 topography frames in Figures 6.2A and 6.2B, there are 61 and 27 nanoholes, respectively, which would correspondingly scale to a surface density of 1.5 x 10^9 and 6.8 x 10^8 holes per cm^2. To estimate the periodicity of the nanopatterns, the average distance between the centers of the holes was measured for at least 100 nanoholes from several different areas of the surface. The lateral periodicity for nanopatterns prepared with 200 and 300 nm latex mesospheres measured 222 $\pm$ 8 and 329 $\pm$ 11 nm, respectively, in close agreement with the latex diameter chosen for fabrication. To evaluate the height of the OTS nanostructures surrounding the nanoholes, a height profile was extracted from zoom-in topography images for each sample. Referencing the areas of uncovered silicon substrate as a baseline, the thickness of the OTS films for the sample prepared with 200 nm latex diameter measured 0.6 $\pm$ 0.1 nm, and 0.5 $\pm$ 0.1 nm for 300 nm latex masks. The thickness of the OTS film was consistent throughout areas of the surface surrounding the circular patterns of uncovered substrate. A densely packed film of OTS with saturation coverage has been reported to measure

within the range of 2.26 and 2.76 nm in thickness.[130, 142-144] Therefore, the nanostructured OTS film produced using these conditions in ambient air did not achieve dense-packing.

A control sample was prepared by following the procedure for particle lithography combined with contact printing, without using OTS to coat the PDMS block. In the absence of OTS, no patterns were detected in the AFM topography and lateral force images shown in Figure 6.2C. The cursor profile in Figure 6.2C shows a relatively flat surface, and reveals the morphology of the Si(111) substrate. The AFM images for the control sample verify that neither PDMS nor latex was transferred to the surface during the steps of contact printing.

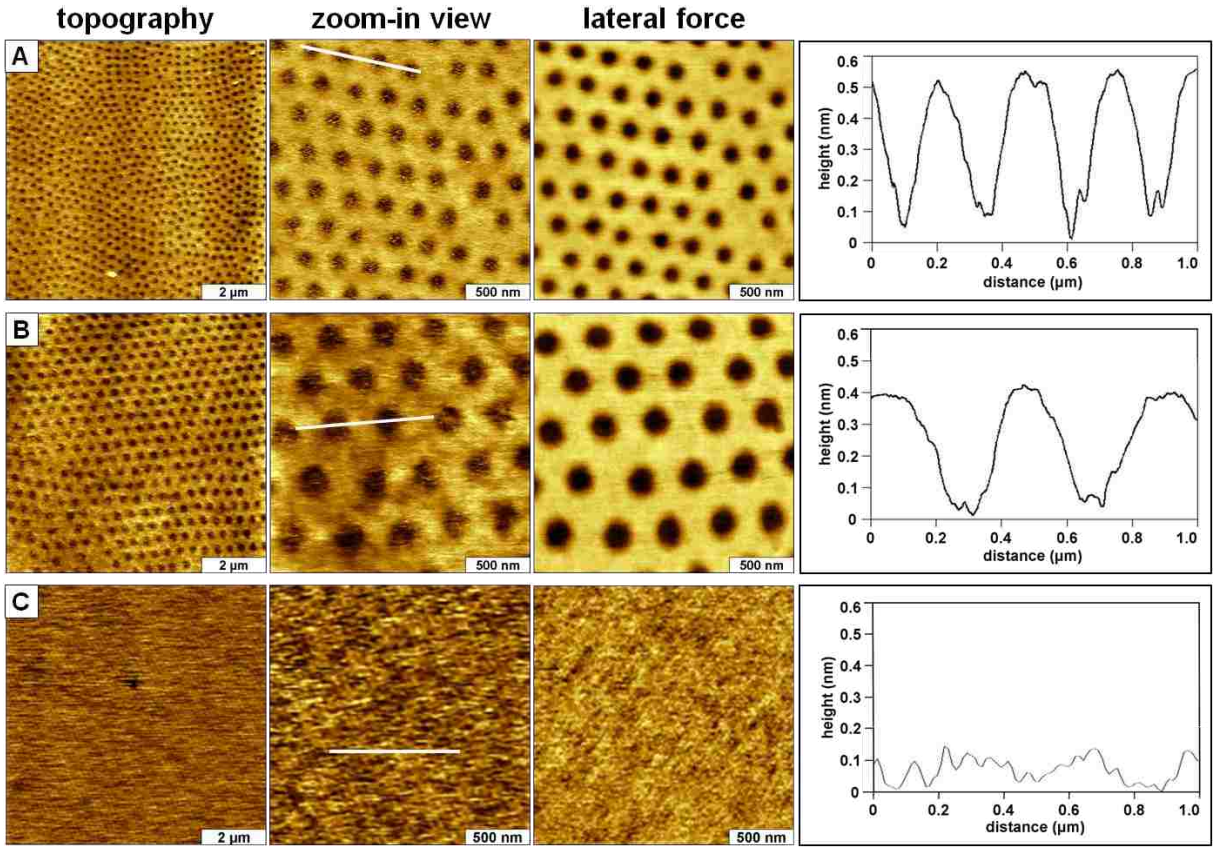

Figure 6.2 Samples prepared by particle lithography combined with contact printing characterized with contact mode AFM. Topography views, lateral force images, and height profiles of (A) arrays of Si/SiO_2 nanoholes within an OTS film prepared with 200 nm latex; (B) film of OTS prepared with 300 nm latex; (C) control sample prepared without OTS.

A trace amount of water is necessary to initiate hydrolysis of OTS for OTS to bind to substrates. When heat is applied to the surface mask, water residues can collect and become trapped near the bottom of latex spheres to form a meniscus.[16] However, with contact printing, the latex masks are dried under ambient conditions and residual water persists throughout areas of the surface surrounding the latex mask. The latex films were dried for no more than 2 h before the contact printing step to ensure that a thin film of water is distributed throughout areas of the surface. We have observed that the distribution of water is more homogeneous for hydrophilic surfaces such as mica or acid-cleaned silicon substrates. During contact printing, OTS molecules covalently bind to unmasked areas of the surface where water is present. The mask of latex particles prevents OTS from binding onto areas of the surface directly beneath the mesospheres. The results presented in Figures 6.2A and 6.2B show that OTS deposits at the interstitial areas of the surface between latex mesospheres during contact printing.

To evaluate the nanoscale reproducibility of particle lithography with contact printing for controlling pattern geometry, samples were prepared using different diameters of latex. The changes in surface coverage of OTS were compared for different sizes of mesoparticles (Figure 6.3). The amount of surface covered by OTS scales according to the size of the latex spheres; smaller spheres cover wider areas of the surface ranging from 79 to 95%.

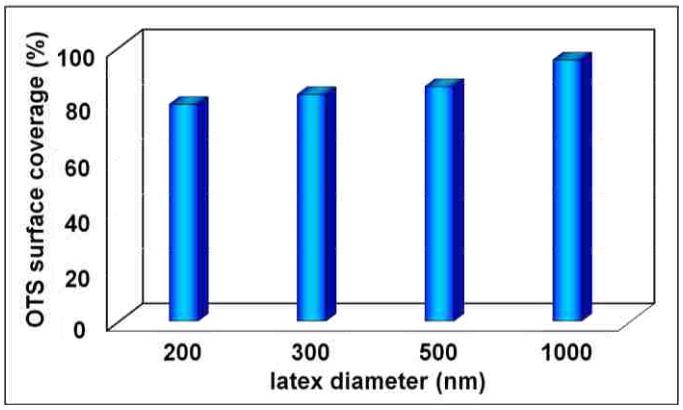

Figure 6.3 Corresponding changes in surface coverage of OTS for different latex diameters.

The density of nanoholes was plotted as a function of latex diameter, as shown in Figure 6.4. The values were estimated by counting the number of holes within AFM frames, and projecting an estimate of the surface density for larger areas. As the size of the latex mesospheres increases, the number of nanoholes decreases exponentially. The overall surface density scales from 1.3 billion holes per cm^2 for a 200 nm latex mask to 0.1 billion holes per cm^2 for patterns prepared with a latex diameter of 1 μm.

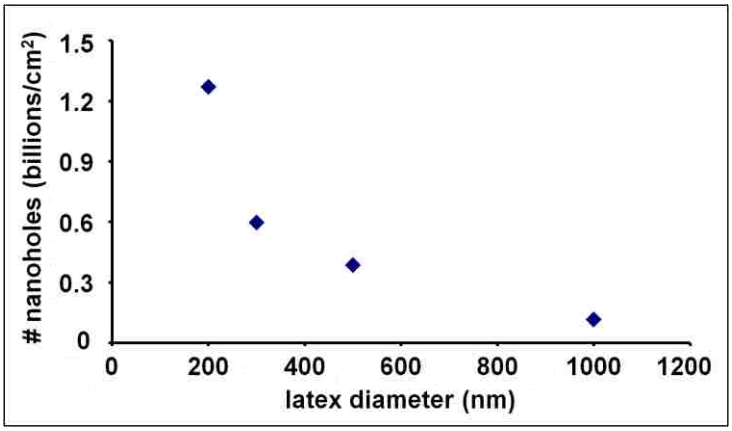

Figure 6.4 Changes in the surface density of nanoholes produced using different diameters of latex.

A further step of backfilling the nanoholes was accomplished by immersion of samples in a second organosilane solution. Methyl-terminated OTS should provide an effective resist for further chemical steps to achieve patterning of another component. However, with submonolayer surface coverage of OTS, the intercalation of molecular materials could occur. The backfilling experiment was used to test the effectiveness of the thin OTS resist for preventing non-specific binding of molecules to OTS-protected areas of the substrate. Nanopatterned surfaces prepared by particle lithography with contact printing were further chemically modified by backfilling the holes of uncovered substrate with 6-AAPTMS, an amine-terminated silane, as shown in Figure 6.5. The nanostructures viewed in the 10 × 10 μm^2 topograph (Figure 6.5A) reveal that the 6-AAPTMS molecules deposited selectively on bare areas of the substrate within the nanoholes

and did not cross-contaminate the surrounding areas of OTS. Differences in surface chemistry between OTS and 6-AAPTMS nanostructures are clearly distinguished in the phase image (Figure 6.5B), shown by differences in contrast; the 6-AAPTMS areas are the bright spots. Within the wide-area frames of Figures 6.5A and 6.5B, there are 910 nanostructures of 6-AAPTMS. A few defects are revealed, which are caused by lines that form between latex spheres which shrink in size when dried. A perfect array would pack an estimated 1000 nanostructures within the 10 × 10 μm^2 area, thus the density of defects is approximately 9 %. The reciprocal space of the topography frame is shown in Figure 6.5C with a 2D fast Fourier transform (FFT) analysis and confirms the well-defined periodicity of the nanopattern array. The FFT analysis provides a quantitative picture of the long-range order of the array of 6-AAPTMS nanostructures. A 3D topograph of the surface patterns for a 4 x 4 μm^2 is displayed in Figure 6.5D.

A close-up view of nine dot patterns of 6-AAPTMS is shown for a 1 × 1 μm^2 topography frame in Figure 6.5E. The zoom-in view of the surface topography reveals the highly regular geometry of the nanodots. The nanodots do not touch neighboring patterns; there is no overlap between adjacent nanostructures. A height profile of three nanodots indicates a height of 1.7 ± 0.2 nm. Considering the thickness of the surrounding OTS film, which measured an average height of 0.5 ± 0.1 nm, the total thickness of the 6-AAPTMS measures approximately 2.2 ± 0.2 nm, which is taller than the theoretical length of 1.48 nm for a single molecule of 6-AAPTMS.[123] The height indicates that interchain crosslinking takes place between 6-AAPTMS molecules of the nanostructures to form a branched, self-polymerized structure. The amino group of 6-AAPTMS can form a hydrogen or ionic bond with the methoxysilane group of either another aminosilane molecule or its hydrolyzed form.[123] Also, the amino group can self-catalyze the hydrolysis step to produce multilayers.[149]

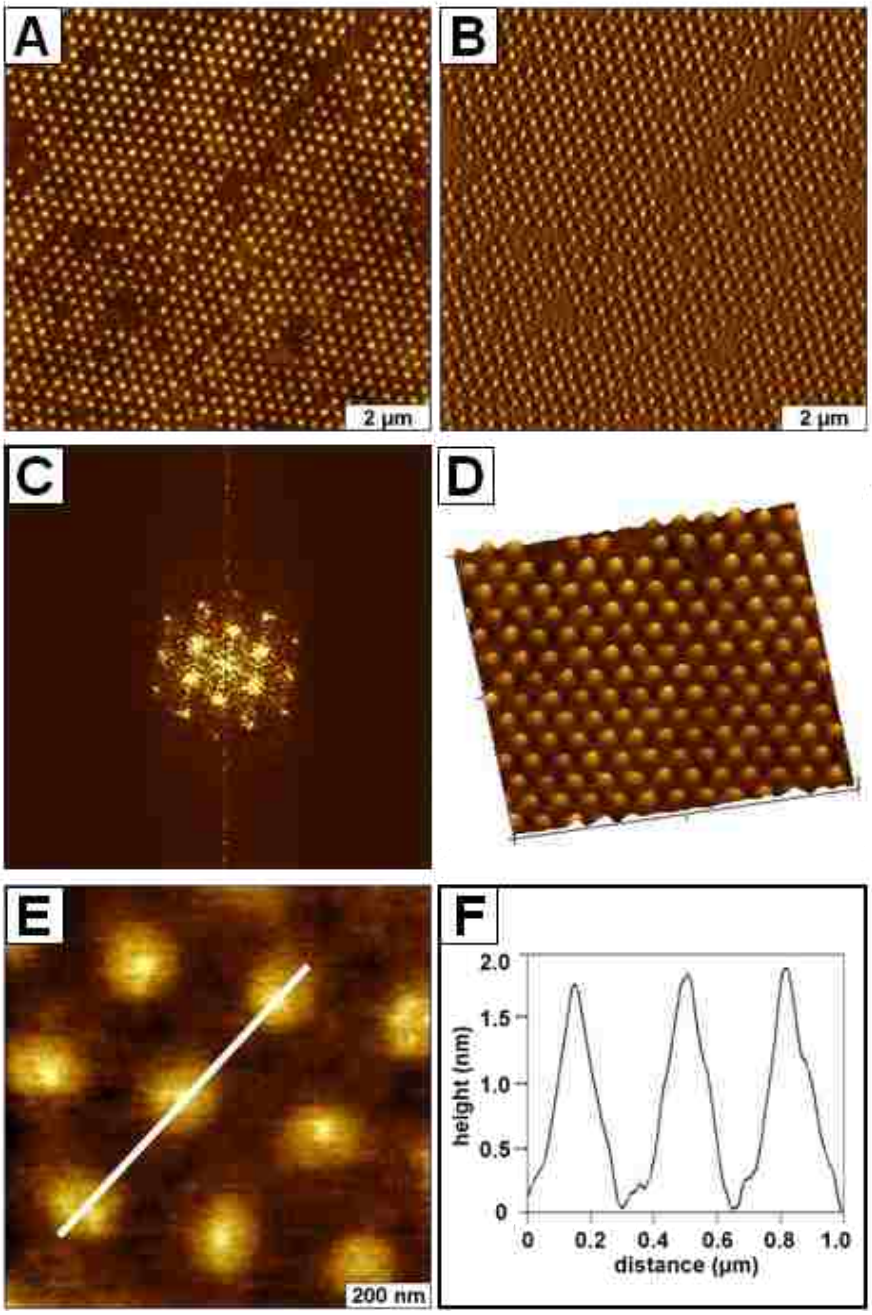

Figure 6.5 Periodic arrays of nanodots produced after backfilling with 6-AAPTMS. Nanoholes within films of OTS were prepared with particle lithography and contact printing using 300 nm latex. (A) Topograph of a surface nanopatterned with 6-AAPTMS and OTS; (B) phase image simultaneously acquired with **A**; (C) FFT spectrum generated from the topograph in **A**; (D) 3D view for a 4 x 4 μm^2 area; (E) zoom-in topographic view; (D) height profile for the cursor line in **C**.

Note that the cursor plot of Figure 6.5F shows the profile of a highly regular angular shape for the 6-AAPTMS nanostructures. This is not the true shape of the surface features; the

nanodots most likely have a columnar structure which is far smaller than the apex of the AFM probe. The line profile actually reveals the shape of the AFM probe rather than the shape of the exquisitely tiny molecular structures. The full width half maximum estimate of the width of the nanostructures measures 151 $\pm$ 11 nm. This width is slightly smaller than expected, since the diameter of the nanoholes measured 168 nm. Experiments are in progress to evaluate changes in dimension observed for silane nanostructures immersed in different solvents, which can account for the size discrepancies.

6.4 Conclusion

Exquisitely regular control of surface chemistry at the molecular level can be achieved with hybrid nanolithography, by combining particle lithography with contact printing. Contact printing enables transfer of a thin layer of OTS by physical contact of a PDMS stamp with a surface mask of latex spheres. The mask can be removed by rinsing, to generate billions of uniformly shaped nanopatterns that are accessible for further steps of chemical patterning. The methyl headgroup of OTS provides an effective resist. The surface coverage of OTS, as well as the density and periodicity of the nanopatterns can be selected by the latex diameter. Beyond introducing a versatile and generic toolkit for nanolithography, these experiments demonstrate molecular views of the products of surface self-assembly reactions. The nanoholes provide a surface template for scanning probe studies of chemical reactions within confined nanoscopic areas. The capabilities for controlling the spatial arrangement of two-component SAMs using particle lithography combined with contact printing offers a starting point for further molecular level studies with multifunctional surfaces.

CHAPTER 7. ORGANIC PHOTOVOLTAIC SOLAR CELLS DESIGNED USING NANOPATTERNS OF ORGANOSILANES AND POLYTHIOPHENES

7.1 Introduction

Organic photovoltaic (OPV) devices offer a promising alternative to traditional silicon based solar cells since they can be produced at low-cost and high speeds through roll-to-roll printing and coating techniques.[183-184] Also, the fabrication process does not require high temperatures or expensive raw materials. Solar cells based on OPVs can be applied to flexible and plastic substrates and are, therefore, lightweight materials. Higher power efficiencies are a key challenge for commercialization of OPV devices. The efficiency is defined as the ratio of electrical energy output to energy input, and is a term used to describe the overall performance of the device. The highest efficiency reported to date is 7.4% for OPV prototype solar cells.[185] For OPVs to be considered for commercial widespread use, an efficiency of at least fifteen percent will be required.[186] The nanoscale morphology and molecular structure of the donor and acceptor materials in the active layer greatly affects the charge separation and charge transport processes that occur after light absorption, thus affecting the efficiency of OPV devices.[187-188]

Although current state-of-the-art bulk heterojunction OPV devices based on semiconducting polymers are moving toward this target, mostly through new materials design, reaching this efficiency requires a new paradigm for precisely controlling the nanoscale organization and molecular structure of the polymers during device fabrication. Such control will help to address two major bottlenecks – increasing the efficiency of exciton dissociation and enhancement of carrier mobility towards electrodes. The efficiency of OPV devices intrinsically depends on the nanoscale morphology. We are working to develop an alternative, "bottom-up" approach to achieve the finest possible control over the organization and morphology of OPV materials at the molecular level. We use surface-initiated *in situ* polymerization with

nanostructured surfaces to precisely control vertical and lateral molecular arrangements of donor/acceptor molecules in the organization of semiconducting polymer thin films. These films will then be converted to functional, complete solar cells. To achieve efficient *in situ* polymerization, simple and effective reactions will be employed, such as metal-catalyzed "living" polymerization. To address the challenge for improving the device efficiency of OPVs, new fabrication methods need to be developed for controlling the molecular organization and orientation of materials with nanoscale precision.

Organosilane nanopatterned surfaces prepared by particle lithography offer a convenient route for spatially confining the orientation of conducting polymers during surface reactions. In this chapter, methyl-terminated organosilane thin films with periodically arranged holes of uncovered substrate were fabricated using particle lithography combined with contact printing as a strategy for directing the 2-D spatial organization of polythiophene nanostructures. The nanopatterned surface was used to control the lateral and hierarchical structure of polythiophene during surface initiated living polymerization. With particle lithography followed by *in situ* living polymerization of surface immobilized initiator, billions of periodically arranged polythiophene nanopillars were produced on surfaces of Si(111) substrates with defined geometry and interpattern spacing. Work is in progress to develop wafer-scale prototype solar cells with discrete, well-defined nanostructures of polythiophene films using particle lithography-based methods.

7.2 Experimental Approach

7.2.1 Preparation of Polythiophene Nanopatterns

Arrays of polythiophene nanopatterns were prepared using particle lithography combined with contact printing. Pieces of boron-doped polished silicon wafers of Si(111) (Virginia Semiconductor Inc., Fredericksburg, VA) or quartz slides (Chemglass) were cut into 1×1 cm^2

squares and soaked in piranha solution for 1 h. Piranha solution is a mixture of concentrated sulfuric acid and 30% hydrogen peroxide (3:1 v/v ratio), which is highly corrosive and should be handled with caution. Next, silicon substrates were rinsed copiously with deionized water (18 MΩ·cm, Millipore Milli-Q plus system, Boston, MA) and dried in ambient air. Monodisperse latex mesospheres (Thermo Scientific, Waltham, MA) were washed with deionized water to remove surfactants by centrifugation. A 300 µL volume of aqueous latex suspension (1 wt%) was centrifuged at 14000 rpm for 15 min, and the supernatant was decanted. The pellet of latex was resuspended in 300 µL deionized water. A 30 µL drop of the latex suspension was deposited on the freshly cleaned substrate and dried in air for 2 h. As water evaporated during the drying step, the monodisperse latex spheres form crystalline layers on the substrate, which provides a lithographic mask for patterning organosilanes. Next, a 2 × 2 cm^2 block of polydimethylsiloxane (PDMS) (Sylgard 184, Dow Corning) was prepared for patterning octadecyltrichlorosilane (OTS) (Gelest, Morrisville, PA). A 30 µL volume of a 30% v/v solution of OTS in bicyclohexyl (Sigma Aldrich, St. Louis, MO) was deposited on the surface of the PDMS block and then dried quickly with a stream of nitrogen. The "inked" PDMS block was placed on top of the masked silicon substrate. The areas of contact between the latex mesospheres and substrate are protected from deposition of OTS during contact printing. After 1 h, the PDMS block was removed from the sample and the surface was rinsed with deionized water. The mask of latex particles was removed completely by rinsing with ethanol (Pharmco, Aaper, Tx) and deionized water several times, using sonication. After removal of the latex mask, a layer of OTS persists on the surface with periodically arranged circular-shaped holes of uncovered substrate (Figure 7.1A). The holes define reactive areas of the surface for immobilizing a nickel-functionalized catalytic initiator (Figure 7.1B) using solution immersion protocols. The nanopatterns of covalently attached initiator defines the surface selectivity for *in situ* living polymerization. *In situ* living

polymerization is accomplished by immersing the sample in a solution of Grignard monomer to produces nanostructures of polythiophene thin films on the surface (Figure 7.1C).

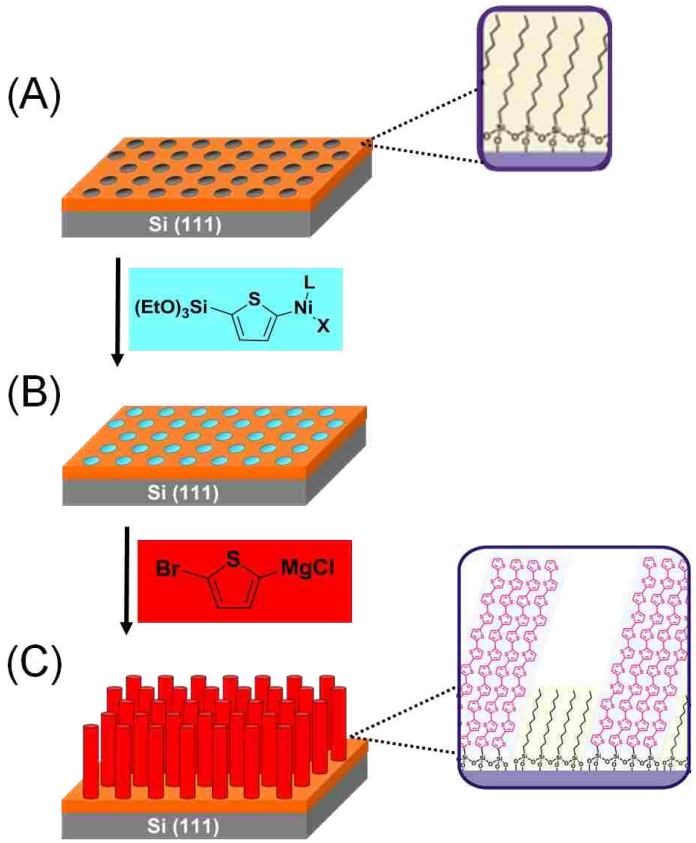

Figure 7.1 Procedure for fabricating surface nanopatterns of polythiophene nanopillars within thin films of OTS. (A) Periodic arrays of nanoholes of uncovered Si(111) substrate produced by particle lithography combined with contact printing; (B) nanoholes define sites for the surface immobilization of nickel-functionalized catalytic initiator (L = 1,3-bis(diphenylphoshino) propane); (C) *in situ* living polymerization genenerates periodic nanopillars of polythiophene on the surface.

7.2.2 Atomic Force Microscopy

Samples were characterized with a model 5500 atomic force microscope (AFM) equipped with Picoscan v5.3.3 software (Agilent Technologies, Chandler, AZ). Images were acquired using contact mode in ambient conditions. Oxide-sharpened silicon nitride cantilevers with force constants ranging from 0.1 to 0.5 N/m were used for imaging (Veeco Probes, Santa Barbara, CA). Digital images were processed with Gwyddion open source software (version 2.9), which is supported by the Czech Metrology Institute.[140]

7.3 Results and Discussion

The surface morphology of a polythiophene film prepared on a quartz substrate are shown in AFM topography frames in Figure 7.2. The successive zoom-in views are representative of the morphology observed throughout areas of the entire sample. The morphology of the film is fairly smooth and continuous with the overall changes in height measuring 11 nm. There are a few line spikes in the images which results from strong tip-surface adhesion. The corresponding lateral force image in Figure 7.2B indicates a homogenous composition with small round domains arranged throughout the surface. Close-up views of the film are shown for a 2 × 2 μm^2 scan area in the topography and lateral force images in Figures 7.2C and 7.2D, respectively. The images show irregular globular domains, with an rms roughness of 1.5 nm.

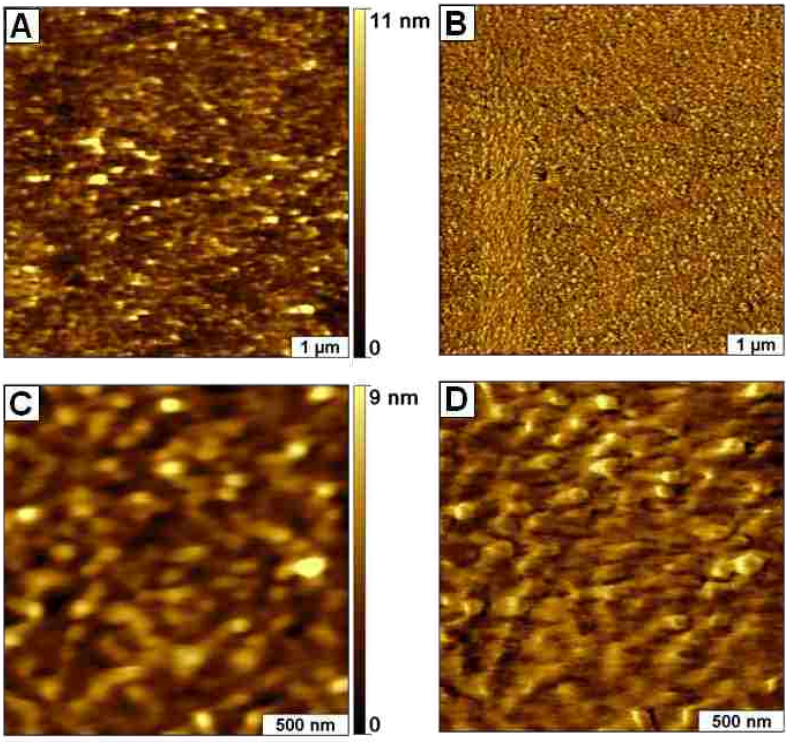

Figure 7.2 Morphology of a polythiophene film prepared on a quartz substrate viewed with contact mode AFM images. (A) Wide area view of surface topograph (6 × 6 μm^2); (B) simultaneously acquired lateral force image; (C) close-up topography view (2 × 2 μm^2); (D) corresponding lateral force image.

To determine the thickness of the polythiophene film, an AFM tip was used to shave a hole in the surface to expose a small area of the underlying quartz substrate (Figure 7.3). The AFM-based process of nanoshaving has been used previously to inscribe holes in different thin film materials,[189] such as *n*-alkanethiol self-assembled monolayers (SAMs),[190] organosilane films,[139, 191] multilayers of 4,4'-dimercaptobiphenyl,[192] sexiothiophene crystals,[193] porphyrin films,[194] films of molecular micelles,[195] and different polymers[196-201]. For nanoshaving, a high force is applied to the AFM tip during scanning to uncover a small hole in a film to expose the underlying substrate. Nanoshaved patterns are generated by scanning over a small area several times, while applying a higher force than used for imaging. The local pressure applied to an AFM tip at the area of contact produces high shear forces to displace adsorbate molecules during rastering. The exposed substrate of the nanoshaved areas provides a baseline for measuring the film thickness.

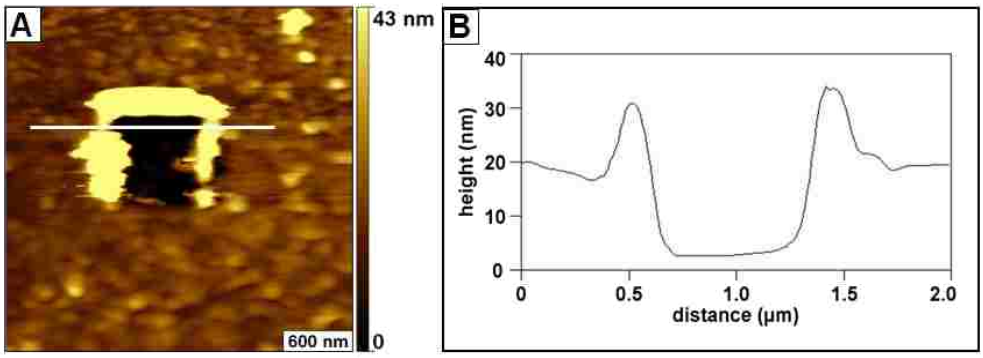

Figure 7.3 Thickness of a polythiophene film prepared by surface initiated living polymerization measured by nanoshaving. (A) AFM topograph of a 700 × 700 nm^2 nanoshaved hole in the film; (B) height profile for the line drawn across the pattern in **A**.

A square region of a polythiophene film prepared on a quartz substrate was nanoshaved in air as shown in the AFM topograph of Figure 7.3A. In liquids, the displaced adsorbates can be pushed to other areas of the substrate. However, since this experiment was accomplished in air the adsorbates piled up at the sides of the nanopattern. The boundaries of the nanoshaved square are taller than the surrounding areas of polythiophene; therefore, the cursor line was extended

past the edges of the pattern to reference the outer areas of the film for measuring the film thickness (Figure 7.3B). The cursor profile in Figure 7.3B is a representative example of several cursor profiles. Referencing the nanoshaved areas as a baseline, the thickness of the film measured 18 $\pm$ 2 nm. The flatness of the line shown in the height profile evidences that molecules were cleanly removed from within the nanoshaved area.

A hybrid method of nanolithography which combines particle lithography with contact printing of organosilanes was used to prepare nanoholes within an OTS film on the surface of a polished silicon wafer, Si(111).[202] The surface passivated with nanostructures of OTS served as a template for bottom-up fabrication of nanopatterns of polythiophene nanopillars prepared by surface-initiated living polymerization. An example of nanoholes produced using 300 nm latex mesospheres as a surface mask is shown in Figure 7.4. The local roughness of mechanically polished silicon wafers prevents us from distinguishing the pore structures in topography views (Figure 7.4A). However, the simultaneously acquired lateral force images clearly resolve the nanopatterns in Figure 7.4B. The lateral force images show changes in frictional forces and stick-slip adhesion for tip-surface interactions. The dark circles are areas of uncovered silicon substrate that were masked by latex spheres during contact printing whereas the bright areas are composed of OTS. The latex films were effective masks for contact printing of OTS since the center areas of the nanopores do not show any OTS adsorbates. There are 747 nanoholes within the 8 x 8 μm^2 image of Figure 7.4B, which scales up to a surface density of 1.2 x 10^9 nanoholes per cm^2. The calculated surface coverage of OTS was 67.4%. A zoom-in view of the surface nanopatterns reveals more clearly the circular shapes and hexagonal arrangement of the nanoholes (Figure 7.4D). The center-to-center spacing between each nanohole closely matches the expected 300 nm diameter of the latex masks, however the actual size of holes is smaller than the periodicity. Cursor measurements of 100 nanopatterns from several different areas of the

surface reveal a lateral periodicity of 292 ± 7 nm, while the edge-to-edge distance of the nanopores measured 162 ± 8 nm. For OTS nanopatterns prepared by particle lithography combined with contact printing, the surface roughness of 1.9 nm prevented accurate measurement of the heights of OTS.

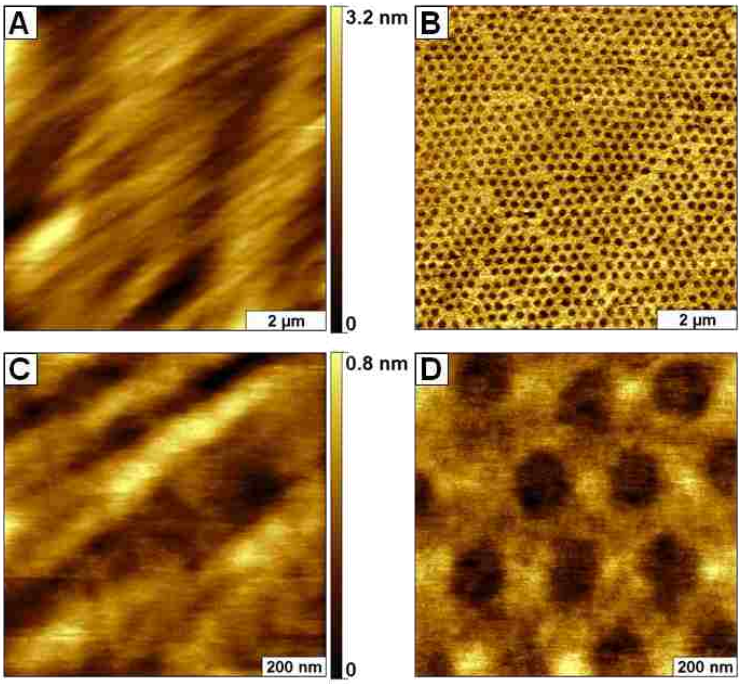

Figure 7.4 By combining particle lithography with contact printing, an array of circular holes of uncovered Si/SiO_2 substrate was prepared within an OTS film using 300 nm latex masks. (A) In a wide area AFM topograph (8 × 8 μm^2) the nanoholes cannot be resolved; (B) the corresponding lateral force image clearly reveals the periodic array of hole nanostructures; (C) at higher magnification (1 × 1 μm^2), the topography image still does not resolve the nanopatterns; (D) the spacing and dimensions of the holes can be clearly viewed in the lateral force frame.

The array of nanoholes of uncovered substrate provides exquisitely regular, well-defined sites for the surface immobilization of polythiophene. The interstitial areas between the nanoholes are covered with methyl-terminated OTS and provide an effective resist during further steps of chemical modification. Nanopillars of polythiophene were successfully prepared using the OTS nanostructures as a foundation layer, demonstrated by the contact mode AFM images in Figure 7.5. The long-range order of the polythiophene brushes (bright dots in Figure 7.5A) is shown with a representative 8 × 8 μm^2 topograph and lateral force image (Figure 7.5B). The

regular arrays of polythiophene nanostructures were displayed throughout areas of the entire surface, evidencing the high-throughput capabilities of particle lithography. After backfilling the uncovered holes with polythiophene, the approximate surface coverage of OTS measured 66%, which matches closely with the 67% surface coverage of OTS before backfilling. A 2-D fast Fourier transform (FFT) analysis of the 8 × 8 μm^2 topography image displays the reciprocal space and periodicity of the nanostructures (Figure 7.5C). The bright features in the FFT image exhibit a hexagonal pattern and demonstrate the long-range ordering of the arrays. The symmetric arrangement of the brush patterns can be viewed more clearly in the successive zoom-in views (3 × 3 μm^2) of topography and simultaneously acquired lateral force images shown in Figures 7.5D and 7.5E, respectively. A line profile (Figure 7.5F) across ten polythiophene nanostructures shows heights ranging from 16 to 38 nm. The center-to-center spacing between nanopatterns measured 289 $\pm$ 10 nm, closely matching the diameter of the latex mesospheres used for the surface mask. With particle lithography combined with contact printing, the periodicity and surface coverage can be tuned by using different size latex masks. To obtain perfect nanoscale geometries would require an absolutely flat surface at the atomic level and perfectly symmetric monodisperse latex spheres. In a natural situation, there are few surfaces that are atomically flat and the variation in the sizes of latex spheres ranges from one to five percent. These small imperfections lead to different pore sizes, which produced variations in height for the nanopillars. The percent variation for 200 nanostructures measured measured 37%.

The geometries of the polythiophene pillars are more clearly viewed with high resolution images of 13 nanostructures in Figures 7.5G and 7.5H. The average width of the polythiophene nanopatterns measured 169 $\pm$ 9 nm (FWHM $\pm$ SD). The width of the pillars is defined by the dimensions of the OTS pores, closely matching the original sizes of the nanopores of Figure 7.4. Distinct valleys between the polythiophene pillars are apparent in the topographs, indicating that

surface-initiated polymerization did not take place in areas passivated with OTS. A cursor measurement across three of the taller patterns indicates heights of 27 ± 2 nm (Figure 7.5I).

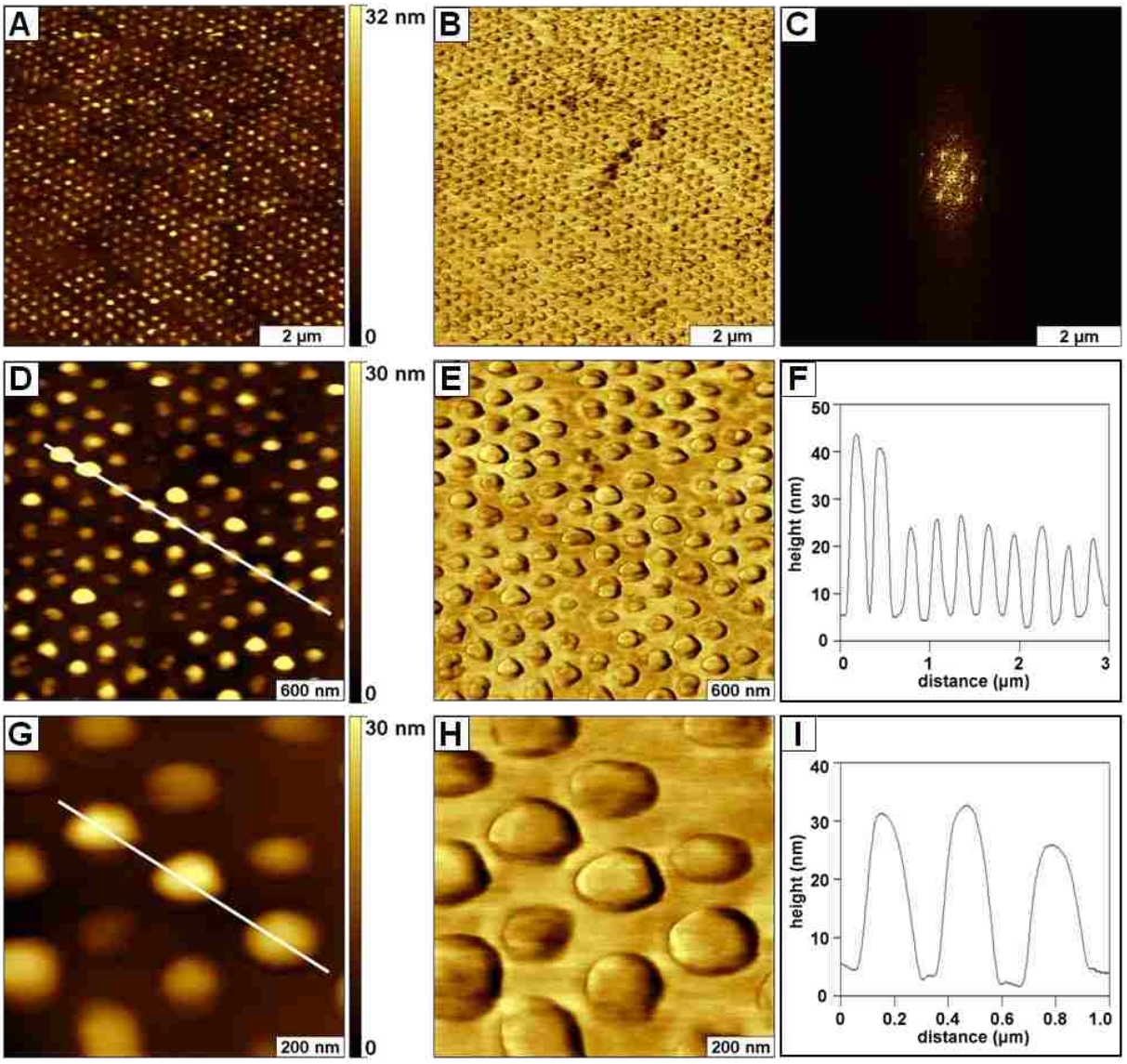

Figure 7.5 Arrays of polythiophene nanopillars produced by backfilling nanopores fabricated within OTS films using 300 nm latex masks. (A) Wide area topographic view of the polythiophene surface patterns obtained with contact mode AFM; (B) corresponding lateral force image; (C) 2D FFT spectrum generated from the topograph in A; (D) zoom-in view (3×3 µm^2) topograph; (E) corresponding lateral force image for **D**; (F) cursor plot for the line in **D**; (G) high resolution topograph (1×1 µm^2); (H) lateral force image for **G**; (I) height profile for the line in **G**.

The results presented in Figure 7.5 demonstrate that the nanopores prepared by particle lithography furnished an excellent surface template to define the locations for the covalent

immobilization of Ni-functionalized catalytic initiator. The nanopatterns spatially confine the growth of the polymer during living polymerization to produce tightly-packed molecules that are vertically aligned to the surface. Since *in situ* polymerization can only occur on locations of the surface with initiator, the resulting polythiophene nanostructures retained the initial surface-patterned geometry to generate circular-shaped, vertically aligned pillars.

7.4 Summary

By combining particle lithography with surface initiated living polymerization, nanopatterns of semiconducting polymer films with controlled morphology and geometry are produced on Si(111). Billions of semiconducting polythiophene nanostructures with discrete domains and designed intervals are reproducibly generated. The size and interpattern spacing of the nanostructures can be tailored by using different size latex mesospheres. Such control of the molecular orientation and nanoscale morphology of conducting polymer materials will facilitate carrier transport towards the top and bottom electrodes in thin film photovoltaics and, therefore, can potentially enhance the device efficiency. Future work is in progress to apply the described nanofabrication method on a transparent ITO electrode, which is suitable for the construction of an OPV device.

CHAPTER 8. CHARACTERIZATION OF DESIGNED ORGANOSILANE TEST PLATFORMS IN AIR AND IN LIQUID ENVIRONMENTS USING ATOMIC FORCE MICROSCOPY CONFIGURED WITH INDIRECT MAGNETIC MODULATION OF PROBES

8.1 Introduction

Dynamic characterizations using force modulation atomic force microscopy (FM-AFM) have been used for probing local mechanical properties (e.g. elastic and viscoelastic properties) of thin films and surfaces with nanoscale resolution.[51-53, 56, 58, 203-204] The local elasticity or stiffness of surface structures can be evaluated with phase and amplitude images.[53, 55-58] For the most common configuration of force modulation, the entire sample is driven to vibrate and the tip is held in a fixed position. Sufficient force is applied to the probe to ensure that continuous contact with the surface is maintained so that the tip does not break contact with the surface. Thus, for studies with FM-AFM, the force applied to the sample is modulated by applying a periodic AC waveform signal to a piezoactuated sample stage. The magnitude in which this force deforms the sample depends on the viscoelastic properties of the sample.[58] In this report, we investigate the applicability of an alternate instrument configuration for FM-AFM using indirect magnetic modulation (IMM) of the AFM tip.[20] In this situation, the tip is indirectly driven to vibrate against the sample surface by magnetic forces of a solenoid stage, rather than using piezoactuation. This configuration has advantages for precisely controlling the modulation of the probe and is suitable for protocols in either ambient or liquid environments.

There are several instrument configurations for force modulation using different approaches for driving the tip to oscillate. One strategy for inducing tip vibration is to apply a periodic AC signal directly to the segment of the piezotube which drives the tip to oscillate in the z-direction.[58] Another setup applies a periodic AC signal to a small piezoceramic chip to directly drive the tip to vibrate.[52] For an approach known as magnetic force modulation, probes which

have a magnetic coating on the topside can be driven to vibrate with an external AC electromagnetic field. field.[59, 205-207] Thin magnetic films can be deposited on AFM tips either by heated metal evaporation or by gluing small magnets onto the cantilever.[59]

An alternate instrument configuration for FM-AFM using indirect magnetic modulation of soft, non-magnetic cantilevers (spring constants <1 N/m) is evaluated in this report, for sample test platforms of designed organosilane nanostructures. In IMM, an external AC electromagnetic field, which is supplied by a wire coil solenoid located beneath the sample plate, is applied to the tip holder assembly of the AFM scanner. The tip is driven to vibrate indirectly through the motion of the tip holder assembly or nosecone, which contains ferromagnetic components. Three channels of data are acquired simultaneously with IMM to generate topography, amplitude, and phase images. Phase and amplitude images provide a map of elastic and viscoelastic properties of the sample. Different frequencies and field strengths can be chosen to drive the nonmagnetic cantilever to oscillate.

8.2 Experimental Section

8.2.1 Materials and Reagents

Double-side polished Si(111) wafers doped with boron were used as a substrates (Virginia Semiconductor Inc., Frederickburg, VA). The substrates were cleaned with piranha solution (3:1 v/v) containing sulfuric acid (96%, EMD Chemical Inc., Gibbstown, NJ) and hydrogen peroxide (30%, Sigma Aldrich). Ethanol (200 proof) was used for sample preparation and for AFM imaging media (Aaper Alcohol and Chemical Co., Shelbyville, KY). After acid cleaning, silicon substrates were rinsed with deionized water (18 MΩ•cm, Milli-Q, Millipore, Bedford, MA). Certified particle size standards of monodisperse polystyrene latex mesospheres (100 and 200 nm diameters) were purchased from Duke Scientific (Palo Alto, CA). For IMM studies, 2-[methoxy(polyethyleneoxy)propyl]trichlorosilane (PEG-silane) and N-(6-

aminohexyl)aminopropyltrimethoxysilane (6-AAPTMS) were purchased from Gelest (Morrisville, PA) and used to fabricate nanostructures.

8.2.2 Preparation of Organosilane Nanostructures

The procedure for preparing ring nanostructures of organosilanes has been previously reported.[16, 71-72] The samples for IMM studies were prepared by particle lithography combined with chemical vapor deposition using silicon substrates. Monodisperse latex mesospheres were washed several times with deionized water by centrifugation to remove contaminants. A drop of aqueous solution containing monodisperse latex particles was deposited on a clean substrate and dried in air at room temperature for at least 12 h. The crystalline layer of latex mesospheres provided a mask for vapor deposition of organosilanes. Next, the masked substrate was placed in a reaction chamber containing 300μL of the neat organosilane. The chamber was sealed and placed in an oven at 80°C to generate silane vapors. The organosilane molecules self-assemble from the vapor phase onto areas of the substrate where water residues are present. Directly beneath the spheres were areas of the substrate that remained masked and protected from adsorbing molecules. After at least 8 h of exposure to the organosilane vapors, the sample was then cooled to room temperature. In the final step, the latex particles were completely removed by rinsing and sonicating with ethanol and deionized water. A representative image of the ring-shaped nanopatterns of PEG-silane is shown in the 3D topograph acquired with tapping mode AFM in Figure 8.1A. The ring patterns were generated using a latex mask of 100 nm, with a surface density of 56 rings within the $1 \times 1\ \mu m^2$ view. Referencing the uncovered areas of the substrate as a baseline, the height of the PEG-silane nanostructures measures 2.6 ± 0.4 nm (Figure 8.1B).

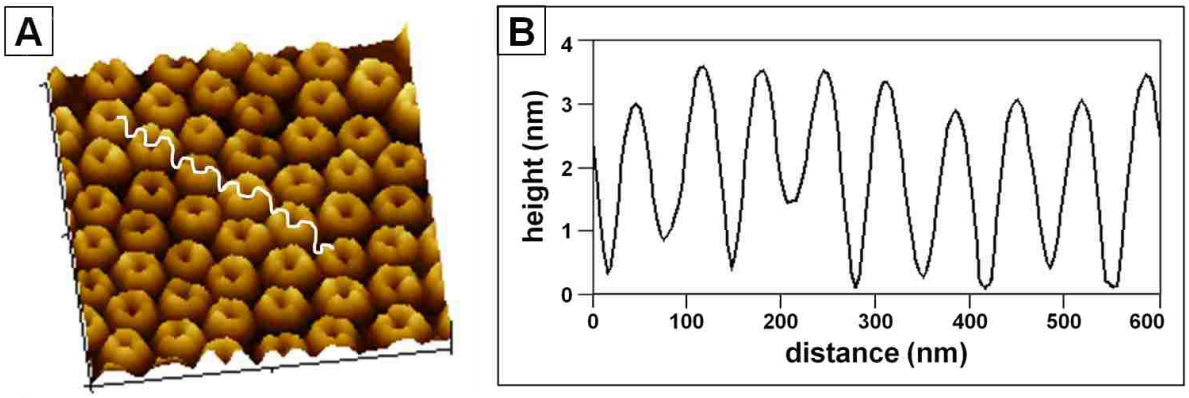

Figure 8.1 Nanopatterns of PEG-silane on Si(111) prepared by particle lithography using 100 nm latex masks. (A) Tapping-mode AFM topograph acquired in air; (B) height profile for the cursor line shown in **A**.

8.2.3 Indirect Magnetic Modulation AFM Imaging

A multipurpose scanner was used for IMM investigations with an Agilent 5500 model atomic force microscope (Agilent Technologies, Tempe, AZ) equipped with Picoscan v5.3.3 software. Oxide-sharpened Si_3N_4 microcantilevers (Veeco, Santa Barbara, CA) with a force constant of 0.1 N/m and a resonance frequency of 26 kHz were used for experiments. Gwyddion software was used for image processing, which is supported by the Czech Metrology Institute and is available for downloaded at no cost on the internet.[140]

The instrument setup for IMM AFM uses a magnetic AC mode (MAC-mode) sample stage containing a wire coil solenoid located underneath the sample plate.[20] A magnetic field is generated by applying an alternating current to the solenoid. The flux of the electromagnetic field induces vibration of the entire nosecone assembly (Figure 8.2); therefore, standard nonmagnetic probes can be used for IMM experiments. The AFM tip is driven to vibrate indirectly through the motion of the nosecone assembly. For each experiment, frequency sweeps are acquired before and after the tip has made contact with the sample surface to obtain information about tip resonances. The amplitude and phase response of the tip motion is

monitored by a photodiode detector and lock-in detection, using the AC current waveform as a reference input signal.

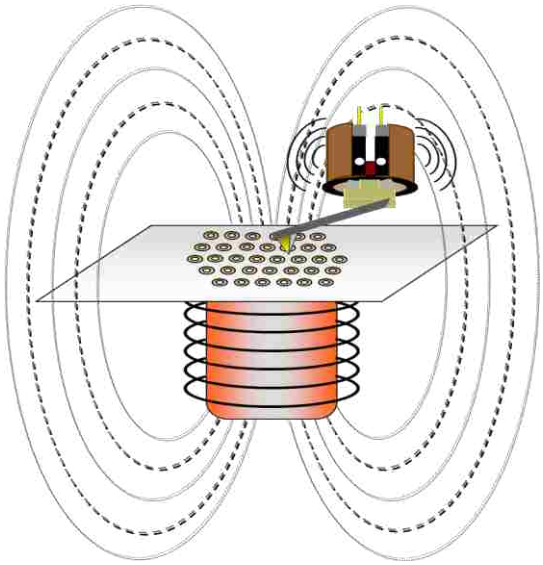

Figure 8.2 Instrument set-up for IMM using a wire coil solenoid to apply an AC electromagnetic field to the sample stage and tip holder assembly. The AFM probe is nonmagnetic and is driven to vibrate indirectly by vibration of the tip holder assembly driven by the flux of the electromagnetic field.

8.3 Results and Discussion

Silane nanostructures of defined geometries and designed surface chemistry fabricated using particle lithography combined with chemical vapor deposition provide a robust test platform for systematic investigations using IMM. Nanopatterns of organosilanes have a distinctly different elastic response than to the hard surfaces of Si(111) substrates and will provide practical nanostructured morphologies for testing the capabilities and resolution of IMM.

8.3.1 Force Modulation Spectroscopy Using IMM

With force modulation imaging, resonances arise directly as a result of tip-surface contact.[203] For experiments with IMM, frequency spectra were acquired while the tip was disengaged from the surface and after the tip was placed in contact with PEG-silane nanopatterns prepared on a silicon substrate (Figure 8.3). For side-by-side comparisons, the spectrum obtained

when the tip was engaged was offset by 0.10 V in the y-direction. Several peaks in the spectrum either shift slightly to the left or decrease in amplitude as the tip is brought into contact with the sample. The most prominent peaks for tip-surface resonance frequencies are observed at 48, 148, and 306 kHz when the tip was engaged with the sample (peaks A, B, and D in Figure 8.3). Notice that the peak at 148 kHz (peak B) is not detected in the spectrum when the tip is disengaged, which suggests that this resonance arises primarily from tip-sample interactions. For evaluation purposes, frequencies where a peak was not present (e.g. 226 and 424 kHz) were evaluated for IMM imaging, to assess the dependence of IMM imaging on the driving frequency of the tip.

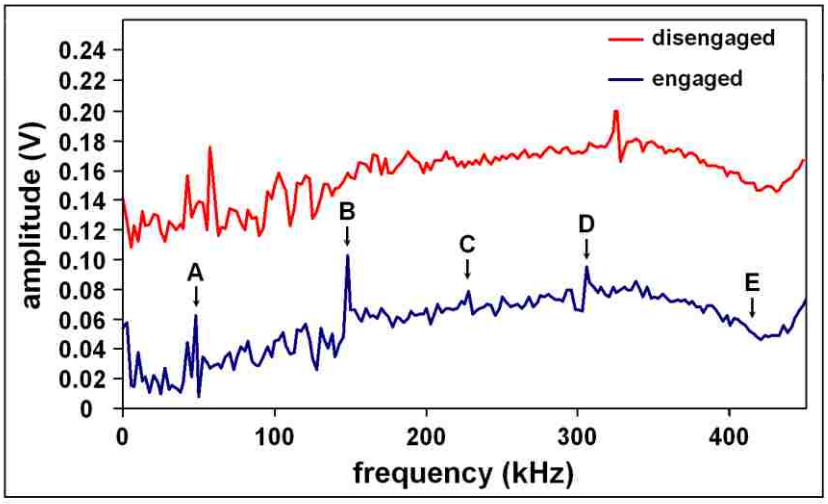

Figure 8.3 Frequency spectra acquired in ambient conditions for monitoring the response of a nonmagnetic AFM probe to IMM.

Since the entire tip-holder assembly is driven to vibrate in response to an applied AC field, both the natural resonances of the entire tip-holder assembly and background vibrations of the sample stage can be seen in the frequency spectra. Resonance peaks observed when the tip is placed in contact with the sample are typically stronger than those from when the tip is out of contact; these stronger resonances likely arise from coupling with the inherent mechanical vibrations of the tip holder assembly. Peaks which appear only upon contact with the sample,

such as the peak at 148 kHz (peak B in Figure 8.3), are attributed to resonances of the tip-sample contact. Additional peaks can result from overtones or resonances of the mechanical system.[20]

8.3.2 Evaluation of the Frequency Dependence for Imaging with IMM

After obtaining the frequency spectrum, individual images of PEG-silane nanopatterns (Figure 8.4) were acquired with IMM in ambient air. To evaluate the frequency dependence of IMM, certain driving frequencies ranging from 49 to 424 kHz (Figure 8.3, labeled A-E) were chosen for driving the tip to vibrate. The data set presented in Figure 8.4 was obtained during a single experiment using the same tip and force setpoint. In addition, approximately the same area of the sample was scanned, using the two missing patterns in each image as a frame of reference. Ring-shaped nanopatterns of PEG-silane are clearly distinguishable from the bare silicon substrate in the images acquired at selected driving frequencies. In the topography frames, the brighter areas correspond to the taller features of PEG-silane nanostructures, whereas the darker areas correspond to the silicon substrate. Since the topography views reflects the height of the surface features detected by the AFM tip, the color scales for differences in height remain constant for each topography frame, regardless of the driving frequency used for imaging. However, the color contrast in amplitude images depends sensitively on the frequency used for driving the tip vibration and reflects changes in the local viscoelastic response of the sample. In the amplitude and phase channels, the magnitude of response of the AFM tip scales according to different driving frequencies. Less contrast is detected in the phase images for Figures 8.4C and 8.4E, and the ring patterns are not as clear and distinct as in the phase images for Figures 8.4A, 8.4B, and 8.4D. The light contrast seen in Figures 8.4C and 8.4E corresponds to the magnitude of the frequencies selected to acquire these images, 226 and 424 kHz. In comparing the five selected frequencies in Figure 8.3, the smallest peaks are observed at 226 and 424 kHz, which

resulted in the weakest amplitude and phase response observed throughout the corresponding images.

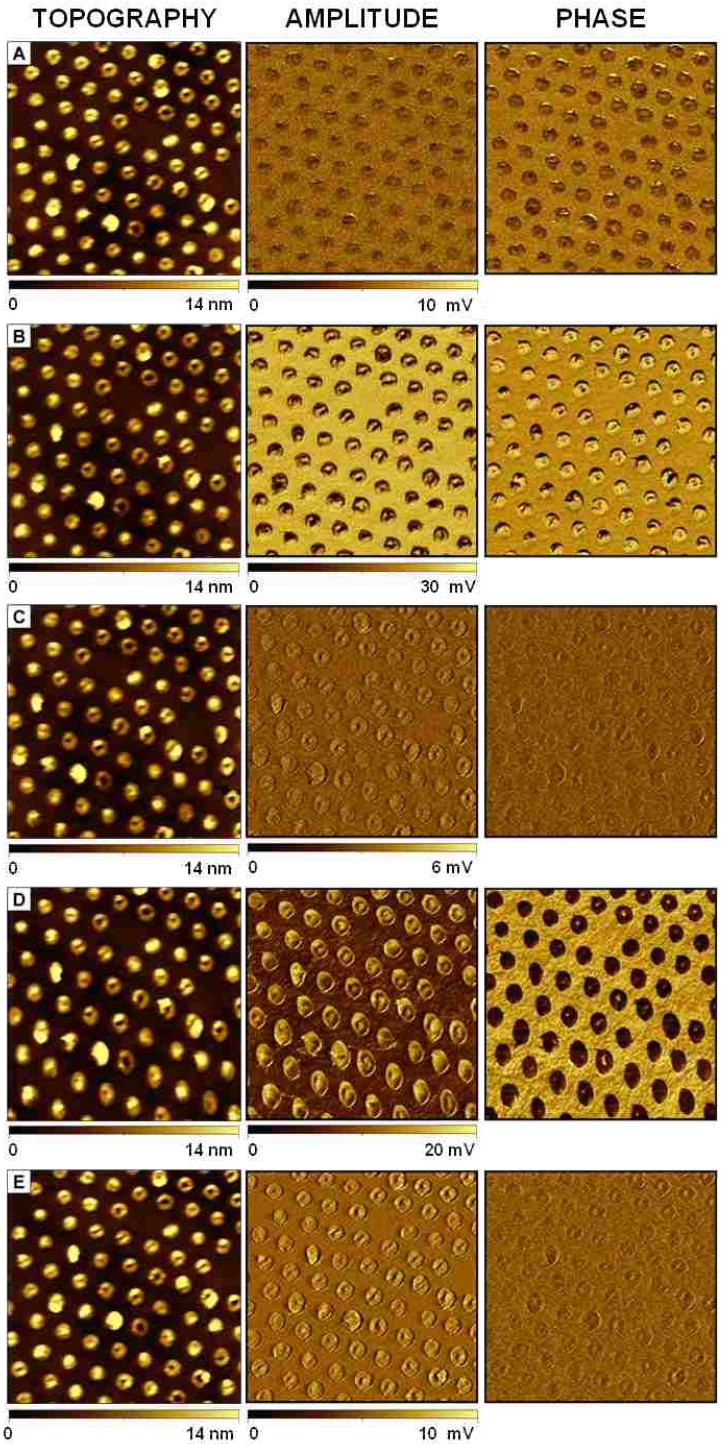

Figure 8.4 IMM images acquired in air of PEG-silane nanopatterns obtained at driving frequencies of (A) 48, (B) 148, (C) 226, (D) 306, and (E) 424 kHz (frequency spectra is shown in Figure 7.3). Images are 2 x 2 μm^2 scan sizes.

The contrast observed in the amplitude images directly corresponds to the response of the tip-sample contact of the vibrating tip. When in contact with soft materials (e.g. PEG-silane molecules), the cantilever oscillates at reduced amplitudes and changes phase in reference to the driving signal. For IMM, the amplitude and phase of the cantilever oscillation depends on interactions between the tip and the surface. Therefore, information about surface elasticity can be mapped with IMM amplitude and phase images. The amplitude images in Figure 8.4 A-E clearly distinguish the locations of the softer PEG-silane molecules and the harder silicon substrate. Factors which determine whether surface structures are displayed as being light or dark in force modulation amplitude and phase images are the frequency or amplitude chosen for driving tip vibration,[46, 208-209] as well as whether the tip is operating in the attractive or repulsive regime.[209-211]

Results for a dynamic IMM experiment are shown in Figure 8.5 for ring patterns of 6-AAPTMS characterized at two selected frequencies. Midway through the scan, in Figure 8.5A, the top half of the 4 x 4 μm^2 scanned area of the sample was analyzed using a driving frequency of 136 kHz, while the bottom half was acquired at 156 kHz. Data acquisition was not interrupted when switching frequencies during imaging. There is a distinct boundary in the phase image that points out where the frequencies were switched from 136 to 156 kHz. As for the amplitude image, only a faint change in contrast is observed between the two halves of the image. The amine-terminated 6-AAPTMS ring nanostructures measured 4.5 $\pm$ 0.2 nm in height. The uncovered areas of the Si(111) surface show matching contrast within the center holes of the nanostructures. These small central areas measure 46 $\pm$ 8 nm in diameter, which demonstrates that IMM is exquisitely sensitive to changes in surface chemistry at scales of a few nanometers.

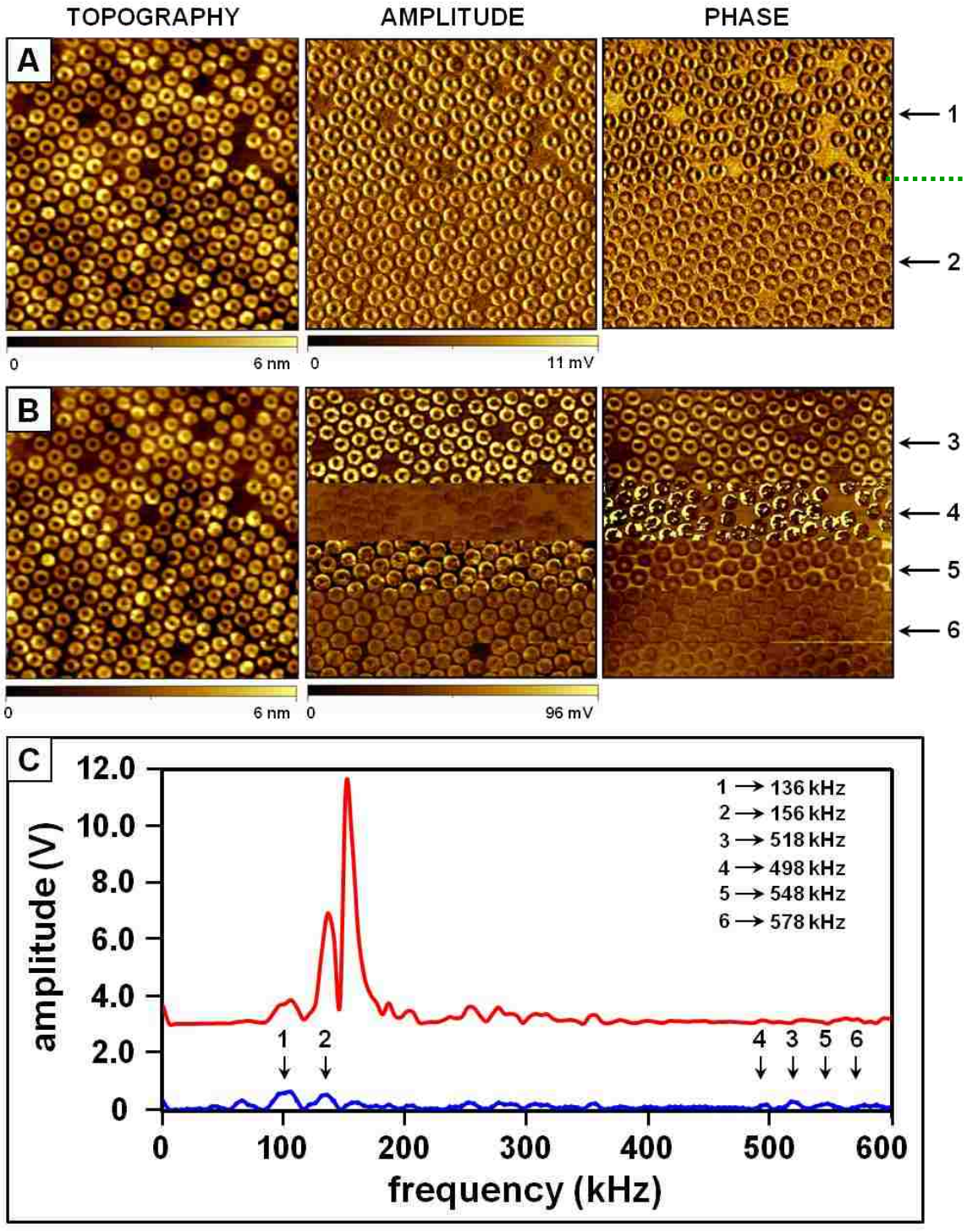

Figure 8.5 Dynamic IMM experiments with nanopatterns of 6-AAPTMS (200 nm) analyzed at selected frequencies in air. Images captured at (A) low frequencies and (B) high frequencies as the frequency was ramped at different points during a single scan. Images are 4 x 4 μm^2 scans. (C) Frequency spectra acquired before (red line) and after (blue line) the tip was placed in contact with the sample; the magnetic field remained on during acquisition of both spectra.

Higher frequencies were also selected for side-by-side comparison of amplitude and phase response within a single image shown in Figure 8.5B. While scanning across a 4 x 4 μm^2 area, the driving frequency was switched without stopping data acquisition. For images acquired in air, the 6-AAPTMS ring patterns exhibit regular circular geometries throughout the entire image for the different frequencies. Sharp changes in contrast are immediately detected in the amplitude and phase images when the frequency is changed, demonstrating that the tip motion instantly changes with the rhythm of the IMM driven oscillation. For the amplitude frames, the softer areas of the ring nanopatterns show bright contrast against a dark background for the substrate at every selected frequency except at 498 kHz. A contrast flip, where the rings become dark and the substrate becomes brighter, is observed for the amplitude frame at 498 kHz (4). The amplitude frames are less straightforward to interpret; dark rings on a light background are shown for peaks 1, 2, 5, and 6, whereas light rings on a dark background are detected for peaks 3 and 4. The phase changes for frame 4 show interesting edge effects, with a different contrast for the top versus the edges of the ring nanostructures. The contrast reversals for phase images are attributable to the complexity of both adhesion and stiffness interactions between the tip and sample and do not follow a predictable general scheme.

8.3.3 Influence of Liquid Media for IMM Imaging

One factor to be considered when imaging in ambient conditions is the presence of a thin film of water on the surface of samples.[203] Adsorbed water forms a capillary neck when the tip is in contact with the surface and results in a capillary adhesive force.[212] Measurements made in liquid media reflect more accurately the elastic and viscoelastic properties of the sample due to the absence of the capillary neck at the tip-sample contact area.[203] When imaging in air, a "forest" of peaks is often observed in the frequency spectrum obtained with FM-AFM. However, immersing the tip and sample entirely in a non-reactive liquid eliminates most of the peaks that

arise from background noise (electronic and acoustic). Imaging in liquid reduces many of the random perturbations of the tip to generate a spectrum displaying a few prominent and well-defined resonance peaks.

To evaluate the effects of imaging media on cantilever motion in response to IMM, frequency spectra were collected for a single sample in both ambient air and under a liquid environment. Analysis of the resonance behavior for a sample containing ring patterns of 6-AAPTMS nanostructures on a silicon substrate was first performed in ambient air (Figure 8.6A). A frequency spectrum was obtained again using the same sample, except under a liquid environment by introducing ethanol into the sample cell (Figure 8.6B). For both spectra, the y-axis for the disengaged tip has been offset by 0.2 V.

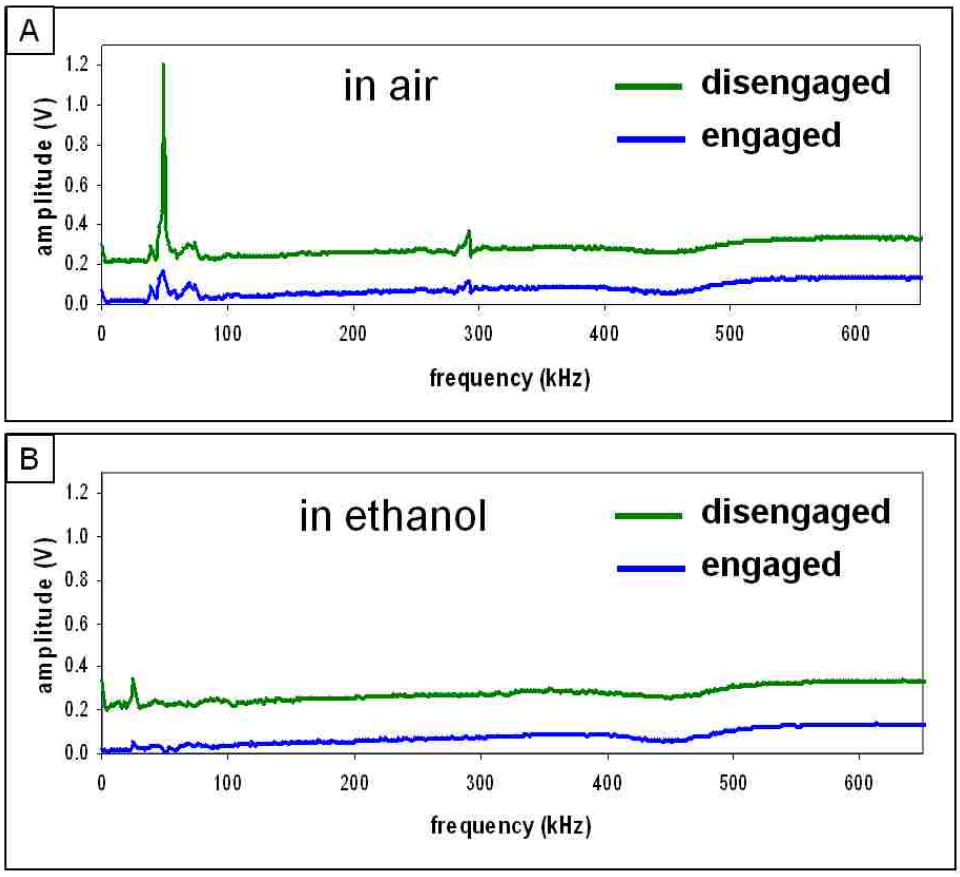

Figure 8.6 Frequency spectra obtained using IMM in (A) air and (B) in ethanol.

A prominent resonance peak is observed before the tip makes contact with the surface in Figures 8.6A and 8.6B. In both cases (in air and in ethanol), these peaks are dampened when the tip engages the surface. In comparing the spectra obtained in the two different environments for the engaged tip, the resonance peak is substantially smaller for the experiment in ethanol. This is attributable to the surrounding liquid media dampening the motion of the cantilever.

Topography, amplitude and phase images (2 x 2 μm^2) of the same 6-AAPTMS arrays were acquired in ethanol using IMM at selected driving frequencies (Figure 8.7). All of the frames were acquired for the same approximate area. The color scale in the topography frames remains unchanged regardless of which frequency was chosen. The tallest features are approximately 4 nm in height. However, the contrast and magnitude of response observed in the amplitude and phase frames changes according to the frequency selected for imaging. Bright rings against a darker colored substrate are displayed in all of the amplitude and phase images with the exception of the phase image acquired at 619 kHz, Figure 8.7E. This image reveals interesting edge effects, with a dark border surrounding the nanorings. Another interesting difference observed in liquid media is that for several of the amplitude frames, the center areas of the rings are darker than the surrounding substrate areas (Figures 8.7A, 8.7C, 8.7D, and 8.7E). This is attributable to fluid pressure and motion of the liquid media within the rings, which has a containment effect within the enclosed nanosized space at the centers of the rings.

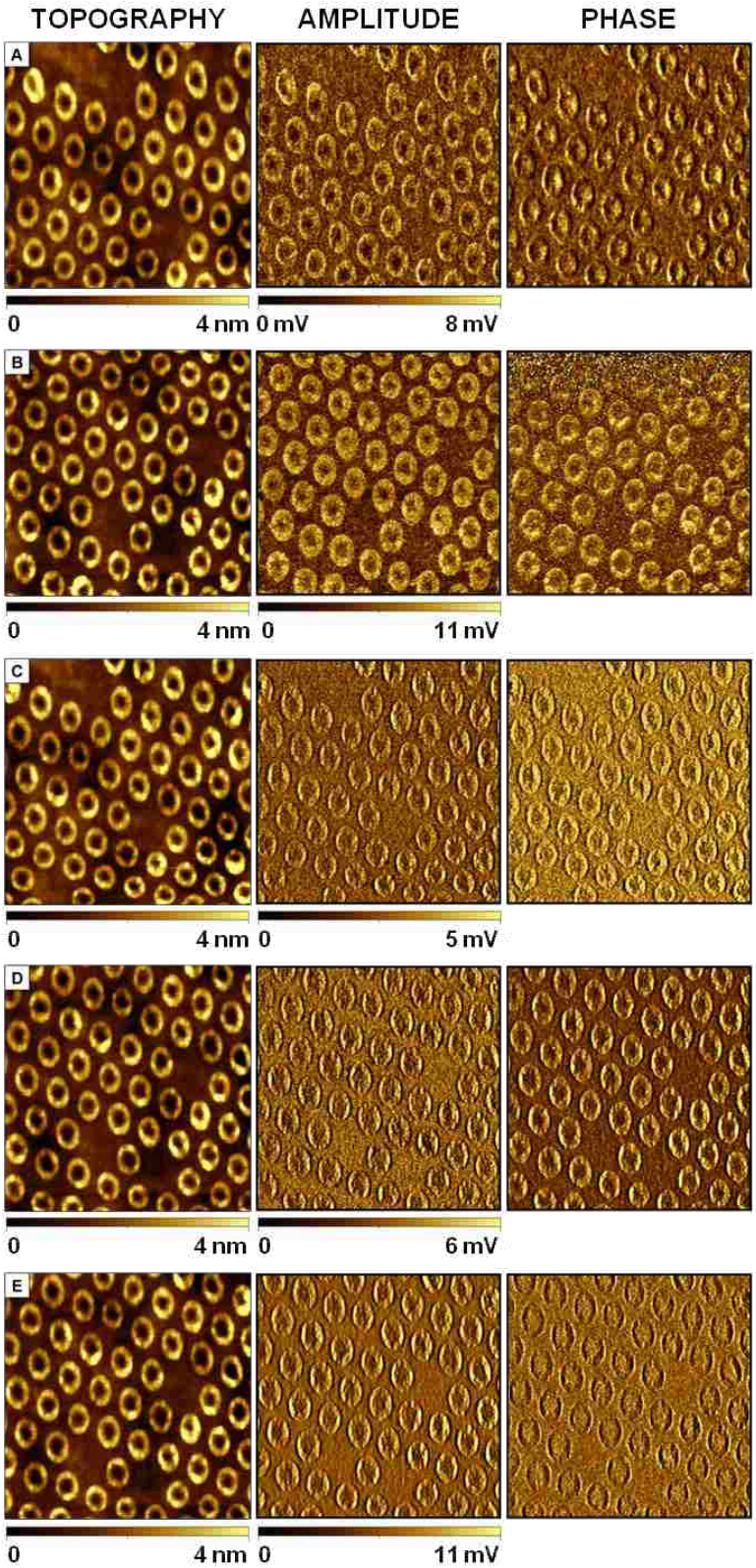

Figure 8.7 Liquid IMM experiments with 6-AAPTMS nanoring patterns (200 nm) acquired in ethanol at selected driving frequencies: (A) 23, (B) 69, (C) 433, (D) 462, and (E) 619 kHz. Images are 2 x 2 μm^2 scan areas.

The same sample of 6-AAPTMS nanostructures and local area of Figure 8.7 was imaged using the same probe in ethanol to evaluate the response of a nonmagnetic tip to an external magnetic field by IMM and for dynamic frequency studies, changing frequencies during acquisition of IMM scans. The magnetic field was alternately switched off and on during scanning without interrupting data acquisition (Figure 8.8A) at a driving frequency of 23 kHz. Interesting changes in the sample geometries were readily observed, which suggests that the surrounding liquid media is perturbed by the tip motion. The regular circular shapes of the ring nanostructures became distorted and appear as elongated ovals due to the changes in tip motion.

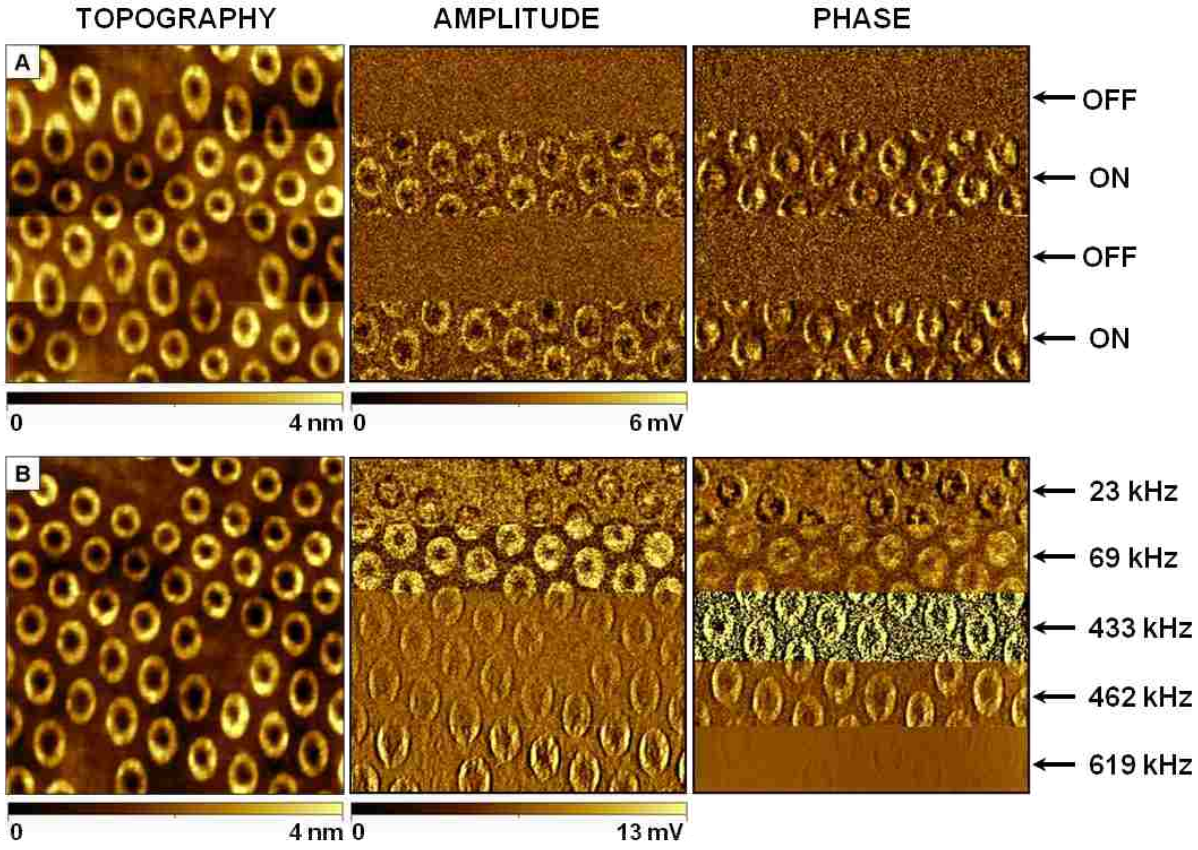

Figure 8.8 Dynamic IMM experiments conducted in liquid media for 6-AAPTMS rings (prepared from 200 nm latex). (A) IMM images (2 x 2 μm^2) obtained in ethanol with the magnetic field alternately switched off and on during data acquisition. (B) IMM frames acquired when switching frequency parameters during a single scan.

Switching the external electromagnetic field on and off during a single scan reveals the successive changes in tip oscillation when the periodic motion is interrupted and resumed within a single image scan. Clear linear boundaries are observed in the amplitude and phase channels in Figure 8.8A when the magnetic field is turned on or off. However, the topography view shows distortion of the ring geometry. In the topography image, the contrast between ring patterns and substrate remains the same regardless whether the field is on or off, because the topography data reflects only the height of the surface features as detected by the AFM tip. However, when the field is off, the rings appear to be somewhat elongated and distorted in the topography frame. The elongated ring patterns reflect the equilibration of the tip due to perturbation of the surrounding liquid media. Liquid media dampens the oscillatory motion of the cantilever during scanning, which requires more equilibration time for the wavemotion to subside. Note that when the field is turned off during IMM experiments, neither amplitude nor phase response of the tip is detected, as evidenced by the immediate loss of contrast for the ring patterns of 6-AAPTMS (Figure 8.8A).

Ramping the driving frequency of the tip from 23 to 619 kHz causes progressive changes in the observed geometry of the ring nanostructures, as shown in the topography frame of Figure 8.8B. The rings became elongated at higher frequencies. Changes in the phase response do not correspond to the amplitude frames. The phase images are highly sensitive to surface edge structures and the containment area within the center of the nanorings. The dynamic sweeps of certain frequencies provide a rapid *in situ* protocol for selecting imaging conditions for mapping surface chemistry with IMM.

8.4 Conclusion

An alternate instrument configuration for investigations with FM-AFM was evaluated in liquid media using test structures of organosilane ring nanostructures. The modulation of

nonmagnetic probes can be accomplished using indirect actuation of the tip holder assembly, and can be operated in both ambient air and in liquid media. The response of the cantilever is sensitively influenced by liquid media; perturbation is observed when the oscillation is turned on and off as detected by changes in apparent sample geometry. The liquid media is perturbed by the motion of the tip, particularly in tight spaces confined in the centers of the nanorings. Organosilane ring patterns prepared using particle lithography furnished a practical test platform for dynamic studies of surface properties, enabling the detection of changes in shapes and sensitivity of IMM to surface stiffness apparent at the nanoscale.

CHAPTER 9. CONCLUSIONS AND FUTURE PROSPECTUS

New nanofabrication methods combining particle lithography with molecular self-assembly were developed in this research for designed organosilane nanostructures. Monodisperse mesospheres of latex or colloidal silica naturally self-assemble on surfaces to form close-packed layers with designed dimensions and interparticle spacing. Colloidal crystals furnish a structural mask or template for guiding and controlling the deposition of materials on surfaces. The geometries and arrangement of nanostructures is determined primarily by the periodicity and dimensions of the mesospheres. The particle lithography methods described in this dissertation furnish high throughput approaches for reproducibly generating either ring or pore-shaped nanopatterns of organosilanes.

Nanopatterns of organosilanes with precise geometries and reproducible dimensions provide test platforms that are suitable for molecular-level investigations with AFM to gain insight on surface self-assembly processes of organosilanes. Characterization of surface nanostructures with selected AFM imaging modes (e.g., contact mode, lateral force imaging, tapping mode, phase imaging) demonstrate the high resolution capabilities of scanning probe measurements for obtaining structural and physical information of materials at the nanoscale. Details of silanation reactions and self-polymerization mechanisms were obtained with high resolution AFM. The development of indirect magnetic modulation (IMM) provided an alternate approach for investigating the elastic compliance of various organosilane nanostructures in ambient or liquid environments.

Particle lithography combined with either vapor deposition or contact printing of organosilanes provides a high-throughput tool for tailoring surface chemistry at the nanoscale. Nanostructures of organosilanes can be applied for the selective adsorption of nanoparticles, proteins or organic molecules. For example, arrays of ring-shaped OTS nanostructures were

successfully used for selectively depositing functionalized gold nanoparticles into confined regions (Chapter 5). Alternatively, pores of uncovered substrate produced within a thin film of OTS have been used for controlling the molecular orientation of polythiophene during surface initiated polymerization. Results of this dissertation research provide a solid foundation for future experiments. Further work will focus on applying particle lithography to pattern organosilane nanostructures, which will provide a scaffold for building more complex molecular architectures. Chemical post-modification of terminal functional groups of organosilane nanostructures will be applied for introducing active functional groups on the surface nanopatterns for selectively binding other molecules or nanomaterials, such as proteins. The ability to precisely control the relative position and arrangement of proteins at the nanoscale are important for development of advanced biosensor technologies.

The increasing demand for more advanced and cost-effective green technology has led to new developments in solar cell technology, such as organic photovoltaic (OPV) devices. To improve device performance of OPVs, ongoing research will continue for fabricating arrays of vertical polythiophene pillars within OTS thin films on transparent indium tin oxide (ITO) substrates using particle lithography and surface initiated living polymerization. With particle lithography combined with contact printing, billions of periodically arranged pillar nanostructures of polythiophene can be produced on the surface with relatively few defects. The dimensions and interpillar spacing can be selectively tuned by changing the diameter of latex mesospheres used for the surface mask. In future work, completion of the device will be accomplished in collaboration with Dr. Evgueni Nesterov at LSU. The spaces between polythiophene nanopillars will be filled with a suitable acceptor (n-type) material, and a top aluminum electrode will be deposited by metal evaporation. Control of the molecular organization of both donor and acceptor materials will provide advantages for efficient carrier

transport towards the top and bottom electrodes. The high throughput capabilities and reproducibility of particle lithography for generating organized arrays of polythiophene nanostructures offers a promising nanofabrication route that can potentially aid in the development of future OPV devices with improved efficiencies.

In addition, future studies will involve investigating the effect of nanoscale morphology on photoelectric properties of the polythiophene nanopillars using current sensing AFM (CS-AFM). Local measurements of the conductive properties with CS-AFM of polythiophene nanostructures will provide insight on the correlation between molecular structure/organization and sample conductivity with nanoscale resolution. Current sensing AFM is an advanced contact imaging mode which is useful for the characterization of conductive materials on surfaces. The probes used for CS-AFM are coated with a thin layer of a conducting metal (e.g., platinum, iridium, gold). For CS-AFM, a bias voltage is applied to a conductive or semi-conductive sample, and the current through the conductive material is measured when the AFM tip is placed in direct contact with the surface (Figure 9.1). The applied bias voltage between the tip and sample generates current flow, which is sensitively measured by the AFM tip using a preamp integrated within the nosecone assembly. Current images of the sample are digitally constructed by recording the changes in current during scanning. Sample conductivity, topography, and lateral force images are acquired simultaneously with CS-AFM. In addition, current voltage (IV) plots at a specific location on the sample can be obtained with CS-AFM. Future directions will be to use CS-AFM to directly measure and mapping photocurrents that are generated by OPV nanostructures at the molecular level. Samples prepared on conductive ITO substates will be used for developing these new measurements.

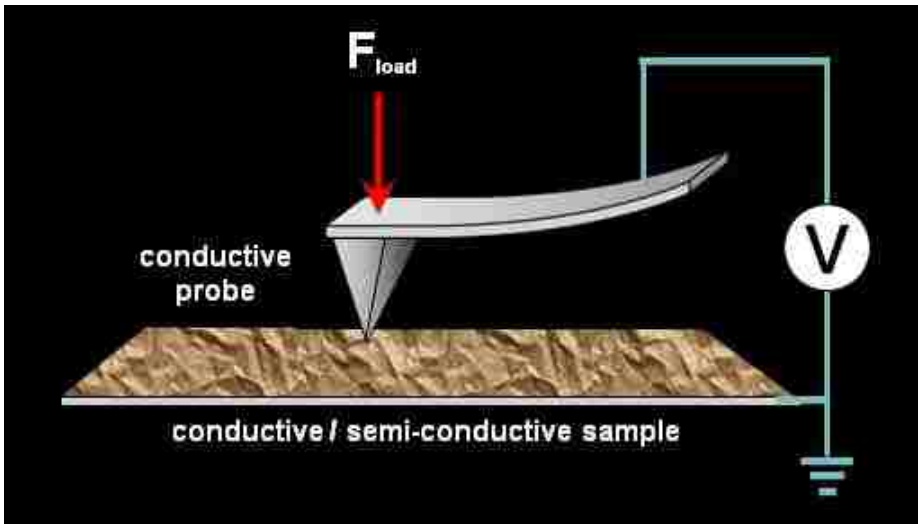

Figure 9.1 Operating principle of CS-AFM.

REFERENCES

1. Haes, A. J.; Van Duyne, R. P. A Nanoscale Optical Biosensor: Sensitivity and Selectivity of an Approach Based on the Localized Surface Plasmon Resonance Spectroscopy of Triangular Silver Nanoparticles. *J. Am. Chem. Soc.* **2002**, *124*, 10596-10604.

2. Mcfarland, A. D.; Van Duyne, R. P. Single Silver Nanoparticles as Real-Time Optical Sensors with Zeptomole Sensitivity. *Nano Lett.* **2003**, *3*, 1057-1062.

3. Kempa, K.; Kimball, B.; Rybczynski, J.; Huang, Z. P.; W u, P. F.; Steeves, D.; Sennett, M.; Giersig, M.; Rao, D. V. G. L. N.; Carnahan, D. L.; Wang, D. Z.; Lao, J. Y.; Li, W. Z.; Ren, Z. F. Photonic Crystals Based on Periodic Arrays of Aligned Carbon Nanotubes. *Nano Lett.* **2003**, *3*, 13-18.

4. Han, J.; Craighead, H. G. Separation of Long DNA Molecules in a Microfabricated Entropic Trap Array. *Science* **2000**, *288*, 1026-1029.

5. Landskron, K.; Hatton, B. D.; Perovic, D. D.; Ozin, G. A. Periodic Mesoporous Organosilicas Containing Interconnected [Si(CH2)](3) Rings. *Science* **2003**, *302*, 266-269.

6. Xie, X. N.; Chung, H. J.; Sow, C. H.; Wee, A. T. S. Nanoscale Materials Patterning and Engineering by Atomic Force Microscopy Nanolithography. *Mater. Sci. Eng. R-Rep.* **2006**, *54*, 1-48.

7. Li, D. B.; Bonnell, D. A. Controlled Patterning of Ferroelectric Domains: Fundamental Concepts and Applications. *Annu. Rev. Mater. Res.* **2008**, *38*, 351-368.

8. Zotti, G.; Vercelli, B.; Berlin, A. Monolayers and Multilayers of Conjugated Polymers as Nanosized Electronic Components. *Accounts Chem. Res.* **2008**, *41*, 1098-1109.

9. McCreery, R. L. Molecular Electronic Junctions. *Chem. Mater.* **2004**, *16*, 4477-4496.

10. Archakov, A. I.; Ivanov, Y. D. Analytical Nanobiotechnology for Medicine Diagnostics. *Mol. Biosyst.* **2007**, *3*, 336-342.

11. Muller, D. J.; Dufrene, Y. F. Atomic Force Microscopy as a Multifunctional Molecular Toolbox in Nanobiotechnology. *Nat. Nanotechnol.* **2008**, *3*, 261-269.

12. Craighead, H. G.; Mankiewich, P. M. Ultra-small Metal Particle Arrays Produced by High Resolution Electron-beam Lithography. *J. Appl. Phys.* **1982**, *53*, 7186-7188.

13. Bayati, M.; Patoka, P.; Giersig, M.; Savinova, E. R. An Approach to Fabrication of Metal Nanoring Arrays. *Langmuir* **2010**, *26*, 3549-3554.

14. Chen, J. X.; Liao, W. S.; Chen, X.; Yang, T. L.; Wark, S. E.; Son, D. H.; Batteas, J. D.; Cremer, P. S. Evaporation-Induced Assembly of Quantum Dots into Nanorings *ACS Nano* **2009**, *3*, 173-180.

15. Garno, J. C.; Amro, N. A.; Wadu-Mesthrige, K.; Liu, G.-Y. Production of Periodic Arrays of Protein Nanostructures Using Particle Lithography. *Langmuir* **2002**, *18*, 8186-8192.

16. Lusker, K. L.; Yu, J.-J.; Garno, J. C. Particle Lithography with Vapor Deposition of Organosilanes: A Molecular Toolkit for Studying Confined Surface Reactions in Nanoscale Liquid Volumes. *Thin Solid Films* **2011**, *519*, 5223-5229.

17. Shaheen, S. E.; Ginley, D. S.; Jabbour, G. E. Organic-based Photovoltaics. Toward Low-cost Power Generation. *Mater. Res. Bull.* **2005**, *30*, 10-19.

18. Oosterhout, S. D.; Wienk, M. M.; van Bavel, S. S.; Thiedmann, R.; Koster, L. J. A.; Gilot, J.; Loos, J.; Schmidt, V.; Janssen, R. A. J. The Effect of Three-dimensional Morphology on the Efficiency of Hybrid Polymer Solar Cells. *Nat. Mater.* **2009**, *8*, 818-824.

19. Peet, J.; Kim, J. Y.; Coates, N. E.; Ma, W. L.; Moses, D.; Heeger, A. J.; Bazan, G. C. Efficiency Enhancement in Low-bandgap Polymer Solar Cells by Processing with Alkane Dithiols. *Nat. Mater.* **2007**, *6*, 497-500.

20. Li, J.-R.; Garno, J. C. Indirect Modulation of Nonmagnetic Probes for Force Modulation Atomic Force Microscopy. *Anal. Chem.* **2009**, *81*, 1699-1706.

21. Binnig, G.; Quate, C. F.; Gerber, C. Atomic Force Microscope. *Phys. Rev. Lett.* **1986**, *56*, 930-933.

22. Hansma, P. K.; Elings, V. B.; Marti, O.; Bracker, C. E. Scanning Tunneling Microscopy and Atomic Force Microscopy - Application to Biology and Technology. *Science* **1988**, *242*, 209-216.

23. Zhong, C. J.; Maye, M. M. Core-shell Assembled Nanoparticles as Catalysts. *Adv. Mater.* **2001**, *13*, 1507-+.

24. Braun, G.; Lee, S. J.; Dante, M.; Nguyen, T. Q.; Moskovits, M.; Reich, N. Surface-enhanced Raman Spectroscopy for DNA Detection by Nanoparticle Assembly onto Smooth Metal Films. *J. Am. Chem. Soc.* **2007**, *129*, 6378-6379.

25. Granot, E.; Patolsky, F.; Willner, I. Electrochemical Assembly of a CdS Semiconductor Nanoparticle Monolayer on Surfaces: Structural Properties and Photoelectrochemical Applications. *J. Phys. Chem. B* **2004**, *108*, 5875-5881.

26. Kasas, S.; Thomson, N. H.; Smith, B. L.; Hansma, H. G.; Zhu, X. S.; Guthold, M.; Bustamante, C.; Kool, E. T.; Kashlev, M.; Hansma, P. K. Escherichia Coli RNA Polymerase Activity Observed Using Atomic Force Microscopy. *Biochemistry* **1997**, *36*, 461-468.

27. Karajanagi, S. S.; Vertegel, A. A.; Kane, R. S.; Dordick, J. S. Structure and Function of Enzymes Adsorbed onto Single-walled Carbon Nanotubes. *Langmuir* **2004**, *20*, 11594-11599.

28. Weisenhorn, A. L.; Drake, B.; Prater, C. B.; Gould, S. A. C.; Hansma, P. K.; Ohnesorge, F.; Egger, M.; Heyn, S. P.; Gaub, H. E. Immobilized Proteins in Buffer Imaged at Molecular Resolution by Atomic Force Microscopy. *Biophys. J.* **1990**, *58*, 1251-1258.

29. Pyun, J.; Kowalewski, T.; Matyjaszewski, K. Synthesis of Polymer Brushes using Atom Transfer Radical Polymerization. *Macromol. Rapid Commun.* **2003**, *24*, 1043-1059.

30. Domke, J.; Radmacher, M. Measuring the Elastic Properties of Thin Polymer Films with the Atomic Force Microscope. *Langmuir* **1998**, *14*, 3320-3325.

31. Bonnell, D. A.: *Scanning Probe Microscopy and Spectroscopy: Theory, Techniques, and Applications*; Wiley-VCH: New York, 2001.

32. Takano, H.; Kenseth, J. R.; Wong, S. S.; O'Brien, J. C.; Porter, M. D. Chemical and Biochemical Analysis using Scanning Force Microscopy. *Chem. Rev.* **1999**, *99*, 2845-2890.

33. Mate, C. M.; McClelland, G. M.; Erlandsson, R.; Chiang, S. Atomic-scale Friction of a Tungsten Tip on a Graphite Surface. *Phys. Rev. Lett.* **1987**, *59*, 1942-1945.

34. Markiewicz, P.; Goh, M. C. Atomic-Force Microscopy Probe Tip Visualization and Improvement of Images using a Simple Deconvolution Procedure. *Langmuir* **1994**, *10*, 5-7.

35. Villarrubia, J. S. Algorithms for Scanned Probe Microscope Image Simulation, Surface Reconstruction, and Tip Estimation. *J. Res. Natl. Inst. Stand.* **1997**, *102*, 425-454.

36. Williams, P. M.; Shakesheff, K. M.; Davies, M. C.; Jackson, D. E.; Roberts, C. J.; Tendler, S. J. B. Blind Reconstruction of Scanning Probe Image Data. *J. Vac. Sci. Technol. B* **1996**, *14*, 1557-1562.

37. Wilson, D. L.; Kump, K. S.; Eppell, S. J.; Marchant, R. E. Morphological Restoration of Atomic-force Microscopy Images. *Langmuir* **1995**, *11*, 265-272.

38. Fritz, M.; Radmacher, M.; Cleveland, J. P.; Allersma, M. W.; Stewart, R. J.; Gieselmann, R.; Janmey, P.; Schmidt, C. F.; Hansma, P. K. Imaging Globular and Filamentous Proteins in Physiological Buffer Solutions with Tapping Mode Atomic-force Microscopy. *Langmuir* **1995**, *11*, 3529-3535.

39. Moller, C.; Allen, M.; Elings, V.; Engel, A.; Muller, D. J. Tapping-mode Atomic Force Microscopy Produces Faithful High-resolution Images of Protein Surfaces. *Biophys. J.* **1999**, *77*, 1150-1158.

40. Thomann, Y.; Cantow, H. J.; Bar, G.; Whangbo, M. H. Investigation of Morphologies and Nanostructures of Polymer Blends by Tapping Mode Phase Imaging. *Appl. Phys. A: Mater. Sci. Process.* **1998**, *66*, S1233-S1236.

41. Raghavan, D.; Gu, X.; Nguyen, T.; VanLandingham, M.; Karim, A. Mapping Polymer Heterogeneity using Atomic Force Microscopy Phase Imaging and Nanoscale Indentation. *Macromolecules* **2000**, *33*, 2573-2583.

42. Tesfai, A.; El-Zahab, B.; Kelley, A. T.; Li, M.; Garno, J. C.; Baker, G. A.; Warner, I. M. Magnetic and Nonmagnetic Nanoparticles from a Group of Uniform Materials Based on Organic Salts. *ACS Nano* **2009**, *3*, 3244-3250.

43. Terrill, R. H.; Postlethwaite, T. A.; Chen, C. H.; Poon, C. D.; Terzis, A.; Chen, A. D.; Hutchison, J. E.; Clark, M. R.; Wignall, G.; Londono, J. D.; Superfine, R.; Falvo, M.; Johnson, C. S.; Samulski, E. T.; Murray, R. W. Monolayers in Three Dimensions: NMR, SAXS, Thermal, and Electron Hopping Studies of Alkanethiol Stabilized Gold Clusters. *J. Am. Chem. Soc.* **1995**, *117*, 12537-12548

44. Ibanez, F. J.; Gowrishetty, U.; Crain, M. M.; Walsh, K. M.; Zamborini, F. P. Chemiresistive Vapor Sensing with Microscale Films of Gold Monolayer Protected Clusters. *Anal. Chem.* **2006**, *78*, 753-761.

45. Gotsmann, B.; Seidel, C.; Anczykowski, B.; Fuchs, H. Conservative and Dissipative Tip-sample Interaction Forces Probed with Dynamic AFM. *Phys. Rev. B* **1999**, *60*, 11051-11061.

46. Tamayo, J.; Garcia, R. Deformation, Contact Time, and Phase Contrast in Tapping Mode Scanning Force Microscopy *Langmuir* **1996**, *12*, 4430-4435.

47. Sulchek, T.; Yaralioglu, G. G.; Quate, C. F.; Minne, S. C. Characterization and Optimization of Scan Speed for Tapping-mode Atomic Force Microscopy. *Rev. Sci. Instrum.* **2002**, *73*, 2928-2936.

48. Ogoshi, T.; Fujiwara, T.; Bertolucci, M.; Galli, G.; Chiellini, E.; Chujo, Y.; Wynne, K. J. Tapping Mode AFM Evidence for an Amorphous Reticular Phase in a Condensation-cured Hybrid Elastomer: Alpha,Omega-dihydroxypoly(dimethylsiloxane)/poly(diethonysiloxane)/fumed Silica Nanoparticles. *J. Am. Chem. Soc.* **2004**, *126*, 12284-12285.

49. Dong, R.; Yu, L. Y. E. Investigation of Surface Changes of Nanoparticles using TM-AFM Phase Imaging. *Environ. Sci. Technol.* **2003**, *37*, 2813-2819.

50. Aytun, T.; Mutaf, O. F.; El-Atwani, O. J.; Ow-Yang, C. W. Nanoscale Composition Mapping of Segregation in Micelles with Tapping-Mode Atomic Force Microscopy. *Langmuir* **2008**, *24*, 14183-14187.

51. Wozniak, M. J.; Ryszkowska, J.; Szymborski, T.; Chen, G.; Tateishi, T.; Kurzydlowski, K. J. Application of Phase Imaging and Force Modulation Mode for Description of Dispersion of Carbon Nanotubes in Polyol Matrix. *Mater. Sci. Poland* **2008**, *26*, 245-253.

52. Li, F. B.; Thompson, G. E.; Newman, R. C. Force Modulation Atomic Force Microscopy: Background, Development and Application to Electrodeposited Cerium Oxide Films. *Appl. Surf. Sci.* **1998**, *126*, 21-33.

53. Maivald, P.; Butt, H. J.; Gould, S. A. C.; Prater, C. B.; Drake, B.; Gurley, J. A.; Elings, V. B.; Hansma, P. K. Using Force Modulation to Image Surface Elasticities with the Atomic Force Microscope. *Nanotech.* **1991**, *2*, 103-106.

54. Carpick, R. W.; Ogletree, D. F.; Salmeron, M. Lateral Stiffness: A New Nanomechanical Measurement for the Determination of Shear Strengths with Friction Force Microscopy. *Appl. Phys. Lett.* **1997**, *70*, 1548-1550.

55. Bar, G.; Rubin, S.; Parikh, A. N.; Swanson, B. I.; Zawodzinski, T. A.; Whangbo, M. H. Scanning Force Microscopy Study of Patterned Monolayers of Alkanethiols on Gold. Importance of Tip-Sample Contact Area in Interpreting Force Modulation and Friction Force Microscopy Images. *Langmuir* **1997**, *13*, 373-377.

56. Overney, R. M.; Meyer, E.; Frommer, J.; Guntherodt, H. J.; Fujihira, M.; Takano, H.; Gotoh, Y. Force Microscopy Study of Friction and Elastic Compliance of Phase-Separated Organic Thin Films. *Langmuir* **1994**, *10*, 1281-1286.

57. DeVecchio, D.; Bhushan, B. Localized Surface Elasticity Measurements Using an Atomic Force Microscope. *Rev. Sci. Instrum.* **1997**, *68*, 4498-4505.

58. Radmacher, M.; Tilmann, R. W.; Gaub, H. E. Imaging Viscoelasticity by Force Modulation with the Atomic Force Microscope. *Biophys. J.* **1993**, *64*, 735-742.

59. Florin, E. L.; Radmacher, M.; Fleck, B.; Gaub, H. E. Atomic Force Microscope with Magnetic Force Modulation. *Rev. Sci. Instrum.* **1994**, *65*, 639-643.

60. Mornet, S.; Bre´tagnol, F.; Ilaria Mannelli; Valsesia, A.; Sirghi, L.; Colpo, P.; Rossi, F. Large-Scale Fabrication of Bi-Functional Nanostructured Polymer Surfaces for Selective Biomolecular Adhesion. *Small* **2008**, *4*, 1919-1924.

61. Trujillo, N. J.; Baxamusa, S. H.; Gleason, K. K. Grafted Functional Polymer Nanostructures Patterned Bottom-Up by Colloidal Lithography and Initiated Chemical Vapor Deposition (iCVD). *Chem. Mater.* **2009**, *21*, 742-750.

62. Sun, Z.; Li, Y.; Zhang, J.; Li, Y.; Zhao, Z.; Zhang, K.; Zhang, G.; Guo, J.; Yang, B. A Universal Approach to Fabricate Various Nanoring Arrays Based on a Colloidal-Crystal-Assisted-Lithography Strategy. *Adv. Funct. Mater.* **2008**, *18*, 4036-4042.

63. Abdelsalam, M. E.; Bartlett, P. N.; Baumberg, J. J.; Coyle, S. Preparation of Arrays of Isolated Spherical Cavities by Self-Assembly of Polystyrene Spheres on Self-Assembled Pre-Patterned Macroporous Films. *Adv. Mater.* **2004**, *16*, 90-903.

64. Wang, W.; Dai, Z.; Sun, Y.; Sun, Y. Enhancement of Optical Nonlinearity in Binary Metal–Nanoparticle Arrays. *Thin Solid Films* **2009**, *517*, 6050-6053.

65. Zhou, C. M.; Gall, D. Surface Patterning by Nanosphere Lithography for Layer Growth with Ordered Pores. *Thin Solid Films* **2007**, *516*, 433-437.

66. Jeong, J.-R.; Kim, S.; Kim, S.-H.; Bland, J. A. C.; Shin, S.-C.; Yang, S.-M. Fabrication of Hexagonal Lattice Co/Pd Multilayer Nanodot Arrays Using Colloidal Lithography. *Small* **2007**, *3*, 1529-1533.

67. Kosiorek, A.; Kandulski, W.; Glaczynska, H.; Giersig, M. Fabrication of Nanoscale Rings, Dots, and Rods by Combining Shadow Nanosphere Lithography and Annealed Polystyrene Nanosphere Masks. *Small* **2005**, *1*, 439-444.

68. Chen, X.; Chen, Z.; Fu, N.; Lu, G.; Yang, B. Versatile Nanopatterned Surfaces Generated via Three-Dimensional Colloidal Crystals. *Adv. Mater.* **2003**, *15*, 1413-1417.

69. Bae, C.; Shin, H.; Moon, J.; Sung, M. M. Contact Area Lithography (CAL): A New Approach to Direct Formation of Nanometric Chemical Patterns. *Chem. Mater.* **2006**, *18*, 1085-1088.

70. McLellan, J. M.; Geissler, M.; Xia, Y. Edge Spreading Lithography and Its Application to the Fabrication of Mesoscopic Gold and Silver Rings. *J. Am. Chem. Soc.* **2004**, *126*, 10830-10831.

71. Li, J. R.; Garno, J. C. Elucidating the Role of Surface Hydrolysis in Preparing Organosilane Nanostructures via Particle Lithography. *Nano Lett* **2008**, *8*, 1916-1922.

72. Li, J. R.; Lusker, K. L.; Yu, J. J.; Garno, J. C. Engineering the Spatial Selectivity of Surfaces at the Nanoscale Using Particle Lithography Combined with Vapor Deposition of Organosilanes. *ACS Nano* **2009**, *3*, 2023-2035.

73. Li, J.-R.; Garno, J. C. Nanostructures of Octadecyltrisiloxane Self-Assembled Monolayers Produced on Au(111) Using Particle Lithography. *ACS Appl. Mater. Interfaces* **2009**, *1*, 969-976.

74. Rybczynski, J.; Ebels, U.; Giersig, M. Large-scale, 2D Arrays of Magnetic Nanoparticles. *Colloids Surf., A* **2003**, *219*, 1-6.

75. Lewandowski, B. R.; Kelley, A. T.; Singleton, R.; Li, J.-R.; Lowry, M.; Warner, I. M.; Garno, J. C. Nanostructures of Cysteine-Coated CdS Nanoparticles Produced with "Two-Particle" Lithography. *J. Phys. Chem. C* **2009**, *113*, 5933-5940.

76. Li, J.-R.; Henry, G. C.; Garno, J. C. Fabrication of Nanopatterned Films of Bovine Serum Albumin and Staphylococcal Protein A using Latex Particle Lithography. *Analyst* **2006**, *131*, 244-250.

77. Cai, Y.; Ocko, B. M. Large-Scale Fabrication of Protein Nanoarrays Based on Nanosphere Lithography. *Langmuir* **2005**, *21*, 9274-9279.

78. Deckman, H. W.; Dunsmuir, J. H. Natural Lithography. *Appl. Phys. Lett.* **1982**, *41*, 377-379.

79. Denis, F. A.; Hanarp, P.; Sutherland, D. S.; Gold, J.; Mustin, C.; Rouxhet, P. G.; Dufrene, Y. F. Protein Adsorption on Model Surfaces with Controlled Nanotopography and Chemistry. *Langmuir* **2002**, *18*, 819-828.

80. Hulteen, J. C.; Van Duyne, R. P. Nanosphere Lithography: A Materials General Fabrication Process for Periodic Particle Array Surfaces. *J. Vac. Sci. Technol. A* **1995**, *13*, 1553-1558.

81. Lipson, A. L.; Comstock, D. J.; Hersam, M. C. Nanoporous Templates and Membranes Formed by Nanosphere Lithography and Aluminum Anodization. *Small* **2009**, *5*, 2807-2811.

82. Jiang, P.; McFarland, M. J. Large-Scale Fabrication of Wafer-Size Colloidal Crystals, Macroporous Polymers and Nanocomposites by Spin-Coating. *J. Am. Chem. Soc.* **2004**, *126*, 13778-13786.

83. Jiang, P.; Prasad, T.; McFarland, M. J.; Colvin, V. L. Two-dimensional Nonclose-packed Colloidal Crystals Formed by Spincoating. *Appl. Phys. Lett.* **2006**, *89*, 011908.

84. Kondo, M.; Shinozaki, K.; Bergstrom, L.; Mizutani, N. Preparation of Colloidal Monolayers of Alkoxylated Silica Particles at the Air-liquide Interface. *Langmuir* **1995**, *11*, 394-397.

85. Hayward, R. C.; Saville, D. A.; Aksay, I. A. Electrophoretic Assembly of Colloidal Crystals with Optically Tunable Micropatterns. *Nature* **2000**, *404*, 56-59.

86. Trau, M.; Saville, D. A.; Aksay, I. A. Field-induced Layering of Colloidal Crystals. *Science* **1996**, *272*, 706-709.

87. Yang, S.-M.; Jang, S. G.; Choi, D.-G.; Kim, S.; Yu, H. K. Nanomachining by Colloidal Lithography. *Small* **2006**, *2*, 458-475.

88. Plettl, A.; Enderle, F.; Saitner, M.; Manzke, A.; Pfahler, C.; Wiedemann, S.; Ziemann, P. Non-Close-Packed Crystals from Self-Assembled Polystyrene Spheres by Isotropic Plasma Etching: Adding Flexibility to Colloid Lithography. *Adv. Funct. Mater.* **2009**, *19*, 3279-3284.

89. Haginoya, C.; Ishibashi, M.; Koike, K. Nanostructure Array Fabrication with a Size-Controllable Natural Lithography. *Appl. Phys. Lett.* **1997**, *71*, 2934-2936.

90. Li, Y.; Lee, E. J.; Cai, W.; Kim, K. Y.; Cho, S. O. Unconventional Method for Morphology-controlled Carbonaceous Nanoarrays Based on Electron Irradiation of a Polystyrene Colloidal Monolayer. *ACS Nano* **2008**, *2*, 1108-1112.

91. Geissler, M.; McLellan, J. M.; Chen, J.; Xia, Y. Side-by-Side Patterning of Multiple Alkanethiolate Monolayers on Gold by Edge-Spreading Lithography. *Angew. Chem. Int. Ed.* **2005**, *44*, 3596 –3600.

92. Li, Y.; Fang, X. S.; Koshizaki, N.; Sasaki, T.; Li, L.; Gao, S. Y.; Shimizu, Y.; Bando, Y.; Golberg, D. Periodic TiO(2) Nanorod Arrays with Hexagonal Nonclose-Packed Arrangements: Excellent Field Emitters by Parameter Optimization. *Adv. Funct. Mater.* **2009**, *19*, 2467-2473.

93. Xu, D. W.; Graugnard, E.; King, J. S.; Zhong, L. W.; Summers, C. J. Large-scale Fabrication of Ordered Nanobowl Arrays. *Nano Lett.* **2004**, *4*, 2223-2226.

94. Kuo, C.-W.; Shiu, J.-Y.; Chen, P.; Somorjai, G. A. Fabrication of Size-Tunable Large-Area Periodic Silicon Nanopillar Arrays with Sub-10-nm Resolution. *J. Phys. Chem. B* **2003**, *107*, 9950-9953.

95. Byrne, D.; Schilling, A.; Scott, J. F.; Gregg, J. M. Ordered Arrays of Lead Zirconium Titanate Nanorings. *Nanotechnology* **2008**, *19*, 165608.

96. McLellan, J. M.; Geissler, M.; Xia, Y. Self-assembly of Hexadecanethiol Molecules on Gold from the Vapour Phase as Directed by a Two-dimensional Array of Silica Beads. *Chem. Phys. Lett.* **2005**, *408*, 80-83.

97. Taylor, Z. R.; Patel, K.; Spain, T. G.; Keay, J. C.; Jernigen, J. D.; Sanchez, E. S.; Grady, B. P.; Johnson, M. B.; Schmidtke, D. W. Fabrication of Protein Dot Arrays via Particle Lithography. *Langmuir* **2009**, *25*, 10932-10938.

98. Marquez, M.; Patel, K.; Carswell, A. D. W.; Schmidtke, D. W.; Grady, B. P. Synthesis of Nanometer-Scale Polymeric Structures on Surfaces from Template Assisted Admicellar Polymerization: A Comparative Study with Protein Adsorption. *Langmuir* **2006**, *22*, 8010-8016.

99. Kim, H.; Park, J. H.; Cho, I.-H.; Kim, S.-K.; Paek, S.-H.; Lee, H. Selective Immobilization of Proteins on Gold Dot Arrays and Characterization using Chemical Force Microscopy. *J. Colloid Interface Sci.* **2009**, *334*, 161-166.

100. Kumar, A.; Biebuyck, H. A.; Whitesides, G. M. Patterning Self-assembled Monolayers - Applications in Materials Science. *Langmuir* **1994**, *10*, 1498-1511.

101. Geissler, M.; McLellan, J. M.; Xia, Y. Edge-Spreading Lithography: Use of Patterned Photoresist Structures to Direct the Spreading of Alkanethiols on Gold. *Nano Lett.* **2005**, *5*, 31-36.

102. Ulman, A. Formation and Structure of Self-Assembled Monolayers. *Chem. Rev.* **1996**, *96*, 1533-1554.

103. Zhang, X.; Whitney, A. V.; Zhao, J.; Hicks, E. M.; Duyne, R. P. V. Advances in Contemporary Nanosphere Lithographic Techniques. *J. Nanosci. Nanotechnol.* **2006**, *6*, 1-15.

104. Zhang, J.; Li, Y.; Zhang, X.; Yang, B. Colloidal Self-Assembly Meets Nanofabrication: From Two-Dimensional Colloidal Crystals to Nanostructure Arrays *Adv. Mater.* **2010**, *22*, 4249-4269.

105. Li, Y.; Koshizaki, N.; Cai, W. Periodic One-dimensional Nanostructured Arrays Based on Colloidal Templates, Applications, and Devices. *Coord. Chem. Rev.* **2011**, *255*, 357-373.

106. Aizpurua, J.; Hanarp, P.; Sutherland, D. S.; Kall, M.; Bryant, G. W.; de Abajo, F. J. G. Optical Properties of Gold Nanorings. *Phys. Rev. Lett.* **2003**, *90*.

107. Bergveld, P. The Future of Biosensors. *Sens. Actuator A-Phys.* **1996**, *56*, 65-73.

108. Templin, M. F.; Stoll, D.; Schwenk, J. M.; Potz, O.; Kramer, S.; Joos, T. O. Protein Microarrays: Promising Tools for Proteomic Research. *Proteomics* **2003**, *3*, 2155-2166.

109. Walt, D. R. Miniature Analytical Methods for Medical Diagnostics. *Science* **2005**, *308*, 217-219.

110. Ngunjiri, J. N.; Daniels, S. L.; Li, J.-R.; Serem, W. K.; Garno, J. C. Controlling the Surface Coverage and Arrangement of Proteins using Particle Lithography. *Nanomedicine* **2008**, *3*, 529-541.

111. Daniels, S. L.; Ngunjiri, J. N.; Garno, J. C. Investigation of the Magnetic Properties of Ferritin by AFM Imaging with Magnetic Sample Modulation. *Anal. Bioanal. Chem.* **2009**, *394*, 215-223.

112. Sagiv, J. Organized Monolayers by Adsorption, I . Formation and Structure of Oleophobic Mixed Monolayers on Solid Surfaces. *J. Am. Chem. Soc.* **1980**, *102*, 92-98.

113. Netzer, L.; Sagiv, J. A New Approach to Construction of Artificial Monolayer Assemblies. *J. Am. Chem. Soc.* **1983**, *105*, 674-676.

114. Kim, J.-H.; Cotton, T. M.; Uphaus, R. A. Electrochemical and Raman Characterization of Molecular Recognition Sites in Self-Assembled Monolayers. *J. Phys. Chem.* **1988**, *92*, 5575-5578.

115. Schreiber, F. Structure and Growth of Self-Assembling Monolayers. *Prog. Surf. Sci.* **2000**, *65*, 151-256.

116. Vuillaume, D.; Boulas, C.; Collet, J.; Allan, G.; Delerue, C. Electronic Structure of a Heterostructure of an Alkylsiloxane Self-Assembled Monolayer on Silicon. *Phys. Rev. B* **1998**, *58*, 16491-16498

117. Xiao, X.; Hu, J.; Charych, D. H.; Salmeron, M. Chain Length Dependence of the Frictional Properties of Alkylsilane Molecules Self-Assembled on Mica Studied by Atomic Force Microscopy. *Langmuir* **1996**, *12*, 235-237.

118. Angst, D. L.; Simmons, G. W. Moisture Absorption Characteristics of Organosiloxane Self-Assembled Monolayers. *Langmuir* **1991**, *7*, 2236-2242.

119. Woodson, M.; Liu, J. Functional Nanostructures from Surface Chemistry Patterning. *Phys. Chem. Chem. Phys.* **2007**, *9*, 207-225.

120. Wen, K.; Maoz, R.; Cohen, H.; Sagiv, J.; Gibaud, A.; Desert, A.; Ocko, B. M. Postassembly Chemical Modification of a Highly Ordered Organosilane Multilayer: New Insights into the Structure, Bonding, and Dynamics of Self-Assembling Silane Monolayers. *ACS Nano* **2008**, *2*, 579-599.

121. Maoz, R.; Sagiv, J. On the Formation and Structure of Self-Assembling Monolayers I. A Comparative ATR-Wettability Study of Langmuir-Blodgett and Adsorbed Films on Flat Substrates and Glass Microbeads. *J. Colloid Interface Sci.* **1984**, *100*, 465-496.

122. Allara, D. L.; Parikh, A. N.; Rondelez, F. Evidence for a Unique Chain Organization in Long Chain Silane Monolayers Deposited on Two Widely Different Solid Substrates. *Langmuir* **1995**, *11*, 2357-2360.

123. Hozumi, A.; Yokogawa, Y.; Kameyama, T. Amino-Terminated Self-Assembled Monolayer on a SiO2 Surface Formed by Chemical Vapor Deposition. *J. Vac. Sci. Technol., A* **2001**, *19*, 1812-1816.

124. Dong, J.; Wang, A.; Ng, K. Y. S.; Mao, G. Self-Assembly of Octadecyltrichlorosilane Monolayers on Silicon-Based Substrates by Chemical Vapor Deposition. *Thin Solid Films* **2006**, *515*, 2116-2122.

125. McGovern, M. E.; Kallury, K. M. R.; Thompson, M. Role of Solvent on the Silanization of Glass with Octadecyltrichlorosilane. *Langmuir* **1994**, *10*, 3607-3614.

126. Tripp, C. P.; Hair, M. L. Direct Observation of the Surface Bonds between Self-Assembled Monolayers of Octadecyltrichlorosilane and Silica Surfaces: A Low-Frequency IR Study at the Solid/Liquid Interface. *Langmuir* **1995**, *11*, 1215-1219.

127. Brzoska, J. B.; Shahidzadeh, N.; Rondelez, F. Evidence of a Transition Temperature for the Optimum Deposition of Grafted Monolayer Coatings. *Nature* **1992**, *360*, 719-721.

128. Parikh, A. N.; Allara, D. L.; Azouz, I. B.; Rondelez, F. An Intrinsic Relationship between Molecular Structure in Self-Assembled n-Alkylsiloxane Monolayers and Deposition Temperature. *J. Phys. Chem.* **1994**, *98*, 7577-7590.

129. Foisner, J.; Glaser, A.; Kattner, J.; Hoffmann, H.; Friedbacher, G. Atomic Force Microscopy Investigation of the Growth of Different Alkylsiloxane Monolayers from Highly Concentrated Solutions. *Langmuir* **2003**, *19*, 3741-3746.

130. Tillman, N.; Ulman, A.; Schildkraut, J. S.; Penner, T. L. Incorporation of Phenoxy Groups in Self-Assembled Monolayers of Trichlorosilane Derivatives: Effects on Film Thickness, Wettability, and Molecular Orientation. *J. Am. Chem. Soc.* **1988**, *110*, 6136-6144.

131. Tripp, C. P.; Hair, M. L. An Infrared Study of the Reaction of Octadecyltrichlorosilane with Silica. *Langmuir* **1992**, *8*, 1120-1126.

132. St. John, P. M.; Craighead, H. G. Microcontact Printing and Pattern Transfer using Trichlorosilanes on Oxide Substrates. *Appl. Phys. Lett.* **1996**, *68*, 1022-1024.

133. Wang, D.; Thomas, S. G.; Wang, K. L.; Xia, Y.; Whitesides, G. M. Nanometer Scale Patterning and Pattern Transfer on Amorphous Si, Crystalline Si, and SiO2 Surfaces using Self-Assembled Monolayers. *Appl. Phys. Lett.* **1997**, *70*, 1593-1595.

134. Xue, C.-Y.; Yang, K.-L. One-Step UV Lithography for Activation of Inert Hydrocarbon Monolayers and Preparation of Protein Micropatterns. *J. Colloid Interface Sci.* **2010**, *344*, 48-53.

135. Lercel, M. J.; Craighead, H. G.; Parikh, A. N.; Seshadri, K.; Allara, D. L. Sub-10 nm Lithography with Self-Assembled Monolayers. *Appl. Phys. Lett.* **1996**, *68*, 1504-1506.

136. Lercel, M. J.; Redinbo, G. F.; Pardo, F. D.; Rooks, M.; Tiberio, R. C.; Simpson, P.; Craighead, H. G. Electron Beam Lithography with Monolayers of Alkylthiols and Alkylsiloxanes. *J. Vac. Sci. Technol., B* **1994**, *12*, 3663-3667.

137. Jung, H. K., R.; Collier, C. P. Dip-Pen Nanolithography of Reactive Alkoxysilanes on Glass. *J. Am. Chem. Soc.* **2003**, *125*, 12096-12097.

138. Gu, J. H. Y., C. M.; Li, S.; Cai, C. Z. Nanometric Protein Arrays on Protein-Resistant Monolayers on Silicon Surfaces. *J. Am. Chem. Soc.* **2004**, *126*, 8098-8099.

139. Headrick, J. E.; Armstrong, M.; Cratty, J.; Hammond, S.; Sheriff, B. A.; Berrie, C. L. Nanoscale Patterning of Alkyl Monolayers on Silicon Using the Atomic Force Microscope. *Langmuir* **2005**, *21*, 4117-4122.

140. Klapetek, P. N. D.: http://gwyddion.net/. 2007.

141. Wilcox, C. D.; Dove, S. B.; McDavid, W. D.; Greer, D. B.: http://ddsdx.uthscsa.edu. 2009.

142. Vallant, T.; Brunner, H.; Mayer, U.; Hoffmann, H.; Leitner, T.; Resch, R.; Friedbacher, G. Formation of Self-Assembled Octadecylsiloxane Monolayers on Mica and Silicon Surfaces Studied by Atomic Force Microscopy and Infrared Spectroscopy. *J. Phys. Chem. B* **1998**, *102*, 7190-7197.

143. Jeon, N. L.; Finnie, K.; Branshaw, K.; Nuzzo, R. G. Structure and Stability of Patterned Self-Assembled Films of Octadecyltrichlorosilane Formed by Contact Printing. *Langmuir* **1997**, *13*, 3382-3391.

144. Wasserman, S. R.; Tao, Y.-T.; Whitesides, G. M. Structure and Reactivity of Alkylsiloxane Monolayers Formed by Reaction of Alkyltrichlorosilanes on Silicon Substrates. *Langmuir* **1989**, *5*, 1074-1087.

145. Thirtle, P. N.; Li, Z. X.; Thomas, R. K. Structure of Nonionic Surfactant Layers Adsorbed at the Solid/Liquid Interface on Self-Assembled Monolayers with Different Surface Functionality: A Neutron Reflection Study. *Langmuir* **1997**, *13*, 5451-5458.

146. Papra, A.; Gadegaard, N.; Larsen, N. B. Characterization of Ultrathin Poly(ethylene glycol) Monolayers on Silicon Substrates. *Langmuir* **2001**, *17*, 1457-1460.

147. Trens, P.; Denoyel, R. Adsorption of (ç-Aminopropyl)triethoxysilane and Related Molecules at the Silica/Heptane Interface. *Langmuir* **1996**, *12*, 2781-2784.

148. Krasnoslobodtsev , A. V.; Smirnov, S. N. Effect of Water on Silanization of Silica by Trimethoxysilanes. *Langmuir* **2002**, *18*, 3181-3184.

149. Vandenberg, E. T.; Bertilsson, L.; Liedberg, B.; Uvdal, K.; Erlandsson, R.; Elwing, H.; Lundstrom, I. Structure of 3-Aminopropyl Triethoxy Silane on Silicon Oxide. *J. Colloid Interface Sci.* **1991**, *147*, 103-118.

150. Carson, G. A.; Granick, S. Self-assembly of Octadecyltrichlorosilane Monolayers on Mica. *J. Mater. Res.* **1990**, *5*, 1745-1751.

151. Rye, R. R.; Nelson, G. C.; Dugger, M. T. Mechanistic Aspects of Alkylchlorosilane Coupling Reactions. *Langmuir* **1997**, *13*, 2965-2972.

152. Haynes, C. L.; Van Duyne, R. P. Nanosphere Lithography: A Versatile Nanofabrication Tool for Studies of Size-Dependent Nanoparticle Optics. *J. Phys. Chem. B* **2001**, *105*, 5599-5611.

153. Hoa, M. L. K.; Lu, M.; Zhang, Y. Preparation of Porous Materials with Ordered Hole Structure. *Adv. Colloid Interface Sci.* **2006**, *121*, 9-23.

154. Kim, E.; Xia, Y.; Whitesides, G. M. Two- and Three-Dimensional Crystallization of Polymeric Microspheres by Micromolding in Capillaries. *Adv. Mater.* **1996**, *8*, 245-247.

155. Gates, B.; Qin, D.; Xia, Y. Assembly of Nanoparticles into Opaline Structures over Large Areas. *Adv. Mater.* **1999**, *11*, 466-469.

156. Shenhar, R.; Rotello, V. M. Nanoparticles: Scaffolds and Building Blocks. *Accounts Chem. Res.* **2003**, *36*, 549-561.

157. Maxwell, D. J.; Taylor, J. R.; Nie, S. Self-Assembled Nanoparticle Probes for Recognition and Detection of Biomolecules. *J. Am. Chem. Soc.* **2002**, *124*, 9606-9612.

158. Caruso, F. Nanoengineering of Particle Surfaces. *Adv. Mater.* **2001**, *13*, 11-22.

159. Templeton, A. C.; Wuelfing, W. P.; W.Murray, R. Monolayer-Protected Cluster Molecules. *Accounts Chem. Res.* **2000**, *33*, 27-36.

160. Li, X.-M.; Huskens, J.; Reinhoudt, D. N. Reactive Self-Assembled Monolayers on Flat and Nanoparticle Surfaces, and their Application in Soft and Scanning Probe Lithographic Nanofabrication Technologies. *J. Mater. Chem.* **2004**, *14*, 2954-2971.

161. Wang, Y.; Han, S.; Briseno, A. L.; Sanedrin, R. J. G.; Zhou, F. A Modified Nanosphere Lithography for the Fabrication of Aminosilane/Polystyrene Nanoring Arrays and the Subsequent Attachment of Gold or DNA-Capped Gold Nanoparticles. *J. Mater. Chem.* **2004**, *14*, 3488-3494.

162. Serem, W. K.; Lusker, K. L.; Garno, J. C.: In *Encyclopedia of Analytical Chemistry, Supplementary*; Meyers, R. A., Ed.; John Wiley and Sons, Ltd.: Chichester, UK, 2011; pp 859-894.

163. Zamborini, F. P.; Smart, L. E.; Leopold, M. C.; Murray, R. W. Distance-Dependent Electron Hopping Conductivity and Nanoscale Lithography of Chemically-Linked Gold Monolayer Protected Cluster Films. *Anal. Chim. Acta.* **2003**, *496*, 3-16.

164. Wyrwa, D.; Beyer, N.; Schmid, G. One-Dimensional Arrangements of Metal Nanoclusters. *Nano Lett.* **2002**, *2*, 419-421.

165. Andres, R. P.; Bielefeld, J. D.; Henderson, J. I.; Janes, D. B.; Kolagunta, V.; Kubiak, C. P.; Mahoney, W. J.; Osifchin, R. G. Self-Assembly of a Two-Dimensional Superlattice of Molecularly Linked Metal Clusters. *Science* **1996**, *273*, 1690-1693.

166. Werts, M. H. V.; Lambert, M.; Bourgoin, J.-P.; Brust, M. Nanometer Scale Patterning of Langmuir-Blodgett Films of Gold Nanoparticles by Electron Beam Lithography. *Nano Lett.* **2002**, *2*, 43-47.

167. Li, X.-M.; Paraschiv, V.; Huskens, J.; Reinhoudt, D. N. Sulfonic Acid-Functionalized Gold Nanoparticles: A Colloid-Bound Catalyst for Soft Lithographic Application on Self-Assembled Monolayers. *J. Am. Chem. Soc.* **2003**, *125*, 4279-4284.

168. Yang, W.; Chen, M.; Knoll, W.; Deng, H. Synthesis of Hexanedithiolate/Decanethiolate Mixed Monolayer Protected Gold Clusters and Scanning Tunneling Microscope Tip Induced Patterning on the Clusters/Au(111) Surface. *Langmuir* **2002**, *18*, 4124-4130.

169. Liu, X.; Fu, L.; Hong, S.; Dravid, V. P.; Mirkin, C. A. Arrays of Magnetic Nanoparticles Patterned via "Dip-Pen" Nanolithography. *Adv. Mater.* **2002**, *14*, 231-234.

170. Garno, J. C.; Yang, Y.; Amro, N. A.; Cruchon-Dupeyrat, S.; Chen, S.; Liu, G.-Y. Precise Positioning of Nanoparticles on Surfaces Using Scanning Probe Lithography. *Nano Lett.* **2003**, *3*, 389-395.

171. Basnar, B.; Willner, I. Dip-Pen-Nanolithographic Patterning of Metallic, Semiconductor, and Metal Oxide Nanostructures on Surfaces. *Small* **2009**, *5*, 28-44.

172. Daniel, M.-C.; Astruc, D. Gold Nanoparticles: Assembly, Supramolecular Chemistry, Quantum-Size-Related Properties, and Applications toward Biology, Catalysis, and Nanotechnology. *Chem. Rev.* **2004**, *104*, 293-346.

173. Taton, T. A.; Mirkin, C. A.; Letsinger, R. L. Scanometric DNA Array Detection with Nanoparticle Probes. *Science* **2000**, *289*, 1757-1760.

174. Hostetler, M. J.; Stokes, J. J.; Murray, R. W. Infrared Spectroscopy of Three-Dimensional Self-Assembled Monolayers: N-Alkanethiolate Monolayers on Gold Cluster Compounds. *Langmuir* **1996**, *12*, 3604-3612

175. Hostetler, M. J.; Wingate, J. E.; Zhong, C. J.; Harris, J. E.; Vachet, R. W.; Clark, M. R.; Londono, J. D.; Green, S. J.; Stokes, J. J.; Wignall, G. D.; Glish, G. L.; Porter, M. D.; Evans, N. D.; Murray, R. W. Alkanethiolate Gold Cluster Molecules with Core Diameters from 1.5 to 5.2 nm: Core and Monolayer Properties as a Function of Core Size. *Langmuir* **1998**, *14*, 17-30.

176. Link, S.; El-Sayed, M. A. Shape and Size Dependence of Radiative, Non-Radiative and Photothermal Properties of Gold Nanocrystals. *Int. Rev. Phys. Chem.* **2000**, *19*, 409-453.

177. Eustis, S.; El-Sayed, M. A. Why Gold Nanoparticles are More Precious than Pretty Gold: Noble Metal Surface Plasmon Resonance and its Enhancement of the Radiative and Nonradiative Properties of Nanocrystals of Different Shapes. *Chem. Soc. Rev.* **2006**, *35*, 209-217.

178. Schaaff, T. G.; Shafigullin, M. N.; Khoury, J. T.; Vezmar, I.; Whetten, R. L.; Cullen, W. G.; First, P. N.; GutierrezWing, C.; Ascensio, J.; JoseYacaman, M. J. Isolation of Smaller Nanocrystal Au Molecules: Robust Quantum Effects in Optical Spectra. *J. Phys. Chem. B* **1997**, *101*, 7885-7891.

179. Menard, L. D.; Gao, S.-P.; Xu, H.; Twesten, R. D.; Harper, A. S.; Song, Y.; Wang, G.; Douglas, A. D.; Yang, J. C.; Frenkel, A. I.; Nuzzo, R. G.; Murray, R. W. Sub-Nanometer Au Monolayer-Protected Clusters Exhibiting Molecule-Like Electronic Behavior: Quantitative High-Angle Annular Dark-Field Scanning Transmission Electron Microscopy and Electrochemical Characterization of Clusters with Precise Atomic Stoichiometry. *J. Phys. Chem. B* **2006**, *110*, 12874-12883.

180. Wilbur, J. L.; Kumar, A.; Kim, E.; Whitesides, G. M. Microfabrication by Microcontact Printing of Self-Assembled Monolayers. *Adv. Mater.* **1994**, *6*, 600-604.

181. Mrksich, M.; Whitesides, G. M. Patterning Self-assembled Monolayers using Microcontact Printing - A New Technology for Biosensors. *Trends Biotechnol.* **1995**, *13*, 228-235.

182. Jackman, R. J.; Wilbur, J. L.; Whitesides, G. M. Fabrication of Submicrometer Features on Curved Substrates by Microcontact Printing. *Science* **1995**, *269*, 664-666.

183. Krebs, F. C. Roll-to-Roll Fabrication of Monolithic Large-Area Polymer Solar Cells Free from Indium-Tin-Oxide. *Sol. Energy Mater. Sol. Cells* **2009**, *93*, 1636-1641.

184. Galagan, Y.; de Vries, I. G.; Langen, A. P.; Andriessen, R.; Verhees, W. J. H.; Veenstra, S. C.; Kroon, J. M. Technology Development for Roll-to-Roll Production of Organic Photovoltaics. *Chem. Eng. Process.* **2011**, *50*, 454-461.

185. Liang, Y. Y.; Xu, Z.; Xia, J. B.; Tsai, S. T.; Wu, Y.; Li, G.; Ray, C.; Yu, L. P. For the Bright Future-Bulk Heterojunction Polymer Solar Cells with Power Conversion Efficiency of 7.4%. *Adv. Mater.* **2010**, *22*, E135.

186. Brabec, C. J.; Gowrisanker, S.; Halls, J. J. M.; Laird, D.; Jia, S. J.; Williams, S. P. Polymer-Fullerene Bulk-Heterojunction Solar Cells. *Adv. Mater.* **2010**, *22*, 3839-3856.

187. Chan, M. M.-Y.; Tao, C.-H.; Yam, V. W.-W.: WOLEDs and Organic Photovoltaics Recent Advances and Applications. In *Green Energy and Technology*; Yam, V. W. W., Ed.; Springer: Berlin Heidelberg, 2010.

188. Chidichimo, G.; Filippelli, L. Organic Solar Cells: Problems and Perspectives. *International Journal of Photoenergy* **2010**.

189. Rosa, L. G.; Liang, J. Atomic Force Microscope Nanolithography: Dip-pen, Nanoshaving, Nanografting, Tapping Mode, Electrochemical and Thermal Nanolithography. *J. Phys.: Condens. Matter* **2009**, *21*, 1-18.

190. Liu, G. Y.; Salmeron, M. Reversible Displacement of Chemisorbed n-Alkanethiol Molecules on Au (111) Surface:An Atomic Force Microscopy Study. *Langmuir* **1994**, *10*, 367-370.

191. Rosa, L. G.; Jiang, J.; Lima, O. V.; Xiao, J.; Utreras, E.; Dowben, P. A.; Tan, L. Selective Nanoshaving of Self-assembled Monolayers of 2-(4-pyridylethyl)triethoxysilane. *Mater. Lett.* **2009**, *63*, 961-964.

192. Brower, T. L.; Garno, J. C.; Ulman, A.; Liu, G.-Y.; Yan, C.; Golzhauser, A.; Grunze, M. Self-Assembled Multilayers of 4,4'-Dimercaptobiphenyl Formed by Cu(II) Oxidation. *Langmuir* **2002**, *18*, 6207-6216.

193. Chwang, A. B.; Granstrom, E. L.; Frisbie, C. D. Fabrication of a Sexithiophene Semiconducting Wire: Nanoshaving with an Atomic Force Microscope Tip. *Adv. Mater.* **2000**, *12*, 285-288.

194. Milic, T.; Garno, J. C.; Batteas, J. D.; Smeureanu, G.; Drain, C. M. Self-organization of Self-assembled Tetrameric Porphyrin Arrays on Surfaces. *Langmuir* **2004**, *20*, 3974-3983.

195. Moore, J., Leonard ; LeJeune, Z. M.; Luces, C. A.; Gates, A. T.; Li, M.; El-Zahab, B.; Garno, J. C.; Warner, I. M. Lysine-Based Zwitterionic Molecular Micelle for Simultaneous Separation of Acidic and Basic Proteins Using Open Tubular Capillary Electrochromatography. *Anal. Chem.* **2010**, *82*, 3997-4005.

196. Kassavetis, S.; Mitsakakis, K.; Logothetidis, S. Nanoscale Patterning and Deformation of Soft Matter by Scanning Probe Microscopy. *Mater. Sci. Eng. C* **2007**, *27*, 1456-1460.

197. Nie, H.-Y.; Motomatsu, M.; Mizutani, W.; Tokumoto, H. Local Modification of Elastic Properties of Polystyrene–Polyethyleneoxide Blend Surfaces. *J. Vac. Sci. Technol. B* **1995**, *13*, 1163-1166.

198. Blach, J. A.; Watson, G. S.; Brown, C. L.; Pham, D. K.; Wright, J.; Nicolau, D. V.; Myhra, S. A Mechanistic Approach to Tip-induced Nanolithography of Polymer Surfaces. *Thin Solid Films* **2004**, *459*, 95-99.

199. Jin, X.; Unertl, W. N. Submicrometer Modification of Polymer Surfaces with a Surface Force Microscope. *Appl. Phys. Lett.* **1992**, *61*, 657-659.

200. Pickering, J. P.; Vancso, G. J. On the Formation of Oriented Nanometer Scale Patterns on Amorphous Polymer Surfaces Studied by Atomic Force Microscopy. *Appl. Surf. Sci.* **1999**, *148*, 147-154.

201. Chen, J.-M.; Liao, S.-W.; Tsai, Y.-C. Electrochemical Synthesis of Polypyrrole within PMMA Nanochannels Produced by AFM Mechanical Lithography. *Synth. Met.* **2005**, *155*, 11-17.

202. Lusker, K. L.; Li, J.-R.; Garno, J. C. Particle Lithography Combined with Contact Printing of Organosilanes: A Hybrid Approach for Fabricating Periodic Arrays of Nanocavities on Surfaces. *Nano Lett.* **2011**, *in submission*.

203. Jourdan, J. S.; Cruchon-Dupeyrat, S. J.; Huan, Y.; Kuo, P. K.; Liu, G. Y. Imaging Nanoscopic Elasticity of Thin Film Materials by Atomic Force Microscopy: Effects of Force Modulation Frequency and Amplitude. *Langmuir* **1999**, *15*, 6495-6504.

204. Price, W. J.; Kuo, P. K.; Lee, T. R.; Colorado, R.; Ying, Z. C.; Liu, G. Y. Probing the Local Structures and Mechanical Response of Nanostructures Using Force Modulation and Nanofabrication. *Langmuir* **2005**, *21*, 8422-8428.

205. Yamamoto, S.; Yamada, H. Interpretation of Direct and Indirect Force Modulation Methods Using Polymer Films. *Langmuir* **1997**, *13*, 4861-4864.

206. Schemmel, A.; Gaub, H. E. Single Molecule Force Spectrometer with Magnetic Force Control and Inductive Detection. *Rev. Sci. Intrum.* **1999**, *70*, 1313-1317.

207. Kawakami, M.; Byrne, K.; Khatri, B. S.; Mcleish, T. C. B.; Radford, S. E.; Smith, D. A. Viscoelastic Measurements of Single Molecules on a Millisecond Time Scale by Magnetically Driven Oscillation of an Atomic Force Microscope Cantilever. *Langmuir* **2005**, *21*, 4765-4772.

208. Magonov, S. N.; Elings, V.; Whangbo, M. H. Phase Imaging and Stiffness in Tapping-mode Atomic Force Microscopy *Surf. Sci.* **1997**, *375*, L385-L391

209. Garcia, R.; Perez, R. Dynamic Atomic Force Microscopy Methods. *Surf. Sci. Rep.* **2002**, *47*, 197-301.

210. Bar, G.; Brandsch, R.; Whangbo, M. H. Description of the Frequency Dependence of the Amplitude and Phase Angle of a Silicon Cantilever Tapping on a Silicon Substrate by the Harmonic Approximation *Surf. Sci.* **1998**, *411*, L802-L809.

211. Whangbo, M. H.; Bar, G.; Brandsch, R. Description of Phase Imaging in Tapping Mode Atomic Force Microscopy by Harmonic Approximation *Surf. Sci.* **1998**, *411*, L794-L801.

212. Chen, G. Y.; Warmack, R. J.; Oden, P. I.; Thundat, T. Transient Response of Tapping Scanning Force Microscopy in Liquids. *J. Vac. Sci. Technol. B* **1996**, *14*, 1313-1317.

APPENDIX A: PROCEDURE FOR PARTICLE LITHOGRAPHY COMBINED WITH VAPOR DEPOSITION OF ORGANOSILANES

1. *Substrate Preparation*. Cut boron-doped double-sided polished silicon(111) wafers into 1 × 1 cm^2 pieces to use as substrates for patterning. To remove organic and inorganic contaminants, immerse the substrates into piranha solution (3:1 v/v ratio of concentrated H_2SO_4 and 30% H_2O_2) for 1 h. Piranha solution is highly corrosive and should be handled with caution. After soaking, rinse the substrates with copious amounts of ultrahigh pure deionized water and dry in air. Note: use freshly prepared piranha solution, old solutions are not effective. Do not exceed 1 h soaking because the surface will become etched and rough. For indium tin oxide (ITO) or glass substrates, soak in piranha solution for 1 h and rinse with copious amounts of water. Then place substrate in a sealed container with RCA-1 solution (1:1:5 v/v ratio of H_2O_2 + NH_4OH + H_2O) and heat for 1 h at 80 °C. After removing from oven and allowing the substrate to cool, rinse with copious amounts of water and dry in air.

2. *Procedure for Washing Latex Spheres*. Wash the latex mesospheres (1 wt%) to remove surfactants and charge stabilizers by centrifugation. Place 300 µL of latex solution in a microcentrifuge tube. Centrifuge the sample for 15 min at 14,000 rpm. A pellet will form at the bottom of the microcentrifuge tube. Discard the supernatant and resuspend the latex mesospheres in deionized water with vortex mixing. Repeat the rinsing cycle three times. Resuspend the pellet in 300 µL deionized water followed by vortex mixing.

3. *Preparation of Latex Mask*. To produce ring-shaped nanopatterns of organosilanes, deposit a drop (20 µL) of the latex suspension on a clean Si(111) substrate and dry for 12 h in ambient conditions (25 °C, relative humidity ~55%).

4. *Vapor Deposition Procedure*. Place the sample on a platform in a glass chamber containing a small volume (300 μL) of neat organosilane at the bottom of the chamber. Seal the container with parafilm and heat in an oven at 70 °C for 8 h to generate vapors of organosilane.

5. *Removal of Latex Mask*. Remove the film of latex mesospheres by rinsing and sonicating the sample in deionized water and ethanol several times. After removing the latex mask, dry the sample in air.

APPENDIX B: PREPARATION OF ORGANOSILANE NANOPATTERNS USING PARTICLE LITHOGRAPHY WITH CONTACT PRINTING

1. *Substrate Preparation.* Use a glass coverslip, boron-doped double-sided polished Si(111), or ITO as a substrate for nanopatterning organosilanes with contact printing. Cut the Si(111) wafer into 1 ×1 cm^2 pieces. Immerse the Si(111) substrate into a piranha solution (3:1 v/v ratio of H_2SO_4 and 30% H_2O_2) for 1 h followed by rinsing with deionized water. Piranha solution is highly corrosive and should be handled with caution. For glass and ITO substrates, clean in piranha solution for 1 h, rinse with deionized water, then immerse in RCA-1 solution (1:1:5 v/v ratio of H_2O_2 + NH_4OH + H_2O) for 1 h at 80 °C. Rinse the substrates with copious amounts of deionized water and dry in air. Note: use freshly prepared reagent solutions, old solutions are not effective. Do not exceed 1 h soaking because the surface will become etched and rough.

2. *Procedure for Washing Latex Spheres*. Wash latex mesospheres to remove surfactants and charge stabilizers by centrifugation. Place 300 µL of latex solution in a microcentrifuge tube. Centrifuge the sample for 15 min at 14,000 rpm. A pellet will form at the bottom of the microcentrifuge tube. Discard the supernatant and resuspend the latex mesospheres in deionized water with vortex mixing. Repeat this three times. Resuspend the pellet in 300 µL deionized water followed by vortex mixing.

3. *Preparation of Latex Mask*. To produce pore-shaped nanopatterns of organosilanes, deposit a drop (20 µL) of the latex suspension on a clean substrate and dry for 2 h in ambient conditions (25 °C, relative humidity ~55%).

4. *Preparation of PDMS Stamp.* In a plastic cup, weigh 10 parts of Sylgard 184 pre-polymer and 1 part of curing agent. Dispense the viscous solutions using a disposable plastic syringe. Mix well with a spatula and pour into a petri dish. Remove bubbles by letting the mixture sit at room temperature for at least 2 h. Place the petri dish in an oven and heat at 70 °C for 1 h to cure the

polymer. Remove the sample from oven and let cool to room temperature. Cut PDMS slab into 2 × 2 cm^2 pieces and rinse with ethanol. Samples can be stored for several months in ethanol before use.

5. *Inking Procedure for PDMS Stamp.* Prepare a 30% solution of OTS in bicyclohexyl (or anhydrous toluene). Deposit 30 μL of OTS solution on top of a PDMS block and spread evenly with pipette tip. Quickly dry the solution with ultrahigh purity argon.

6. *Ink Transfer Step.* Immediately after drying, gently place the PDMS block 'inked' with OTS on top of the latex masked substrate for 1 h.

7. *Removal of Latex Mask*. Remove the film of latex mesospheres by rinsing and sonicating the sample in deionized water and ethanol several times. After removing the latex mask, dry the sample in air.

APPENDIX C: SETUP AND OPERATION FOR AFM IMAGING WITH INDIRECT MAGNETIC MODULATION

1. *Cable Connections for Indirect Magnetic Modulation AFM.* The instrument configuration for indirect magnetic modulation (IMM) is displayed in Figure C.1. To setup the AFM instrument for IMM imaging, connect cables for the PicoSPM II controller, MAC/AC controller and head electronic box as shown Figure C.1. Connect one cable from the AUX of the Picoplus head electronic box to the phase input of the MAC/AC controller. A second cable is connected from the amplitude of MAC/AC controller to the AUX IN of the PicoSPM II controller.

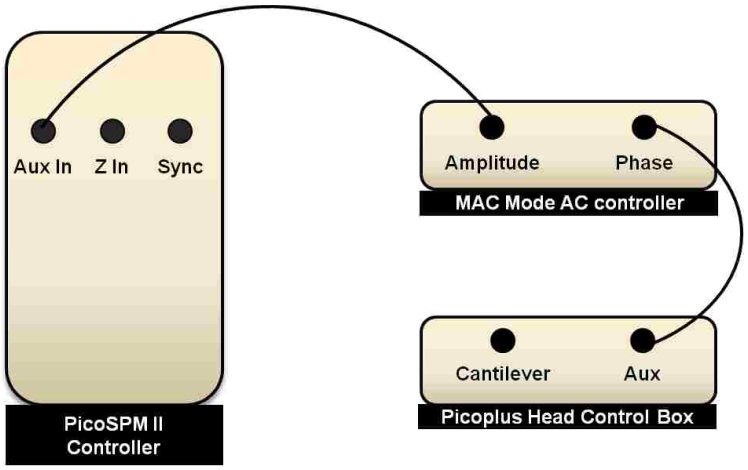

Figure C.1 Cable connections for IMM imaging.

2. *Instrument Setup and Sample Installation.* A magnetic AC (MAC) sample plate, which contains a wire coil solenoid underneath, is used for IMM to drive the oscillation of the nosecone assembly during imaging. For IMM, an Agilent 5500 AFM multipurpose scanner with a scan area of $10 \times 10\ \mu m^2$ is used and operated in contact mode with an AAC nosecone. Insert the AAC nosecone into the Agilent 5500 AFM multipurpose scanner. Place the sample onto the MAC mode sample plate. NOTE: The IMM mode should not be used for samples or tips containing magnetic materials. It is only useful for samples such as polymers, SAMs, proteins, etc. that are nonmagnetic. For contact mode imaging with IMM, a soft, non-magnetic tip should

be used. For example, a silicon nitride cantilever (MSCT-AUHW, Veeco Probes) with a force constant of 0.1 N m^{-1} and a resonance frequency of 26 kHz or a silicon cantilever (SICON, NanoScience Instruments) with a force constant of 0.2 N m^{-1} and a resonance frequency of 12 kHz can be used for IMM imaging. Install the MAC mode sample plate and the AFM scanner. Focus the laser light onto the back of the cantilever to optimize the photodiode signal.

3. *Software Settings.* Launch PicoScan v5.3.3 software. Under 'mode', select 'AFM; under 'AC mode control' panel, select 'MAC' and 'contact'. Under 'View', select the 'Layout Editor' option, create eight channels for topography, defection, Aux IN BNC and Aux IN 5 on the top and bottom rows. The frames on the top row represent raw data and those on the bottom row represent processed data. Aux IN BNC represents IMM amplitude images, and Aux IN 5 corresponds to IMM phase images.

4. *Acquisition of Frequency Spectra.* Open the AFM AC Mode Frequency Plot window and select the frequency range. Choose the MAC/Top MAC option in the AC Mode controls window. Uncheck the drive on box to turn the AC electromagnetic field off. Set the force setpoint value to '0' and click 'approach' to approach the tip to the surface. Once the tip engages the surface, select buffer 'A' and click 'start' under the AC Mode frequency plot panel to sweep the frequency with the AC electromagnetic field still off. Check the 'Drive On' box and enter 5% for the Drive On and 1X for Gain. Reduce the force setpoint to the lowest value possible to lift the tip away from the surface. Click on 'sweep' to acquire a frequency spectrum while the AC electromagnetic field is on and the tip is disengaged. Adjust the Drive On % and frequency range (0-600 kHz) accordingly until prominent frequency peaks are observed in the spectrum. Note: domains with different composition will have different frequency profiles. It is important to identify the different domains (e.g. bare substrate versus organosilane nanostructures) and acquire frequency spectra of the different materials. Also, acquire force-distance curves of the

distinct surface domains. Increase the force setpoint slowly until the tip is engaged with the surface. Check the 'overlay' box in the AC mode frequency plot panel and click on the sweep button again to acquire a resonance spectrum with the field on with the tip in contact with the surface. Adjust the Drive On % and frequency range (0-600 kHz) accordingly until prominent frequency peaks are observed in the spectrum. Differences in resonance frequency spectra acquired with or without the tip in contact with surfaces should be apparent. After the tip engages the surface, the natural resonance frequency slightly shifts.

5. *IMM Imaging.* Select the resonance frequency for operation with IMM imaging by left clicking the resonance peak maximum. Select the 'Active' check box in the AC mode frequency plot panel. Click 'Start' to acquire IMM images and adjust the integral (I) gain, the proportional (P) gain and the force setpoint values as if operating under conventional contact mode.

.

APPENDIX D: LETTERS OF PERMISSION

RightsLink | Copyright Clearance Center

Thank You For Your Order!

Dear Ms. Kathie Lusker,

Thank you for placing your order through Copyright Clearance Center's RightsLink service. Elsevier has partnered with RightsLink to license its content. This notice is a confirmation that your order was successful.

Your order details and publisher terms and conditions are available by clicking the link below:
http://s100.copyright.com/CustomerAdmin/PLF.jsp?lID=2011081_1313602405824

Order Details
Licensee: Kathie L Lusker
License Date: Aug 17, 2011
License Number: 2731460853824
Publication: Thin Solid Films
Title: Particle lithography with vapor deposition of organosilanes: A molecular toolkit for studying confined surface reactions in nanoscale liquid volumes
Type Of Use: reuse in a thesis/dissertation
Total: 0.00 USD

To access your account, please visit https://myaccount.copyright.com.

Please note:Online payments are charged immediately after order confirmation; invoices are issued daily and are payable immediately upon receipt.

To ensure we are continuously improving our services, please take a moment to complete our customer satisfaction survey.

B.1:v4.2

ELSEVIER LICENSE
TERMS AND CONDITIONS
Aug 17, 2011

This is a License Agreement between Kathie L Lusker ("You") and Elsevier ("Elsevier") provided by Copyright Clearance Center ("CCC"). The license consists of your order details, the terms and conditions provided by Elsevier, and the payment terms and conditions.

Supplier	Elsevier Limited The Boulevard,Langford Lane Kidlington,Oxford,OX5 1GB,UK
Registered Company Number	1982084
Customer name	Kathie L Lusker
Customer address	325 East state st. Apt. D Baton Rouge, LA 70802
License number	2731460853824
License date	Aug 17, 2011
Licensed content publisher	Elsevier
Licensed content publication	Thin Solid Films
Licensed content title	Particle lithography with vapor deposition of organosilanes: A molecular toolkit for studying confined surface reactions in nanoscale liquid volumes
Licensed content author	Kathie L. Lusker,Jing-Jiang Yu,Jayne C. Garno
Licensed content date	31 May 2011
Licensed content volume number	519
Licensed content issue number	15
Number of pages	7
Start Page	5223
End Page	5229
Type of Use	reuse in a thesis/dissertation

Portion	full article
Format	both print and electronic
Are you the author of this Elsevier article?	Yes
Will you be translating?	No
Order reference number	
Title of your thesis/dissertation	Fabrication of Organosilane Nanostructures as Selective Sites for Surface Chemical Reactions
Expected completion date	Oct 2011
Estimated size (number of pages)	180
Elsevier VAT number	GB 494 6272 12
Permissions price	0.00 USD
VAT/Local Sales Tax	0.0 USD / 0.0 GBP
Total	0.00 USD

Terms and Conditions

Thesis/Dissertation: If your license is for use in a thesis/dissertation your thesis may be submitted to your institution in either print or electronic form. Should your thesis be published commercially, please reapply for permission. These requirements include permission for the Library and Archives of Canada to supply single copies, on demand, of the complete thesis and include permission for UMI to supply single copies, on demand, of the complete thesis. Should your thesis be published commercially, please reapply for permission.

American Chemical Society's Policy on Theses and Dissertations

This is regarding request for permission to include your paper(s) or portions of text from your paper(s) in your thesis. Permission is now automatically granted; please pay special attention to the implications paragraph below. The Copyright Subcommittee of the Joint Board/Council Committees on Publications approved the following:

Copyright permission for published and submitted material from theses and dissertations
ACS extends blanket permission to students to include in their theses and dissertations their own articles, or portions thereof, that have been published in ACS journals or submitted to ACS journals for publication, provided that the ACS copyright credit line is noted on the appropriate page(s).

Publishing implications of electronic publication of theses and dissertation material
Students and their mentors should be aware that posting of theses and dissertation material on the Web prior to submission of material from that thesis or dissertation to an ACS journal may affect publication in that journal. Whether Web posting is considered prior publication may be evaluated on a case-by-case basis by the journal's editor. If an ACS journal editor considers Web posting to be "prior publication", the paper will not be accepted for publication in that journal. If you intend to submit your unpublished paper to ACS for publication, check with the appropriate editor prior to posting your manuscript electronically.

Reuse/Republication of the Entire Work in Theses or Collections:
Authors may reuse all or part of the Submitted, Accepted or Published Work in a thesis or dissertation that the author writes and is required to submit to satisfy the criteria of degree-granting institutions. Such reuse is permitted subject to the ACS' "Ethical Guidelines to Publication of Chemical Research" (http://pubs.acs.org/page/policy/ethics/index.html); the author should secure written confirmation (via letter or email) from the respective ACS journal editor(s) to avoid potential conflicts with journal prior publication*/embargo policies. Appropriate citation of the Published Work must be made. If the thesis or dissertation to be published is in electronic format, a direct link to the Published Work must also be included using the ACS Articles on Request author-directed link−
see http://pubs.acs.org/page/policy/articlesonrequest/index.html

* Prior publication policies of ACS journals are posted on the ACS website at
http://pubs.acs.org/page/policy/prior/index.html

If your paper has not yet been published by ACS, please print the following credit line on the first page of your article: "Reproduced (or 'Reproduced in part') with permission from [JOURNAL NAME], in press (or 'submitted for publication'). Unpublished work copyright [CURRENT YEAR] American Chemical Society." Include appropriate information.

If your paper has already been published by ACS and you want to include the text or portions of the text in your thesis/dissertation, please print the ACS copyright credit line on the first page of your article: "Reproduced (or 'Reproduced in part') with permission from [FULL REFERENCE CITATION.] Copyright [YEAR] American Chemical Society." Include appropriate information.

Submission to a Dissertation Distributor: If you plan to submit your thesis to UMI or to another dissertation distributor, you should not include the unpublished ACS paper in your thesis if the thesis will be disseminated electronically, until ACS has published your paper. After publication of the paper by ACS, you may release the entire thesis (not the individual ACS article by itself) for electronic dissemination through the distributor; ACS's copyright credit line should be printed on the first page of the ACS paper.

JOHN WILEY AND SONS LICENSE
TERMS AND CONDITIONS

This is a License Agreement between Kathie L Lusker ("You") and John Wiley and Sons ("John Wiley and Sons") provided by Copyright Clearance Center ("CCC"). The license consists of your order details, the terms and conditions provided by John Wiley and Sons, and the payment terms and conditions.

All payments must be made in full to CCC. For payment instructions, please see information listed at the bottom of this form.

License Number	2732561153601
License date	Aug 19, 2011
Licensed content publisher	John Wiley and Sons
Licensed content publication	Angewandte Chemie International Edition
Licensed content title	Side-by-Side Patterning of Multiple Alkanethiolate Monolayers on Gold by Edge-Spreading Lithography
Licensed content author	Matthias Geissler,Joseph M. McLellan,Jingyi Chen,Younan Xia
Licensed content date	Jun 6, 2005
Start page	3596
End page	3600
Type of use	Dissertation/Thesis
Requestor type	University/Academic
Format	Print and electronic
Portion	Figure/table
Number of figures/tables	1
Number of extracts	
Original Wiley figure/table number(s)	Figure 3
Will you be translating?	No
Order reference number	
Total	0.00 USD
Terms and Conditions	

JOHN WILEY AND SONS LICENSE
TERMS AND CONDITIONS
Aug 19, 2011

This is a License Agreement between Kathie L Lusker ("You") and John Wiley and Sons ("John Wiley and Sons") provided by Copyright Clearance Center ("CCC"). The license consists of your order details, the terms and conditions provided by John Wiley and Sons, and the payment terms and conditions.

All payments must be made in full to CCC. For payment instructions, please see information listed at the bottom of this form.

License Number	2732570822469
License date	Aug 19, 2011
Licensed content publisher	John Wiley and Sons
Licensed content publication	Small
Licensed content title	Fabrication of Nanoscale Rings, Dots, and Rods by Combining Shadow Nanosphere Lithography and Annealed Polystyrene Nanosphere Masks
Licensed content author	Adam Kosiorek,Witold Kandulski,Hanna Glaczynska,Michael Giersig
Licensed content date	Apr 1, 2005
Start page	439
End page	444
Type of use	Dissertation/Thesis
Requestor type	University/Academic
Format	Print and electronic
Portion	Figure/table
Number of figures/tables	1
Number of extracts	
Original Wiley figure/table number(s)	Figure 5
Will you be translating?	No
Order reference number	
Total	0.00 USD

Dear Kathie Lusker,

The Royal Society of Chemistry hereby grants permission for the use of the material specified below in the work described and in all subsequent editions of the work for distribution throughout the world, in all media including electronic and microfilm. You may use the material in conjunction with computer-based electronic and information retrieval systems, grant permissions for photocopying, reproductions and reprints, translate the material and to publish the translation, and authorize document delivery and abstracting and indexing services. The Royal Society of Chemistry is a signatory to the STM Guidelines on Permissions (available on request).

Please note that if the material specified below or any part of it appears with credit or acknowledgement to a third party then you must also secure permission from that third party before reproducing that material.

Please ensure that the published article carries a credit to The Royal Society of Chemistry in the following format:

[Original citation] – Reproduced by permission of The Royal Society of Chemistry

and that any electronic version of the work includes a hyperlink to the article on the Royal Society of Chemistry website. The recommended form for the hyperlink is http://dx.doi.org/10.1039/DOI suffix, for example in the link http://dx.doi.org/10.1039/b110420a the DOI suffix is 'b110420a'. To find the relevant DOI suffix for the RSC paper in question, go to the Journals section of the website and locate your paper in the list of papers for the volume and issue of your specific journal. You will find the DOI suffix quoted there.

Regards,
Charlotte Pearce

Charlotte Pearce, Legal Services Department,
Royal Society of Chemistry, Thomas Graham House Science Park,
Milton Road, Cambridge CB4 0WF, UK
Tel +44 (0) 1223 420066, Fax +44 (0) 1223 423623
http://www.rsc.org

-----Original Message-----
From: kluske1@lsu.edu [mailto:kluske1@lsu.edu]
Sent: 19 August 2011 17:06
To: CONTRACTS-COPYRIGHT (shared)
Subject: Permission Request Form: Kathie Lusker

Name : Kathie Lusker
Address : Louisiana State Univ.
Dept. of Chemistry
232 Choppin Hall
Baton Rouge, LA 70803

Tel : 225-578-8853
Fax :
Email : kluske1@lsu.edu

I am preparing the following work for publication:

Article/Chapter Title : FABRICATION OF ORGANOSILANE NANOSTRUCTURES AS SELECTIVE SITES FOR SURFACE CHEMICAL REACTIONS
Journal/Book Title : Ph.D. Dissertation
Editor/Author(s) : Kathie L. Lusker
Publisher : Louisiana State University

I would very much appreciate your permission to use the following material:
Journal/Book Title : The Analyst
Editor/Author(s) : Jie-Ren Li, Gretchen C. Henry, Jayne C. Garno
Volume Number : 131
Year of Publication : 2006
Description of Material : Fabrication of Nanopatterned Films of bovine serum albumin and Staphylococcal protein A using latex particle lithography (Figure 4)
Page(s) : 244-250

Any Additional Comments

I am requesting to include Figure 4 in the listed publication for use in my disseration

VITA

Kathie Lee Lusker was born in Fayetteville, North Carolina, and raised by her loving parents Lee and Maria Lusker. She has three sisters (Jennifer, Zabrina, and Aine), one nephew (Carson), and one niece (Amaiya). Her father served in the Army for 20 years, which allowed her to live in many places around the world. Kathie graduated from Denham Springs High School in Denham Springs, Louisiana, in 1999. Afterwards, Kathie attended Louisiana State University and received a Bachelor of Science degree in chemistry in 2004. Upon graduation, she worked at Albemarle Corporation as a laboratory analyst for almost two years. In fall of 2006, Kathie decided to pursue a higher education and enrolled in the doctoral program for analytical chemistry at Louisiana State University under the supervision of Dr. Jayne Garno.

Kathie's research interests include fabrication of nanostructured materials on surfaces, as well as conducting nanoscale characterizations of surfaces and nanomaterials using high resolution atomic force microscopy. She has two first-author publications and six co-authored publications. Kathie currently has three more first author and three co-authored manuscripts being submitted to peer-reviewed journals. During graduate studies at LSU, Kathie had the opportunity to attend local, regional, and international conferences, where she has presented two oral presentations (in New Orleans, Louisiana and Beijing, China), eleven first author posters, and thirteen co-authored posters on her research. Kathie has also directed thesis research projects for three LSU undergraduate students majoring in chemistry. Throughout her graduate studies, she has received prestigious research and teaching awards, including three first place student poster awards at national and regional conferences, an LSU Charles E. Coates Travel Award, two LSU Graduate Student Travel Stipends, the 2009 Procter and Gamble Research Award, and the 2009 LSU Outstanding Graduate Teaching Award for Organic Chemistry Lab. Currently,

Kathie is an active member of the Materials Research Society, the American Chemical Society, and Iota Sigma Pi National Honors Society for Women in Chemistry.